Molecular Polymer Bottlebrushes with Tunable Hydrophilic-Hydrophobic Character and their Interaction with Serum Proteins, Cancer Cells, and Tumours

A thesis submitted in fulfilment of the requirements for the degree of

Doctor of Philosophy

by

Parathan Ramamurthi

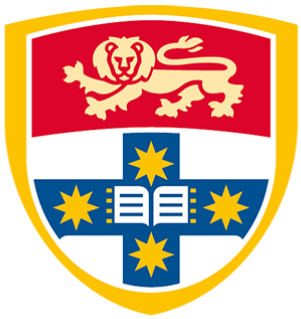

THE UNIVERSITY OF SYDNEY

School of Chemistry

Faculty of Science

September 2023

Author's Declaration

I hereby declare that the work submitted as part of this thesis was obtained by myself between January 2020 and September 2023 at the School of Chemistry to partially fulfill the requirements of a Doctor in Philosophy in Science.

This thesis has not been distributed for any degree or any other purpose. I hereby certify that all content of this thesis is, to the best of my knowledge,

_____ 30/09/23

Parathan Ramamurthi **Date**

Thesis Abstract

Nanosized drug delivery systems have been a focal point of research and development in the past few decades, having demonstrated superior targeting, and enhanced drug cargo stability compared to their small-molecule analogues. This has been especially advantageous in their use against ailments such as cancer, although their improvements are usually countered by poor penetrability and accumulation into tumour tissue. Quite often, such nanoparticle systems are also compromised by the protein corona that spontaneously manifests when proteins adsorb onto their surfaces *in vivo*. While this process has radical consequences for an NP's immunogenicity, drug release profile and long-term retention, it remains poorly understood. To that end, significant efforts have been devoted to studying the structure-function-property relationships between nanoparticle physicochemical parameters (such as size, surface chemistry, shape and stiffness) and tumour penetrability, accumulation, cancer cell association and interactions with serum proteins. Compared to these parameters however, nanoparticle amphiphilicity is not as well understood in the same context. In this work, the role of amphiphilicity in regulating various aspects of nanoparticle behaviour in biological environments, using polymer bottlebrushes (otherwise known as molecular polymer brushes; MPBs) as the nanoparticle platform of choice. The second chapter details an investigation into the influence of amphiphilicity on nanoparticle penetrability, passive targeting, and accumulation into tumours using MPBs composed with varying hydrophobicity levels. With an increase in the MPBs' hydrophobicity up to an intermediate point, their tumour-homing properties and long-term accumulation was improved in ovarian cancer-bearing mouse models. However, only marginal differences between differently hydrophobic MPBs in tumour penetration were observed in 2D and 3D in vitro tumour models. In the third chapter, nanoparticle interactions on cell membranes and serum proteins as modulated by

amphiphilicity was the subsequent focus. Using protein-enriched serum, aspects of the nanoparticle's character such as size change and cellular uptake efficiency were studied as a function of MPB amphiphilicity. MPBs underwent little change in their overall size with co-incubation with serum proteins despite their hydrophobicity levels. Flow cytometric analyses revealed that the intermediately hydrophobic MPBs again experienced greatest levels of cancer cell association, irrespective of the presence or absence of serum proteins. However, a more striking result was seen comparing the MPBs' cellular association under different serum conditions, wherein improvements in cellular uptake were experienced in the absence of a potential protein corona, which was negated upon switching to a protein-containing medium. Subsequent analysis via ITC using albumin as a standalone model protein revealed that regardless of amphiphilicity, all MPBs were able to resist nonspecific binding of albumin to their surfaces, despite its high abundance in serum. In the final part of this study, the effect of amphiphilicity on nanoparticle interactions with the cell membrane were investigated via electrochemical impedance spectroscopy of tethered bilayer lipid membranes (tBLMs). Reversible and miniscule deformations in the cell membranes incited by the MPBs were observed across the series and were notably proportional in magnitude to each MPBs hydrophilicity at prolonged timescales. As it stands, these perturbations could not be solely attributed to thermosensitive dehydration of the polymer chains stemming from their varied hydrophobicity levels.

Publications Included in Thesis and Statement of Authorship Attribution

Chapter 2 of this thesis is published as the following;

1) Ramamurthi, P.; Zhao, Z.; Burke, E.; Steinmetz, N. F.; Müllner, M. Tuning the Hydrophilic–Hydrophobic Balance of Molecular Polymer Bottlebrushes Enhances Their Tumor Homing Properties. Adv. Healthc. Mater. 2022, 11 (12), 2200163.

My contribution to this publication included all experimental work and draft writing, with the exception of work related to in vivo experiments.

In addition to the statements above, as I am not the corresponding author of the published item, permission to include the published material has been granted by the corresponding author, Assoc. Prof. Markus Müllner.

_____ 30/09/23

Parathan Ramamurthi **Date**

As supervisor for the candidature upon which this thesis is based, I can confirm that the authorship attribution statements above are correct.

_____ 30/09/23

Markus Müllner **Date**

In addition to the above publication, material in this thesis was presented orally at the following conferences and symposiums.

1) Ramamurthi, P.; Zhao, Z.; Burke, E.; Steinmetz, N. F.; Müllner, M. "Tuning the amphiphilicity of molecular polymer bottlebrushes to improve tumour homing behaviour" - Oral presentation, RACI National Congress, RACI, Brisbane, Australia, July 2022

2) Ramamurthi, P.; Zhao, Z.; Burke, E.; Steinmetz, N. F.; Müllner, M. "Role of Amphiphilicity of Bottlebrush Polymers in their Interaction with Cancer Cells and Tumours" - Oral Presentation, PolyNSW Symposium, RACI November 2021

3) Ramamurthi, P.; Zhao, Z.; Burke, E.; Steinmetz, N. F.; Müllner, M. "Role of Amphiphilicity of Bottlebrush Polymers in their Interaction with Cancer Cells and Tumours" - Oral presentation, Postgraduate Symposium, School of Chemistry, University of Sydney, September 2021 (Awarded Best Presentation)

The duration of this course also included the publication of a work not included in this thesis, to which I contributed;

1) Lane, J. D. E.; Shiels, G.; Ramamurthi, P.; Müllner, M.; Jolliffe1, K. A. Water-Soluble Squaramide-Functionalised Copolymers for Anion Recognition. *Macromol. Rapid Commun.* **2023**.

Statement of Contribution

The findings obtained over the course of this thesis were acquired in collaboration with other researchers. A breakdown of each collaborator's contribution to each research chapter is detailed in the following sections.

Chapter II: All MPB syntheses and their post-polymerisation functionalisation was performed by me. MPB characterisation by SEC, NMR, DLS, fluorescence spectroscopy, IR spectroscopy was carried out by me. In vitro experiments including maintenance of cell cultures, culturing of cell monolayers and spheroids and their evaluation using confocal microscopy and flow cytometry was performed by me. Evaluation of the MPBs *in vivo* performance using mice models was carried out by Dr. Zhongchao Zhao (Steinmetz group) at the University of California San Diego (UCSD). This included sourcing and care of test mice, culturing of and inoculation of tumour cells, and in vivo analyses.

Chapter III: All MPB syntheses was performed by me, including their NMR characterisation. tBLM formation and evaluation via electrochemical impedance spectroscopy was performed by me, with Dr. Charles Cranfield (UTS) assisting in initial demonstrations of the technique. Analysis of the MPBs interactions with proteins and its effects using confocal microscopy, flow cytometry, DLS and ITC were carried out by me.

I hereby certify that all contributions of the individuals have been acknowledged appropriately.

_____ 30/09/23

Parathan Ramamurthi **Date**

_____ 30/09/23

Markus Müllner **Date**

Research Involving Animal Subjects

All animal experiments were carried out in accordance with the guidelines of the Institutional Animal Care and Use Committee (IACUC) of the University of California San Diego (UCSD) and approved by the Animal Ethics Committee of UCSD. Female NCR nu/nu mice 6-8 weeks old were sourced from In-House Breeding Colony of UCSD and all mice were housed at the UCSD Moores Cancer Center with unlimited food and water.

Acknowledgements

My first round of thanks goes to Dr. Markus Müllner for all his support and direction throughout the course of this project. It is thanks to his insight, mentorship and encouragement that allowed me to persevere and hopefully become a better scientist over the years. I would secondly like to thank past and present members of my research group, the Polymer Nanostructures Group (PNG). To my old lab-mates Alicia, Karen, Theo, Antoine, Emma, Thomas, Max, Clare, Amanda, Cindy, Cheryl, David and Sophia, thank you for all the memorable moments and unyielding support in 319, 341 and now 323. It's been great having all of you around, whether it's time spent at one of Newtown's many restaurants for group lunches, or the meeting rooms of the chemistry building. I'd also like to thank members of the Key Centre for Polymers and Colloids for both their professional and personal assistance inside the lab and out, particularly members of the Neto, Warr and Hawkett groups. Special mention must also go to various staff members in the School of Chemistry, the ACMM and the Charles Perkins Centre for all the assistance rendered towards my project over the years.

Finally, I want to extend my immense gratitude to my family; Amma, Appa and Nak, as well as my close friends Oneka, Rohan, Ohona, Ananya, Savinda and Abhi, and my partner Madhu for putting up with and supporting me particularly over the past few gruelling years. None of this would have been possible without your combined love and support that's kept me going.

To Appappa, Appamma, Ammamma and Thatha,

Even though you couldn't all be here at the end of my journey, I hope I've made every one of you proud. This work in chemistry is a tribute to the devotion you've gifted me all my life, and the person you helped me become.

I miss you all.

Table of Contents

List of Abbreviations

^{1}H-NMR	Proton nuclear magnetic resonance spectroscopy
2D	Two-dimensional
3D	Three-dimensional
^{64}Cu	Copper-64
AFM	Atomic force microscopy
ARGET	Activators regenerated by electron transfer
ATRP	Atom transfer radical polymerisation
BAM	N-tert-butylacrylamide
BIEM	2-(2-Bromoisobutyryloxy)ethyl methacrylate
$CDCl_3$	Deuterated chloroform
CLSM	Confocal laser scanning microscopy
CPT	Camptothecin
CRP	Controlled radical polymerisation
CTA	Chain transfer agent
DSC	Differential scanning calorimetry
DEGMA/MeO_2MA	Di(ethylene glycol) methyl ether methacrylate
DLS	Dynamic light scattering
DMAc	Dimethylacetamide
DMAEMA	2-(dimethylamino) ethyl methacrylate
DMF	Dimethylformamide
DOX	Doxorubicin
DP	Degree of polymerisation
eATRP	Electrochemically-mediated atom transfer radical polymerisation
ECM	Extracellular matrix
EIS	Electrochemical impedance spectroscopy
EPR	Enhanced permeability and retention
FSC	Forward scatter
GMA	Glycidyl methacrylate
HBM	Hybrid bilayer membrane
HEMA	2-hydroxyethyl methacrylate
ICAR	Initiators for continuous activator regeneration
ID	Injected dose

IFP	Interstitial fluid pressure
ITC	Isothermal titration calorimetry
IV	Intravenous
IVIS	*In vivo* imaging system
K_p	Propagation constant
K_t	Termination constant
LAM	Less activated monomer
LC-MS	Liquid chromatography-mass spectrometry
MAM	More activated monomer
MCTS	Multicellular tumour spheroid
MeOD	Deuterated methanol
MPB	Molecular polymer brush
MPS	Mononuclear phagocyte system
NSCLC	Non-small cell lung cancer
NIPAM	N-isopropylacrylamide
NIPMAM	N-isopropylmethacrylamide
NOTA	1,4,7-triazacyclononane-N, N′,N-triacetic acid
NR	Neutron reflectometry
OEGMA	Oligo(ethylene glycol) methyl ether methacrylate
PBS	Phosphate buffered saline
PC	Protein corona
PEG	Polyethylene glycol
PEGMA	Poly(ethylene glycol) methyl ether methacrylate (Mn = 300 g mol^{-1})
PET	Positron emission tomography
PS	Polystyrene
RAFT	Reversible addition-fragmentation chain transfer polymerisation
RDRP	Reversible deactivation radical polymerisation
SANS	Small angle neutron scattering
SDS-PAGE	Sodium dodecyl sulfate polyacrylamide gel electrophoresis
SEC	Size exclusion chromatography
SLB	Supported lipid bilayer
SPR	Surface plasmon resonance
SSC	Side scatter

tBMA	Tert-butyl methacrylate
T_c	Cloud point temperature
THF	Tetrahydrofuran
TME	Tumour microenvironment
UV-Vis	Ultraviolet-Visible
α-BiBB	Alpha-bromoisobutyryl bromide

CHAPTER I

Literature Review

1.1. Current Strategies and Issues facing Cancer Chemotherapy

Cancer has endured as one of the leading causes of human mortality up to the present and continues to place a heavy financial and health burden on the global community, with these only expected to grow steadily in future.[1,2] This condition is primarily characterised by uncontrolled growth of the body's own cells, often due to erroneous changes to their genes.[3] The result of this runaway cellular replication often manifests as a mass of cancerous tissue called a tumour. In dire instances, patient complications can arise when these tumours break away from their primary site of formation and establish themselves in other parts of the body, forming new tumours in a process known as metastasis that dramatically lowers chances of patient survival. Given their importance, both metastatic and benign tumours often serve as the target for chemotherapy treatment strategies.

Current approaches to cancer chemotherapy usually involve the intravenous (IV) administration of small-molecule drugs, which should travel throughout the body and eventually accumulate at the tumour site to induce sufficient cancer cell necrosis. Although the development of modern chemotherapy has made immense improvements in patient survival rates, their successes have been negated by significant drawbacks. These limitations usually include the drugs' poor pharmacokinetic profiles when intravenously injected,[4] and inability to differentiate between healthy cells and organs from cancerous ones, eliciting toxic side effects in patients as a result.[5,6] Apart from their non-specific biodistribution, conventional chemotherapeutics are usually also burdened by poor infiltration levels of tumour tissue itself.[7] This is particularly detrimental in the case of cancer, as the lowered levels of the cytotoxic drug permeating the target tumour means a substantial population of surviving cells reform the tumour and trigger relapse.[8] Moreover, the surviving cell population, by resisting the initial drug dose, will oftentimes present a

harder target for successive treatment attempts due to the now drug-resistant cells comprising the reformed tumour.[9] Although a dose increase can counter this by ensuring a higher amount suffuses the target, cytotoxic side-effects may be simultaneously exacerbated as the drug's non-specific biodistribution pattern is not improved with a dose increase.

1.2. Applications of Nanoparticles in Tumour-Targeted Drug Delivery and Current Challenges

Considering the numerous pitfalls plaguing current small-molecule cancer drugs, there is a pervasive need for alternative modalities that can ensure the chosen drug reaches its tumour target in a selective and efficient manner. Amongst the avenues being considered for that purpose, nanotechnology has become a major focus point of research in the past few decades.[10] Owing to their small size (often in the range of tens to hundreds of nanometres), nanoparticles are on a similar size scale as most biomolecular complexes and the cellular processes, putting them in a unique position to be able to exert their effects.[11] Moreover, the development of advanced synthetic and modification techniques has enabled the physical and chemical properties of nanoparticles to be effortlessly adjusted to fit their intended function.[12] This feature has made them attractive as therapeutic and diagnostic agents for a range of conditions, including cancer.

As of 2023, a handful of nanoparticle designs have received regulatory approval for treatment of various cancers, ranging from liposome-encapsulated drugs, to iron oxide nanoparticles.[13–15] While these formulations have unarguably managed to prolong patient lifespans and reducing overall toxicity, their general benefits can be considered rather meagre when considering the greater number of anticancer nanomedicines being evaluated

in pre-clinical trials, which numbers more than a hundred as of 2022.[16] Furthermore, the gains yielded by current nanosized drug carriers on the market also pales when factoring in the notoriously high failure rate of translating proposed nanomedicines from preclinical research settings into commercially and clinically viable products. In their perspective article on present challenges and opportunities associated with cancer nanoformulations, He *et al.* analysed anticancer nanomedicines that were part of ongoing clinical trials as well as those granted full clinical approval. As part of their findings, they reported success rates as high as 94 % based on phase I trial results, although subsequent phase II evaluations lead to a sharp decline in the number of formulations that make it through (48 % success rate based on completed trials). Attrition rates were only further exacerbated in completed phase III tests, with only 14 % of candidates reporting satisfactory outcomes.[17]

While the specific reasons for the difficulties in commercialising anti-cancer drug nanocarriers can vary wildly from case to case, there are several overarching factors that can be examined, some applicable to targeted drug delivery in general and others more specific to cancer treatment. The next few sections outline the primary barriers occurring at the systematic, microenvironmental and cellular level that most IV-injected nanoparticles encounter on their route to the tumour target, as well as summarising a few physicochemical parameters pertinent to nanoparticle-bio interactions and how they can be individually optimised to improve the chosen nanoparticle's drug-delivery function.

1.2.1. Biological Barriers Faced by Nanoparticles En Route to and at the Tumour Microenvironment

When considering the overall advantages afforded by nanoparticles to ferry drugs, their improvements over small molecules alone are somewhat negligible compared to their promise often emphasised in literature.[18,19] This unfortunately rings true when considering that on average less than 1 % of the nanoparticle's injected dose (ID) manages to reach the tumour to have an effect, as reported by reviews analysing the delivery efficiencies of multiple nanoparticle designs reported in literature over recent years.[20] This an especially unsettling trend, as the reportedly low delivery levels imply that the bulk of the ID either permeates through healthy tissues to ultimately exert cytotoxic side-effects, are cleared through renal and mononuclear phagocyte system (MPS) pathways, or are simply unable to infiltrate cancer cells with adequate levels for reasons associated with the tumour microenvironment. For a nanoparticle to apply its intended effect against its intended cellular targets, it must travel from the site of injection to the tumour cells, all the while surmounting these extensive barriers at different stages of its journey whilst preserving its cargo.

From the site of injection, the first environment the nanoparticle will need to safely traverse is the body's circulatory system.[21] Even for those nanoparticles employing active targeting mechanisms, the ability to repeatedly circulate throughout the body intact is crucial to increase their deposition,[22,23] since the presence of targeting ligands on the nanoparticle surface will not necessarily aid in directing vascular extravasation.[24] Moreover, given that most human tumours often occupy a miniscule fraction of patients' bodies in mass and volume, there is no guarantee that all nanoparticles will extravasate out of blood vessels when they reach the target.[25] Hence, blood circulation lifetimes on the order of hours or even a few days is beneficial to increase the nanoparticle's *in vivo* efficacy,[26] although this

can be a potential problem for cytotoxicity if the chosen nanomaterial drug is not particularly biocompatible.[27] As the nanoparticle traverses the circulatory system, it will have to overcome significant hurdles including opsonisation, a process whereby the particle is tagged with antibodies that mark the nanoparticle for phagocytosis and immune clearance by the cells of the mononuclear phagocytic system (MPS).[28] Although the macrophages and other immune MPS components are interspersed throughout the body, most of them reside within the spleen and liver.[29] These two organs are known to be particularly detrimental to nanoparticles during the circulation stage, ultimately sequestering the majority of injected nanoparticles.[30,31] Aside from opsonisation and subsequent MPS-mediated removal, IV-injected nanoparticles are also highly likely to undergo renal filtration and clearance *via* the kidneys, which receives and processes a substantial volume of blood at any one time (up to 22 % of cardiac output).[25] Assuming a portion of nanoparticles manage to evade these clearance mechanisms, they will then need to marginate towards the endothelial walls of the capillaries at the appropriate moment to extravasate out at the local tumour site.[32] This phase of nanoparticle tumour delivery can be aided by the existence of large fenestrations in the vasculature surrounding tumour tissue.[33]

Following nanoparticle extravasation from capillaries into the tumour interstitium, they will subsequently have to navigate the tumour microenvironment (TME). The TME alone has been known to significantly impede the penetration and therapeutic action of nanoparticles in solid tumours through its unique pathophysiology compared to healthy tissue.[34] As cancerous cells usually proliferate much more rapidly compared to their healthy counterparts,[35,36] the resultant tumour requires a dedicated transport network to support its nutrient, oxygen, and waste requirements that cannot be met by the pre-existing circulatory system alone. This in turn triggers the formation of a greatly disorganised and variable

network of blood vessels with highly fenestrated vessel walls.[34,37]. Apart from this accelerated angiogenesis (blood vessel formation), solid tumours have also been known to feature an abnormal and defective lymphatic network,[38] usually a consequence of the mechanical pressure applied by the solid tumour on pre-existing lymph vessels in the area, triggering their collapse.[39] Without an adequate lymphatic outflow, coupled with their highly permeable vasculature, the TME is usually subjected to a high interstitial fluid pressure (IFP) that induces a net outward flow from the tumour core.[40–42] Given that most nanoparticles and macromolecules would theoretically rely on convective flow to transport them from the surrounding blood vessels to the tumour interstitium, this elevated IFP presents a potential barrier to their migration and penetration of the tumour tissue itself.[43,44] Indeed, a number of studies employing various macromolecular/nanosized complexes have replicated this phenomenon, implicating the high IFP with slowed tumoural intravasation of nanoparticles.[45–47]

Another aggravating factor in suboptimal nanoparticle performance in cancer therapy is the remodelled extracellular matrix (ECM) intrinsic to the TME. Under normal circumstances, the ECM is present in all healthy tissues and organs to provide structural support and facilitate cell-to-cell signalling, taking the form of a three-dimensional network consisting of collagen, proteoglycans, hyaluronan, elastin fibres and other glycoproteins. By contrast, the ECM as part of the TME can undergo drastic alterations, becoming increasingly dense and rigid due to increased levels of collagen deposition and cross-linking, and an increase in hyaluronan and proteoglycan expression. For nanoparticle-mediated drug delivery, these changes to the ECM can significantly hinder diffusion/convection of both small-molecules and nanosized drug carriers.[48] Furthermore, the increased presence of charged biomolecules such as hyaluronan and collagen can compromise the transport of

nanoparticles bearing charged groups through complementary electrostatic interactions, effectively trapping them at the tumour periphery.[49]

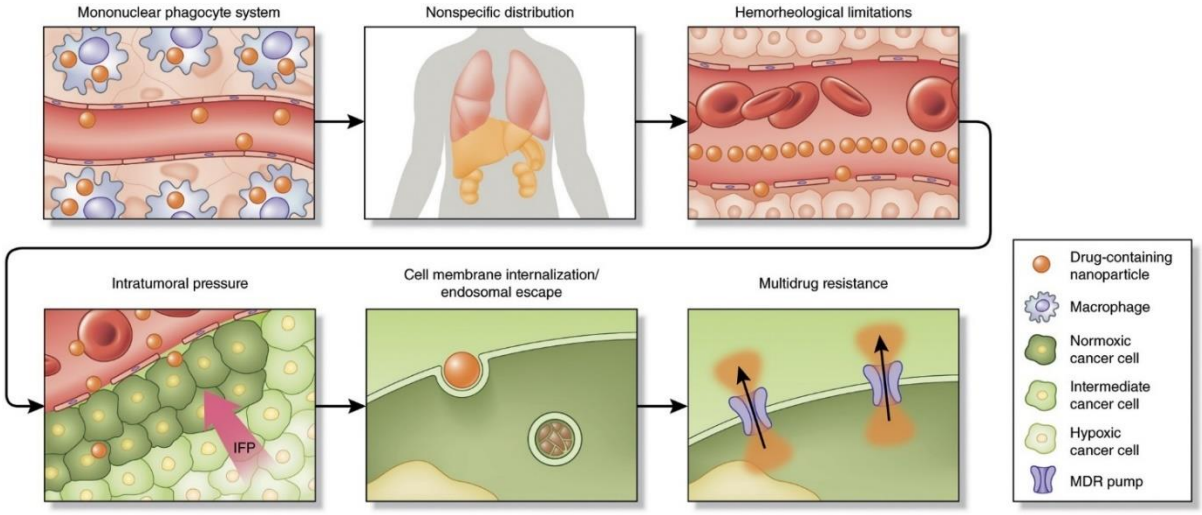

Figure 1.1 Sequential barriers faced by nanoparticles upon their *in vivo* administration and their subsequent journey to and into tumours. Reproduced from Blanco *et al.*, 2015.[50]

As part of ongoing endeavours to improve the anticancer performance of nanoparticles, researchers have frequently cited the so-called "EPR effect" (enhanced permeability and retention effect) as a potential mechanism by which an appropriately sized nanoparticle can experience selective deposition at the tumour site. This phenomenon was first coined by Maeda and colleagues in 1986 after they first observed the greater tumoural accumulation of a high molecular weight polymer-neocarzinostatin conjugate compared to the neocarzinostatin protein alone.[51] Since then, the EPR effect has been extensively mentioned by numerous researchers as forming the basis for passive targeting mechanisms for their preclinical nanoparticle designs. The supposed mechanism of the EPR effect can be divided into two main components. The first component, the 'enhanced permeability', arises from TME's leaky vasculature as previously explained. Such hyperpermeability in the surrounding blood vessels can be sufficient to promote enhanced extravasation of chosen

nanocarriers out of the bloodstream and into the TME. The second feature of the EPR effect, being enhanced retention, arises as a natural consequence of the weakened lymphatic drainage common to most malignant tumours as stated previously. Theoretically, this slowed lymph efflux can work in favour of nanoparticles by extending their residence time at the tumour site and by extension, their chances of infiltrating the tumour matrix and achieving sustained drug release. Despite its initial promise, systematic evaluations of the EPR effect's merit have revealed its inconsistent performance in clinical settings. Indeed, its attempts to improve passive targeting has yielded highly variable results based on tumour type, stage of progression, time, and even between individuals.[52–55] Moreover, much of the significant improvements yielded by this effect have been chiefly documented in rodent models, whereas benefits in larger and more complex human models have remained largely unreliable.[56] In response to these shortcomings, 'active-targeting' functionalisation of nanoparticles has been presented as an alternative to improve targeting specificity. This approach leverages certain receptors or other biomolecules known to be exclusively overexpressed on the target cell or tissue specifically by functionalising a nanoparticle with a targeting moiety on its surface that can be recognised by the chosen receptor/biomolecule. Since the receptor target is ideally chosen so that it occurs in negligible levels on healthy cells, selective uptake into the cancer cell target is favoured over non-specific cell uptake. Studies have already identified and employed several targeting ligands and demonstrated their usefulness in heightening target cell specificity. Folate is one such example of a functional molecule that has been extensively cited and used in the literature, since folate receptors are known to be quite pervasive on the surface of most cancer cells.[57–60] When conjugated with folate groups on their surface, the polymeric micelles constructed by Yoo and colleagues showed improved delivery of doxorubicin (8.7 μg/g of tumour) compared to non-functionalised drug-loaded micelles

(6.3 μg/g of tumour) in mouse xenograft models after 24 h.[61] Similarly to folate, certain peptides such as the angiopep-2 sequence have shown active-targeting capabilities, and can be additionally advantageous in terms of ease of synthesis and cost. In their work on drug delivery to brain gliomas, Xin and co-workers employed angiopep-2-decorated block copolymer nanoparticles to exploit the selective recognition of the peptide by overexpressed αvβ3 integrin proteins. Their findings both *in vitro* and *in vivo* cemented the targeting potential of angiopep-2 compared to non-conjugated controls, which exhibited enhanced glioma cell uptake.[62] Even so, the concept of active-targeting in the nanomedicine field has not been developed without its share of setbacks.

1.2.2. Optimisation of Physicochemical Traits in Tumour-Targeting Nanoparticles

With a growing understanding of the challenges faced by nanosized drug-delivery systems *in vivo*, current efforts to bolster their delivery efficiency and tumour penetration have turned towards nanoparticle design optimisation. The underlying reason is that it has become progressively clear that a nanoparticle's physicochemical parameters hold critical roles in regulating nano-bio interactions, including circulation lifetime,[63] immunogenicity,[64] blood margination,[65] tumour tissue penetration[66] and even the specific endocytic pathway used to internalise the nanoparticle within cells.[67] Given the complexity of the *in vivo* environment and the processes that constitute it, a nanoparticle must be meticulously designed in its physicochemical parameters to satisfy the (sometimes contradictory) requirements imposed by each drug-delivery stage.

Of the various physicochemical factors, size is generally acknowledged as one of the most influential in governing a nanoparticle's behaviour and fate in biological environments.

From the moment of injection, a nanoparticle's distribution can be reasonably predicted on the basis of its size alone, with excessively large particles (>200 nm) tending to be rapidly removed *via* opsonisation/phagocytosis.[68,69] Conversely, particles sized at a few nanometres (< 6 nm) have been known to be excreted by the kidney's renal system or else diffuse through blood vessel walls and into organs indiscriminately.[70] In order to fully exploit the defective tumour vasculature for passive accumulation therefore, intermediate particle sizes are desirable to permit their escape through the fenestrated tumour blood vessels whilst minimising capillary extravasation elsewhere.[63] Post-extravasation and within the tumour locale, the nanoparticle's size also dictates the ease at which it navigates the surrounding ECM and tumour interstitium. As the ECM imposes its own restrictions *via* the numerous gaps in the network, particles larger than these pores will quickly be immobilised before they can reach the main tumour mass.

Morphology or shape of nanoparticles has likewise proven a key influence in governing tumour penetration, circulation lifetime and cellular uptake. During the nanoparticle's circulation in the blood for example, its tendency to marginate to the outer vessel walls under flow has been shown to be significantly influenced by its shape. In particular, margination tends to be facilitated in cases of disc or rod-like morphologies, whose high surface area provides greater access for torque and hydrodynamic forces to act upon and push them to the outer vessel walls for extravasation.[71,72] Circulation half-life has also demonstrated to be prolonged through use of non-spherical nanoparticles with high aspect ratios, including filamentous, rod-like or worm-like shapes.[73] The role of shape is also apparent in the internalisation pathway(s) used and overall tumour accumulation of the chosen nanoparticle. Every other variable constant, nanoparticles presenting an elongated face or surface (as is the case with rods and disc-like shapes) to the cell membrane have exhibited quicker cell membrane association than their spherical counterparts.[74] However,

the greater cell adhesion rates of such nanoparticles tends to be offset by lower internalisation rates, posited to be a consequence of the higher energy requirements for deforming and wrapping the membrane around a larger surface area. Nanoparticle tumour penetration also reveals a shape-dependence that has been observed in nanoparticles of different materials, although results vary widely depending on the material used. While some have reported the greater efficiency of nanospheres in being internalised in tumour models, others have observed that nanorods outperform their filamentous or spherical counterparts when penetrating into 3D tumour spheroids.[75]

Certain aspects of a nanoparticle's biological behaviour can be drastically affected by surface charge and functionalisation. From a drug-delivery standpoint, nanoparticle surface charge is challenging to optimise as the nanoparticle may require different surface charges at different points along its journey. In particular, opsonisation of nanoparticles tends to be enhanced on surfaces presenting net negative charges, whilst positively-charged particles undergo accelerated clearance due to their aggregation with negatively charged serum proteins.[76,77] For extension of circulation half-life, it is generally acknowledged that zwitterionic or neutral nanoparticles perform the best in that regard.[78] On the other hand, comparisons of charged and neutral surfaces prove the clear advantages of cationic surfaces in increasing nanoparticle tumour penetration.[79,80] Given the contrasting effects of charged vs neutral nanoparticles on circulation lifetimes and tumour penetration, an idyllic nanoparticle drug carrier would be able to exploit a neutral surface charge for extended circulation lifetime but a cationic surface to encourage tumour cell uptake and penetration. Recent efforts have already been made on realising such a 'charge-switching' tumour-targeting design with some success.[81–83]

1.3. Altered Biological Interactions of Nanoparticles by the Protein Corona

Apart from suboptimal site accumulation and poor penetration of tumour tissue, engineered nanocarriers must also contend with drastic changes to their identity from the protein corona (PC), a term first coined by Cedervall and colleagues in 2007.[84] This corona arises whenever nanoparticles are exposed to biological fluid, causing its surface to be rapidly encased with a layer of proteins and other biomolecules. Previous studies have already established the high complexity and dynamic nature of the PC. As it forms on the nanoparticle, the PC's identity will not remain static, but rather results from the establishment of an equilibrium of protein adsorption/desorption events over time, termed the Vroman effect. As part of this effect, PC will initially favour the adsorption of highly abundant, low-affinity proteins with fast exchange rates. With time however, these low-binding proteins will be substituted with slow-exchange proteins with higher binding affinities.[84,85] Within literature, the layers formed by both classes of proteins are occasionally referred to as the "hard" and "soft" protein coronas. The hard corona comprises those proteins bearing high binding affinities and low exchange rates. Accordingly, this layer is often found deposited directly on the nanoparticle's surface, whereas the more loosely bound, labile proteins of the soft corona materialise around the outer edge of the hard corona. Remarkably, the latter proteins that persist longer as part of the hard protein corona are usually found in low concentrations in blood serum, emphasising the influence of other factors beyond the serum composition of the nanoparticle's local environment in solely determining the corona's final composition. Indeed, the physicochemical traits of the pristine nanoparticle itself, including surface chemistry, size, surface charge, shape, stiffness and curvature have also been identified as driving forces in modulating various aspects of the corona such as thickness, protein composition and degree of protein unfolding.

Due to the high degree of protein coverage on the pristine nanoparticle surface, the engineered 'synthetic' identity of the nanoparticle is effectively superseded by a new 'biological' identity presented by the PC. From a drug-delivery standpoint, the nanoparticle-protein corona has shown to have substantial influence of key variables of the nanoparticle's subsequent biological interactions, such as biodistribution, immunogenicity, cytotoxicity and cellular uptake. Given this, full comprehension of the formation and composition of the protein corona has become a vital step in optimising the design of any drug-carrier nanoparticle to avoid undesirable changes that could compromise its therapeutic performance.

Armed with this understanding, scientists have demonstrated novel methods for reducing and even controlling protein adsorption onto nanomaterials *via* customisation of the nanoparticle surface. Yet, there is still substantial debate on the precise way that the resultant protein corona is shaped by these parameters. Apart from common variables such as size and surface charge, the hydrophobicity of the chosen nanoparticle has been shown to play a role on the protein corona's final composition wherein greater surface hydrophobicity tends to promote increased protein adsorption. Apart from the quantity of proteins adsorbed however, the role of hydrophobicity on other aspects of the protein corona such as its specific make-up has remained mostly unexplored or inconclusive.

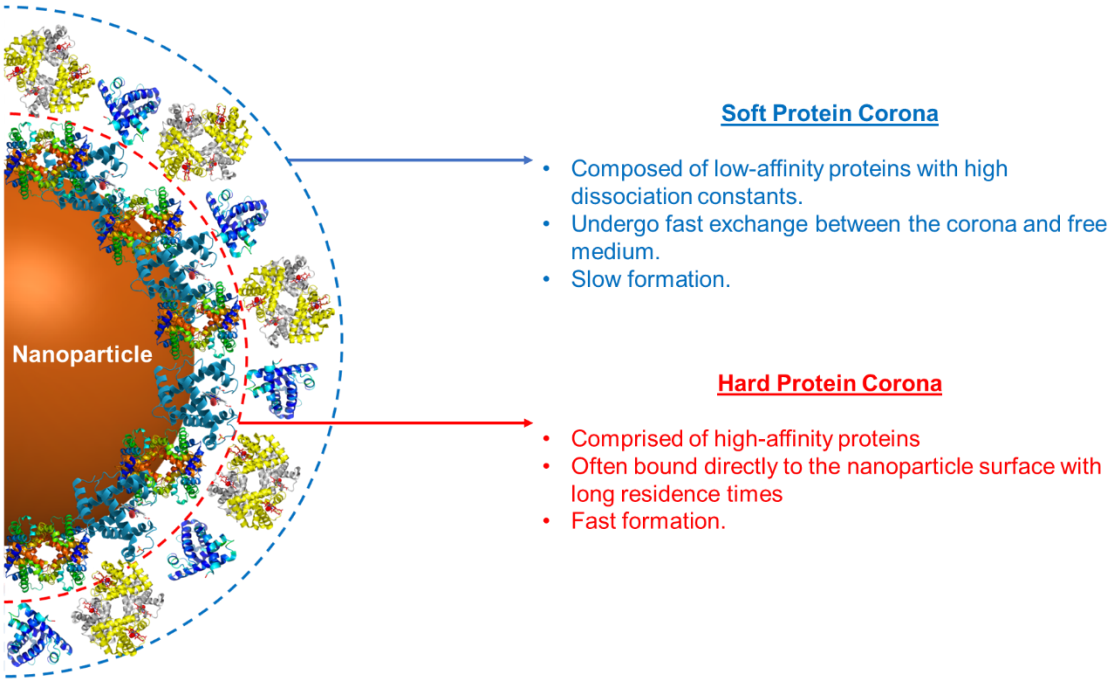

Figure 1.2. Representative schematic of the protein corona formed almost instantaneously upon a nanoparticle's exposure to biological fluids, comprising the hard and soft corona components.

1.4. Current Status of Polymeric Nanoparticles in Cancer Therapy

The nanomedicine field has so far managed to exploit a broad array of material types, both organic and inorganic, as the basis for nanoparticles in biomedical applications. One such class, polymeric nanoparticles, have proven especially capable of delivery of anticancer pharmaceuticals with high efficacy and selectivity due to their facile and established synthesis, ability to ferry drug cargoes with high loading capacity, and their modular structure which allows for precisely controllable physicochemical characteristics and functionalisation with bio-targeting or bio-responsive groups. Outside of academic research, a few polymer-based nanosystems have even managed to enter the oncology market in the form of polymer-drug conjugates and drug-loaded polymeric micelles, although their prevalence here falls short in comparison to lipid or protein-based

nanoparticles.[16,86,87] The earliest known instance of polymer-based nanoparticles first appeared as drug-infused silicon capsules synthesised by Folkman and Long in 1964, who demonstrated the ability of the silicone matrix to entrap and induce prolonged discharge of isoprenaline.[88] Since then, a number of polymeric architectures, particularly micelles, utilising different targeting modes and therapeutic loads have independently been approved for public use (some regionally) for the treatment of different cancers. Such approved formulations include Genexol-PM®, a treatment consisting of paclitaxel encapsulated within PEG/poly(D,L-lactic acid)-based micelles that have been tolerated well by breast cancer and non-small cell lung cancer (NSCLC) patients.[89] In the interim, other polymeric nanoparticles such as Paclical (polymeric micelle formulation containing paclitaxel for ovarian cancer treatment)[90], Calaspargase pegol (PEGylated L-asparaginase II used to treat acute lymphoblastic leukaemia)[91] and even the dendrimer AZD-0466 (intended for haematological cancers)[92] have progressed to Phase II and Phase III trials with promising prospects for their market suitability. Apart from polymer-drug conjugates and polymeric micelles, MPBs have demonstrated their ability to compartmentalise therapeutic cargo and deliver it selectively and efficiently in preclinical research.

1.5. Reversible Deactivation Radical Polymerisation (RDRP) Techniques

As previously discussed, successful delivery of a therapeutic drug to tumours is an arduous and complex matter, necessitating robust nanoparticle designs with precisely engineered attributes to overcome each of the biological barriers the nanoparticle will face on its journey. In that regard, current literature focused on the field of anticancer polymeric drug vehicles have adopted synthetic polymers in various forms, including nanosized hydrogel particles, block copolymer micelles, dendrimers, polymer drug-conjugates, and

polymersomes.[93,94] All of these aforementioned architectures can now be engineered with distinct sizes, size distributions, surface charges and surface chemistries, a feat that would not have been attainable without the emergence of RDRP techniques.

Historically, the preparation of synthetic polymers bearing narrow molecular weight distributions, complex architectures and a wide selection of functional monomers has been a problematic affair. In the years since the pioneering work of Staudinger establishing polymer chemistry as a dedicated scientific field,[95] breakthroughs in polymerisation techniques occurred with the establishment of early step-growth polymerisations and chain-growth polymerisation. Since then, these techniques have been deployed for the widescale production of commercial polymers even today, which has been further aided by the development of reliable polymerisation catalytic systems such as those devised by Ziegler and Natta in the 1950s.[96–98] For all their applicability in industrial polymer manufacture however, their inability to synthesise polymers with complex morphologies and poor control over the final molecular weight makes conventional step-growth and chain-growth techniques ill-suited for the synthesis of precisely-defined, multifunctional polymers necessary for biomedical applications. With the advent of a series of 'living ionic polymerisation' techniques that emerged from the work of Szwarc, Grubbs and Higashimura, the scope of achievable polymer architectures was expanded to include copolymers incorporating multiple monomer types, with high retention of end-groups and good control over molecular weight distribution.[99–101] The hallmark 'living' character that confers these benefits stems from the systems' complete exclusion of termination and transfer reactions that would usually lead to premature formation of 'dead' chains and subsequent broadening of the molecular weight distribution (dispersity). Nonetheless, the suitability of most living ionic polymerisation techniques for creating fine-tuned polymeric nanoparticles is still limited by their need for strictly controlled reaction conditions,

involving complete exclusion of even trace amounts of oxygen or water. Additionally, their aversion to certain functional groups such as amines and hydroxyl groups limits the choice of monomers that they can be used for.

Since its conception, RDRP techniques have become some of the most valuable techniques in the synthetic toolbox of the polymer chemist. Fundamentally, this suite of techniques draws on some of the mechanistic features while improving upon living ionic polymerisations, such as its instantaneous initiation rates compared to propagation. Unlike living ionic polymerisations however, RDRP techniques accomplish this through the incomplete suppression of termination and transfer reactions, rather than absolute preclusion. Specifically, this involves a suitable compound as a deactivating agent to reversibly revert active radical chain species into a dormant state, thereby halting propagation. Since activation-deactivation proceeds far faster between chains than their propagation, all chains are conferred similar growth rates and thus achieve similar sizes, while termination and chain transfer are still mostly suppressed. In this manner, the final polymeric products are yielded with easily controllable molecular weights and narrow molecular weight distributions. Improving upon the limited versatility of living ionic techniques, most RDRP techniques exhibit a far greater tolerance to a wider variety of monomer functional groups such as amines, carboxylic acids, alcohols, esters and halogens. Present RDRP techniques include RAFT (reversible addition-fragmentation chain-transfer) polymerisation, ATRP (atom transfer radical polymerisation) and NMP (nitroxide-mediated radical polymerisation), which all operate through establishing an active-dormant chain equilibrium but *via* different methods and reagents. Within the scope of this work, the concepts of RAFT and ATRP will be elaborated further since they were used to prepare the molecular polymer brushes (MPBs) used in this study.

1.5.1. Atom Transfer Radical Polymerisation (ATRP)

The beginnings of ATRP can be traced back to independent investigations into the conducting living free-radical polymerisations *via* transition metal complexes, led by Matyjaszewski's and Sawamoto's groups in 1995.[102,103] Since then, it has become a greatly ubiquitous technique for the preparation of complex polymer morphologies for myriad applications. Like any RDRP technique, the underlying principle of ATRP involves temporary deactivation and activation of propagating radical chains to ensure their coordinated growth and thus minimise their dispersity.[104]

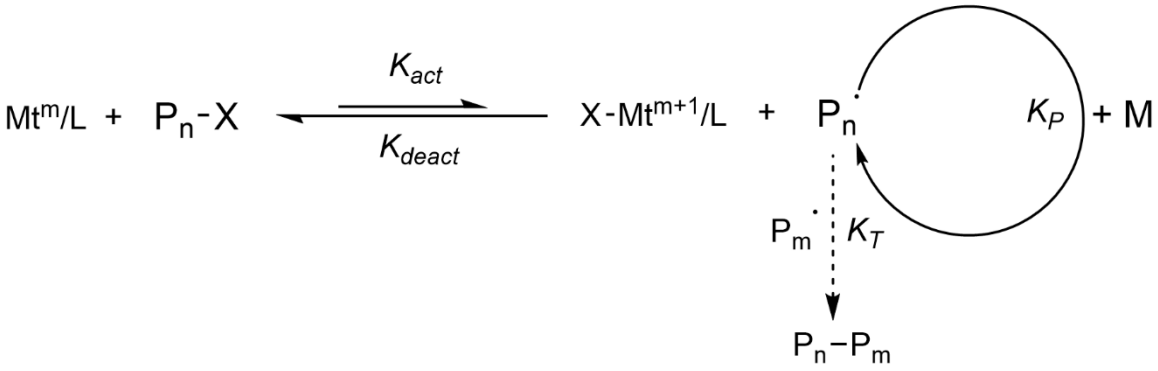

Figure 1.3. The primary equilibrium comprising the mechanism of ATRP.

Figure 1.3 illustrates the core components and mechanism that drives ATRP, which includes a metal halide in oxidation state *m* (denoted $\mathbf{Mt^m}$) complexed to a suitable ligand (**L**), and the chosen monomer (**M**). To activate the alkyl halide initiator, the metal-ligand complex (usually copper-based) reacts with the initiator with an activation rate constant (K_{act}) to free a radical species ($\mathbf{P_n^{\cdot}}$) through homolytic cleavage of the latter's halide group, whilst oxidising the metal halide complex($X\text{-}Mt^{m+1}$). From here, the free radical species can either form a propagating chain by reaction with the monomer (**M**) with a certain

propagation rate constant (K_P), self-terminate by reacting with another propagating chain ($\mathbf{P_n}$) with a termination rate constant (K_T), or undergo a temporary redox process with the metal-halide complex with a rate constant of K_{deact} to reduce the latter back to its lower oxidation state and form a deactivated halogen-terminated polymer chain. This deactivation reaction, as in any RDRP process, is crucial in ATRP for narrowing the final molecular weight distribution. Thus, K_{deact} under an ideal set of ATRP conditions must be sufficiently large such that the equilibrium lies mainly to the left, where the majority of chains are in the dormant state and the concentration of radical species are reduced. This ensures that the chances of radical-radical chain termination reactions are minimised and grants the chains their 'living' character that allows them to be extended if desired through retention of chain-end functionality.

Although ATRP has been successfully carried out using a range of transition metals such as iron,[105,106] cobalt,[107] nickel,[108,109] and ruthenium,[110,111] copper remains the most frequently used choice of metal for the catalytic complex for its availability, low cost, and high catalytic activity when paired with nitrogen-containing ligands.[112,113] Nevertheless, the use of a transition metal catalyst (sometimes at substantial concentrations) in a conventional ATRP reaction can be a drawback, since the copper residue contaminating the obtained polymers may render them unsuitable for biomedical applications.[114] While procedures exist for catalyst removal, this requires further purification steps and generates extra chemical waste. Another limitation associated with standard ATRP procedures is that the cuprous halide catalyst must be preserved in its lower oxidation state (I) when introduced and ideally maintained as the majority ion species in equilibrium with the deactivator X-Mt^{m+1}/L throughout the reaction. For this, most ATRP reactions require degassing using appropriate methods (freeze-pump-thaw or inert gas sparging) before

catalyst addition to safeguard it against oxidation by atmospheric oxygen, which in turn makes the reaction more time-consuming.

Since several of the setbacks hindering classic ATRP stem from its reliance on a lower oxidation state copper catalyst, a few variations of ATRP methods have been developed recently that drastically reduce the amount of catalyst needed to as little as a few parts per million. These techniques, such as ARGET (Activator Regenerated by Electron Transfer) ATRP,[115] ICAR (Initiator for Continuous Activator Regeneration) ATRP, and eATRP (Electrochemically-mediated ATRP) employ different approaches to reducing the amount of copper(I) needed through continuous regeneration of the Cu^{I} species from Cu^{II}.[116] This is achieved either through an externally introduced reducing agent or radical source (in the case of ARGET and ICAR ATRP respectively),[117] or *via* electrochemical means (in eATRP).[118]

1.5.2. Reversible Addition-Fragmentation Chain Transfer (RAFT) Polymerisation

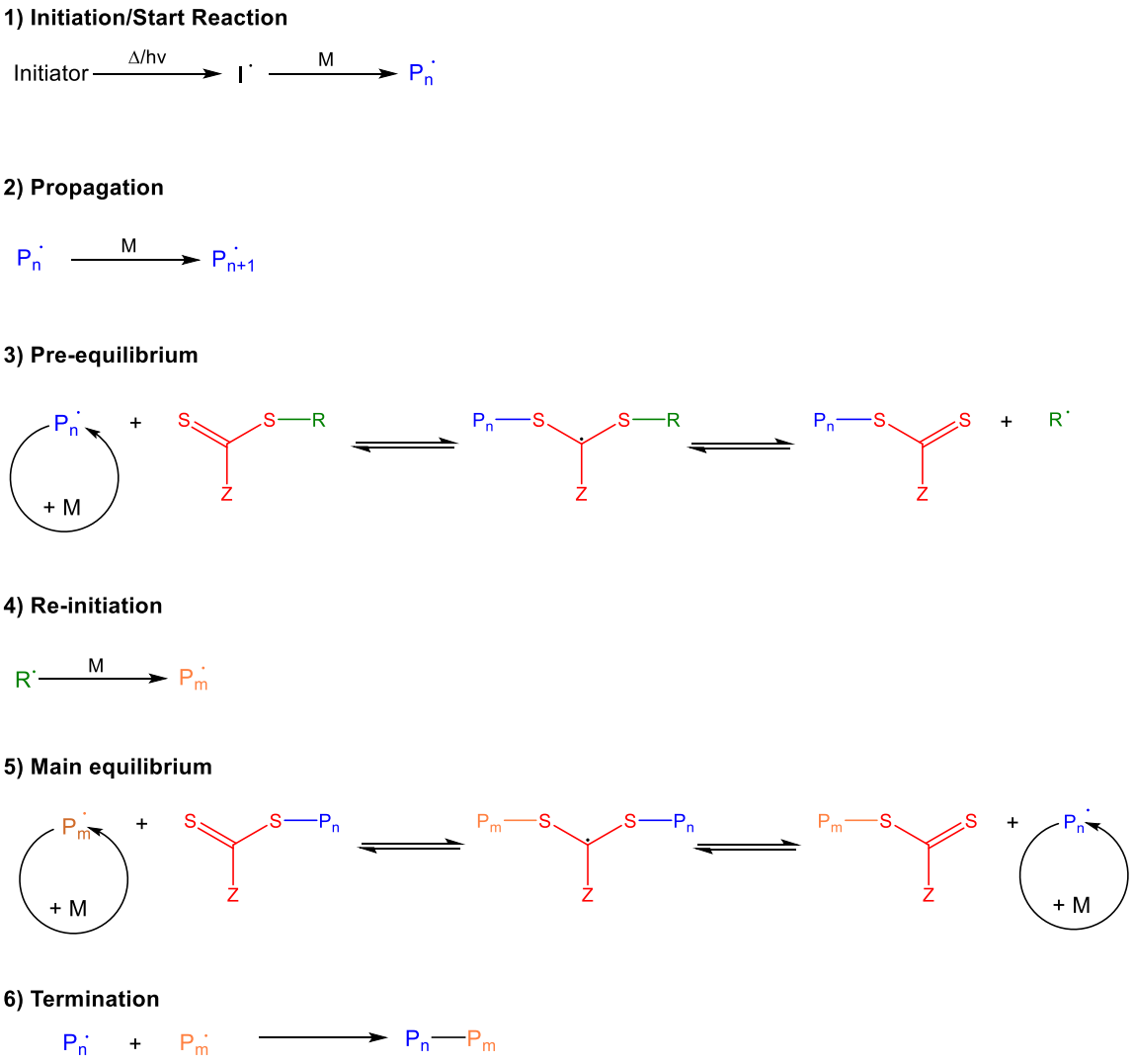

Figure 1.4. Key steps comprising the mechanism of RAFT polymerisation.

Much like the other RDRP techniques, RAFT polymerisation has likewise proven a robust tool for production of structurally complex polymer architectures, including stars,[119] combs,[120] and gradient copolymers.[121,122] Compared to ATRP, RAFT has the added advantage of being able to conduct polymerisations more easily in aqueous environments, and generally has a wider tolerance to different monomer functional groups. First reported

by Moad, Rizzardo, Thang *et al.* in 1998,[123] the RAFT technique relies on a degenerate chain transfer process for reversible chain activation-deactivation mediated by a chain transfer agent (CTA). A typical CTA features a thiocarbonylthio group bearing two customisable substituents; an 'R' and 'Z' group, that dictate the efficiency of the polymerisation depending on several factors. The RAFT process (outlined in **Figure 1.4**) begins with the thermal or photo-induced decomposition of a radical initiator to produce radical species (**I$^{\bullet}$**), which can subsequently form propagating radical chains with a degree of polymerisation (DP) of *n* (**P$^{\bullet}_{n}$**) through their reaction with monomers (**M**). Eventually, the growing radical chain (**P$^{\bullet}_{n+1}$** or **P$^{\bullet}_{n}$**) is entrapped by reaction with the thiocarbonylthio group of the CTA to generate a transient CTA-chain adduct species. At this stage, the adduct can reversibly undergo homolytic cleavage to release either the radical R group or the previous radical chain species. Depending on the group released from the adduct, a new growing polymeric chain (**P$^{\bullet}_{m}$**) is re-initiated by reaction of the radical R$^{\bullet}$ species with unreacted monomer, or the previous chain **P$^{\bullet}_{n}$** polymerises further. With time, a continuous series of rapid fragmentation-addition events between the different chain radicals (**P$^{\bullet}_{n}$** and **P$^{\bullet}_{m}$**) and the CTA occurs to set up an equilibrium to allow all the chains to grow at the same rate. At any point during the reaction, bi-radical termination events can occur (albeit on a small scale) between radical chain species, generating 'dead' chains that cannot polymerise further.

A controlled RAFT polymerisation will yield narrowly defined polymers with predictable molecular weights, so long as the reaction predominantly favours chain addition-fragmentation over chain propagation and all initiation events complete early in the reaction. To that end, selection of the CTA with the appropriate R and Z groups is of utmost importance, due to the role these groups play in establishing the position of the chain transfer equilibria. In the case of RAFT, the 'Z' group primarily exists to stabilise the intermediate

CTA adduct radical and consequently influences its reactivity towards propagating chain radicals. With a diverse selection of monomers available for RAFT (e.g. (meth)acrylates, acrylates, vinyl acetates, styrenes, (meth)acrylamides), the Z group is ideally chosen so as to be compatible with the monomer choice, depending on whether the monomer(s) are "more-activated" (MAM) or "less activated" (LAM). Alongside the Z group, the R group must also be optimised to serve as a good homolytic leaving group compared to the propagating chain, whilst being able to efficiently re-initiate polymerisation. Since its inception, several CTAs have been devised and synthesised with guidelines to select the best agent for different monomer classes.

1.6. Molecular Polymer Brushes and their Applications in Nanomedicine

1.6.1. Overview and Features of MPBs

Polymer bottlebrushes (also known as molecular polymer brushes; MPBs) are an interesting class of synthetic macromolecules with unique properties compared to their linear counterparts. As their name insinuates, these polymers are structurally analogous to bottlebrushes, since their architecture consists of a polymer chain (often termed the 'backbone') appended with numerous polymer sidechains along its length. The sheer density of grafted sidechains on the supporting backbone confers a few interesting properties to MPBs. For one, the proximity of sidechains close to each other has the effect of forcing the backbone into a stretched state, as opposed to the coiling normally adopted by simple linear polymers. This occurs to minimise steric entanglement between sidechains, which in the case of MPBs with sufficiently large aspect ratios, allows them to assume anisotropic worm- or rod-like shapes. Where the aspect ratio is closer to 1 (i.e. in

MPBs with sidechains equal in length or longer than the backbone), star-like or nominal spherical structures can be achieved. Ultimately, the strength of steric repulsion between sidechains can be manipulated by methodically controlling the MPBs grafting density, sidechain length and backbone length, by extension granting access to anisotropic or isotropic structures that would be normally challenging to achieve synthetically.

Initial attempts to prepare MPBs began with the work carried out by Yamashita *et al.* in 1989.[124] Using polystyrene (PS) chains functionalised with a terminal methacrylate group, their group was able to synthesise star-like MPBs *via* conventional free radical polymerisation (FRP). Since then, further advancements in polymerisation techniques, such as the introduction of RDRP (see previous section), have drastically expanded the synthetic latitude of achievable MPB compositions. Fuelled by advances in macromolecule characterisation techniques such as size-exclusion chromatography (SEC), atomic force microscopy (AFM), electron microscopy and small-angle scattering techniques among others, researchers have managed to overturn MPBs from a relatively undistinguished polymer class to fundamental materials for a range of applications and research areas.[125]

1.6.2. Synthetic Routes towards MPBs

Up to the present, three general strategies for MPB synthesis have been cultivated, and are differentiated according to the manner sidechains are attached or formed on the backbone. They are named the "grafting-from", the "grafting-to" and "grafting-through" strategies, each bearing its own advantages and limitations. In the "grafting-to" strategy, fully formed sidechains are attached to the backbone *via* complementary functionalities. One key

advantage of this approach is that it allows for complete characterisation of both components before grafting. Moreover, organic synthetic methods have progressed to such a degree to grant an abundance of options in terms of robust coupling chemistries. Of these chemistries, copper-catalysed click chemistry has perhaps remained the most widely used approach, although examples of grafting-to *via* Diels-Alder cycloaddition[126,127] and thiol-ene/yne chemistry[128–130] also exist in literature. Despite the presence of well-established attachment chemistries, the grafting-to method has the most difficulty yielding MPBs with high grafting densities out of the three strategies. This can be attributed to the high steric congestion associated with inducing bulky, pre-formed polymer sidechains to react with complementary sites that often make up a small molar fraction of the whole backbone. Unfavourable entropic costs also come into play as sidechains are forced to uncoil to better access the backbone's reactive sites. This unreacted fraction of sidechains can pose a problem in subsequent purification steps. While these issues can be slightly amended to ensure MPBs are created with almost one sidechain for every backbone unit, shortening of sidechains is often required as a trade-off.

The "grafting-through" strategy is based on using "macromonomers" consisting of pre-formed sidechains decorated with a polymerisable pendant group on one end to construct MPBs. As the macromonomers are polymerised *via* their end-groups, MPBs are formed with quantitative grafting densities, since each backbone unit is formed with a sidechain already attached. Because of the unique means by which MPBs are grown, the grafting-through method has been particularly useful in generating hemispherical block MPBs featuring chemically distinct domains separated along the backbone. Moreover, akin to grafting-to, thorough characterisation and functionalisation can be performed on the macromonomers before their polymerisation, facilitating MPB fabrication with well-defined and multivalent characteristics. For this reason, polymeric nanomedicine has

expressly exploited the grafting-through method to produce well-defined MPB architectures for drug-delivery and nano-biological studies, more frequently than with grafting-to and grafting-from. However, the MPBs produced by this strategy are known to suffer from exceptionally short backbone lengths due to steric constraints imposed by polymerising bulky macromonomers onto the already large and growing bottlebrush. Much like grafting-to, the incomplete conversion of the reactants also complicates purification due to the presence of high-molecular weight macromonomers remaining in the reaction.

The "grafting-from" method sets itself apart from the previous synthetic strategies since it relies on in situ polymerisation of sidechains from a 'polyinitiator' backbone (i.e., a backbone bearing suitable polymerisation-initiating sites along its length). This approach already improves on the steric issues common to grafting-to and grafting-from that restrict achievable backbone lengths and sidechain grafting densities. Since backbones are formed separately before the MPB is assembled in grafting-from, they can be formed with high DPs. Additionally, greater sidechain grafting densities can be attained because monomers are added sequentially as small molecules instead of as polymerised entities to gradually 'grow' the sidechains at the backbone's periphery, thereby avoiding steric complications. Using grafting-from also facilitates post-synthetic purification compared to grafting-to and grafting-from, as the unreacted reagents mostly consist of small-molecule monomers and catalysts that can be easily removed using techniques such as dialysis or selective precipitation. On the other hand, the grafting-from strategy is limited in that the final MPB products are not as narrowly defined in their molecular weight range due to factors such as grafting efficiency, termination/intermolecular coupling reactions, and differences in monomer reactivity in the case of copolymeric sidechains. Determination of the final grafting efficiency is therefore more cumbersome using this technique compared to the

alternatives, as it requires additional post-polymerisation steps for sidechains to be detached and then characterised.

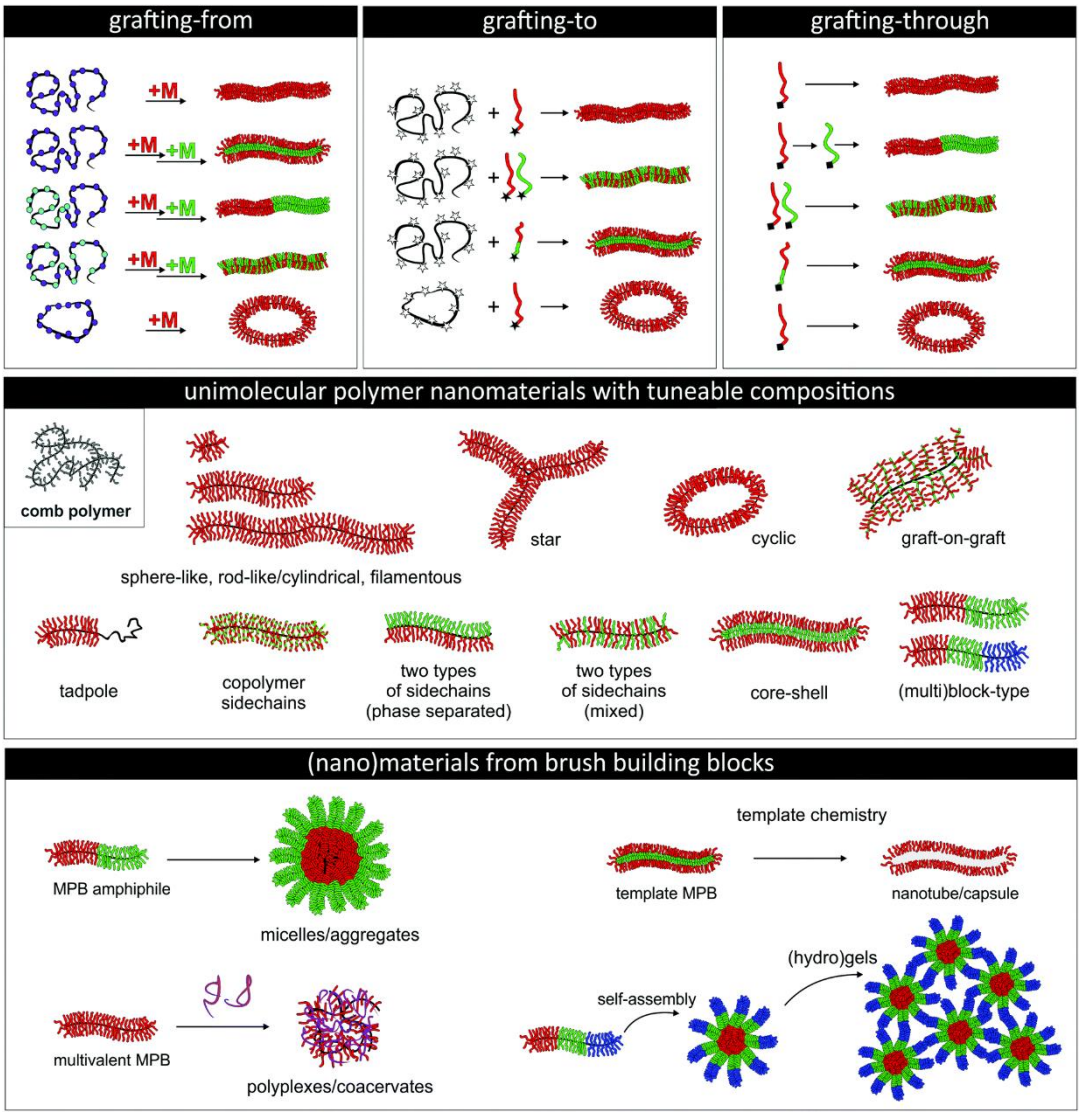

Figure 1.5. Overview of synthetic strategies towards MPBs (top panels), highlighting the grafting-to, grafting-from and grafting-through approach. Achievable unimolecular compositions and morphologies (star, cyclic, brush-on-brush) using MPBs (middle panel), and more complex architectures attained through use of MPBs as building blocks in a self-assembly or templating approach (bottom panel). Adapted from Muellner *et al.*[131]

1.6.3. Current Applications of MPBs in Cancer Nanomedicine

With the establishment and improvement of robust synthetic routes and choice of post-functionalisation, MPBs are gaining traction in the drug-delivery field. Aside from unprecedented morphological control, MPBs hold a few extra advantages over other nanomaterials that make them appealing as drug-delivery systems. Much of these benefits chiefly originate from the 'bottom-up' approach to their synthesis (as discussed previously) that allows them to compartmentalise drug cargoes as well as other functional moieties within the same structure. This feature is best exemplified in MPBs bearing "core-shell" arrangements, in which block copolymers are used as sidechains to introduce chemically distinct properties into the same molecule. Various studies have already exploited this design for drug-loading by incorporating a 'core' sidechain block (the region of the sidechains proximal to the backbone) that can be conjugated to the drug of choice, protecting it from premature excretion and degradation and lengthening its blood circulation time. In one such example, Bai *et al.* managed to synthesise a core-shell MPB particle loaded with the hydrophobic anticancer drug camptothecin (CPT) with the intent to increase its long-term stability and specific targeting of tumour cells by exploiting the drug's reductive-responsiveness within the TME.[132] This was achieved by ATRP polymerisation of a camptothecin-functionalised monomer from a cellulose backbone, followed by chain extension with a hydrophilic oligo(ethylene glycol) methyl ether methacrylate (OEGMA) block to impart water solubility. Notably, the final unimolecular nanoparticles all showed improved cell apoptotic activity (59.4 %) against HeLa cervical cancer cells for *in vitro* assays compared to free CPT (43.0 %), whilst concurrently exhibiting reduced toxicity against a non-cancerous L929 cell line. More than that, encapsulation of CPT in the MPBs' cores also improved the drugs pharmacokinetic profile in tumour-free mouse models, with all tested MPBs exhibiting greater blood circulation

lifetimes than free CPT up to 24 hours after injection. In a similar vein, Guo *et al.* entrapped a model drug (doxorubicin) with relatively high loading levels (16.7% by weight) within the poly(L-lactide) core of an amphiphilic block bottlebrush polymers, albeit *via* simple physisorption. In conjunction with the MPBs outer PEG (polyethylene glycol) shell decorated with active targeting and a radiolabelling moiety, the chosen tumours (4TI breast cancer) could be specifically targeted and subjected to high therapeutic doses by the MPBs under acidic conditions *via* active and passive means (60% doxorubicin release over 76 h). Simultaneously, complexation of the integrated imaging ligand (1,4,7-triazacyclononane-N, N′,N-triacetic acid; NOTA) with ^{64}Cu enabled tumour imaging by PET (positron emission tomography) and allowed for precise quantification of the targeting nanoparticles within the imaged region.[133] Their work effectively showcases the multifunctional capabilities of MPBs on a single platform that would make them valuable in cancer theranostics.

Aside from their applications in entrapping and transporting drug loads, MPBs are emerging as a model platform for investigating nanoparticle physicochemical parameters in a biological context. Through incorporation of monomers with different chemistries, along with their unimolecular nature, this polymeric class uniquely presents modifiable aspects that can be tuned independently of each other. As an example to illustrate this orthogonality, a series of two MPBs made by Niederberger *et al.* was made with comparable aspect ratios, surface charge/functionality and sizes but varied stiffness levels as evidenced by small angle-neutron scattering (SANS) analyses. The modulation of stiffness in this work was achieved by the simple incorporation of a tert-butyl methacrylate (tBMA) sidechain core along with an OEGMA corona. Due to the higher glass transition temperature of the former, the resultant MPB was endowed with greater stiffness than the MPB featuring no tBMA core. In vitro evaluations of the two MPB species' intracellular

localisation revealed significant differences, with stiffer MPBs tending to aggregate in mitochondria whilst the more flexible MPBs being entrapped in vesicles.[134] In a similar vein, Müllner *et al.* demonstrated the aspect-ratio dependence of nanoparticle tumour penetration using MPBs as the platform of choice. Their MPB synthesis approach was able to solely control for nanoparticle aspect ratio by varying the backbone DP and maintaining a constant sidechain DP and monomer composition. Similarly, their findings using 3D multicellular tumour spheroids (MCTS) showed rod-like MPBs overtaking filamentous and spherical nanoparticles in tumour accumulation.[75] The favourable performance of rod-like topologies was independently corroborated by the findings of Li *et al.* in 2018, who tested different MPB shapes in 2D, 3D and *in vivo* cancer models.[135] Aside from a tuneable platform to test anti-cancer behaviour, structure-function-property studies leveraging MPBs have also extended to other biological factors important for nanocarriers, such as protein adsorption. One such investigation by Saltzman *et al.* examined how protein adsorption could be modulated by altering the surface topography of nanoparticles, normally challenging using linear polymer chains but achievable in this case using asymmetrical/symmetrical block MPBs.[136] The self-assembled constructs formed from these MPBs were able to exhibit different levels of surface roughness and widths of the brush terminals. Ultimately, both were implicated in governing the adsorption levels of a model protein onto the nanoparticles as well as their uptake into a HeLa cancer cell line.

1.7. Thesis Methodology

The general aim of this thesis can be summarised as investigating the potential role that nanoparticle hydrophobicity may play on key aspects of their biological interactions in a complex in vivo environment, with a particular focus on those relevant to tumour-targeting nanoparticles. Consequently, the second chapter of this work will investigate how nanoparticle hydrophobicity may affect their association with cancer cells, as well as their passive accumulation and retention in tumour tissue in vivo. In the third chapter, the complexity of the in vivo environment is further considered, as the work diverges to examine how nanoparticle amphiphilicity may impact their association with proteins ubiquitous in serum. Due to the challenging nature of analysing nano-bio associations in a complex multi-component mixture such as blood serum, a model protein is later singled out to test the interactions of the chosen nanoparticles as a function of hydrophobicity. Finally, the potential effect of the hydrophilic-hydrophobic balance on cell membrane interactions by nanoparticles will be tested using biomimetic lipid membranes. The following section outlines the methodology by which these thesis aims were planned and accomplished and provides background information on selected techniques that are particularly important to this study.

The Investigation in the second chapter leverages the versatility and good molecular weight control of RDRP techniques (as discussed beforehand) to produce a library of four MPBs. MPBs provide an appropriate level of compositional versatility (through incorporation of monomers bearing different chemistries) whilst also enabling orthogonal tuning of single parameters. These two features are advantageous in the context of this structure-function-property study since it firstly; 1) permits MPBs to be synthesised with different amphiphilicity levels and 2) allows this to be achieved while leaving other important

physicochemical aspects (size, shape, surface charge) relatively constant. This allows us to make our analyses of the MPBs biological behaviour through the lens of hydrophobicity alone. As important as the synthesis of these materials is their robust characterisation. To that end, techniques including ^{1}H-NMR spectroscopy and size exclusion chromatography are used to characterise the nanomaterials at different stages of synthesis and functionalisation. SEC is a commonplace characterisation technique in polymer chemistry that allows the molecular weight distribution (otherwise known as the 'dispersity') of a polymer sample to be determined, along with its molecular weight. Akin to most chromatographic techniques, SEC performs separation (albeit by molecular weight) of macromolecules using a series of solid-phase columns featuring pores with well-defined sizes in the inner packing material. As polymer samples of varied sizes traverse through this solid phase, size-dependent separation occurs as smaller sized samples spend more time traversing through and in the pores to ultimately elute later, whilst larger samples conversely elute out of the column quicker, as their size curbs their pore penetration. A detector (or series of detectors) positioned at the end of the column circuit subsequently determines the hydrodynamic volume of different size fractions as they elute through, which in tandem with an appropriate standard curve can extrapolate the molecular weight and dispersity of the sample.

With an appropriately characterised and functionalised amphiphilic MPB library, a variety of in vitro experiments employing cancer cell lines are used to test the effects of nanoparticle amphiphilicity on their cellular association, starting with simple two-dimensional (2D) monolayers. Despite their simplicity, they are still appealing for their facile handling and maintenance. Furthermore, their two-dimensional nature facilitates analysis using methods such as confocal laser scanning microscopy (CLSM) and can yield high resolution data on how nanoparticles are internalised in specific locales within the

cells. Nonetheless, the initial in vitro results in the first chapter are insufficient in replicating how the MPBs would behave in a complex TME. To address this, multicellular tumour spheroids (MCTSs) will be used next to provide a clearer understanding of how each MPBs' hydrophobicity might affect its efficiency in penetrating much denser tumours. Between 2D monolayer models which sparingly capture the physiological intricacies of clinical tumours, and in vivo animal models which are costly, more time-consuming and present more in vivo factors that complicate assessment of nanoparticle performance against tumours alone, MCTSs provide an excellent middle ground. Fundamentally, MCTSs are grown from cell cultures under conditions that encourage cell-to-cell aggregation to form scaffold-free spheroids comprised of densely packed cells. As a result of such tight cell packing, MCTSs share some key characteristics with clinical tumours, such as layered cell populations in different states of growth and health, nutrient/pH/oxygen spatial gradients, and multidrug resistance in some cases.[137] In the scope of this study, MCTSs (as analysed using CLSM) served as a midpoint between the previous 2D monolayers and subsequent in vivo tests biodistribution to test the effects of nanoparticle hydrophobicity.

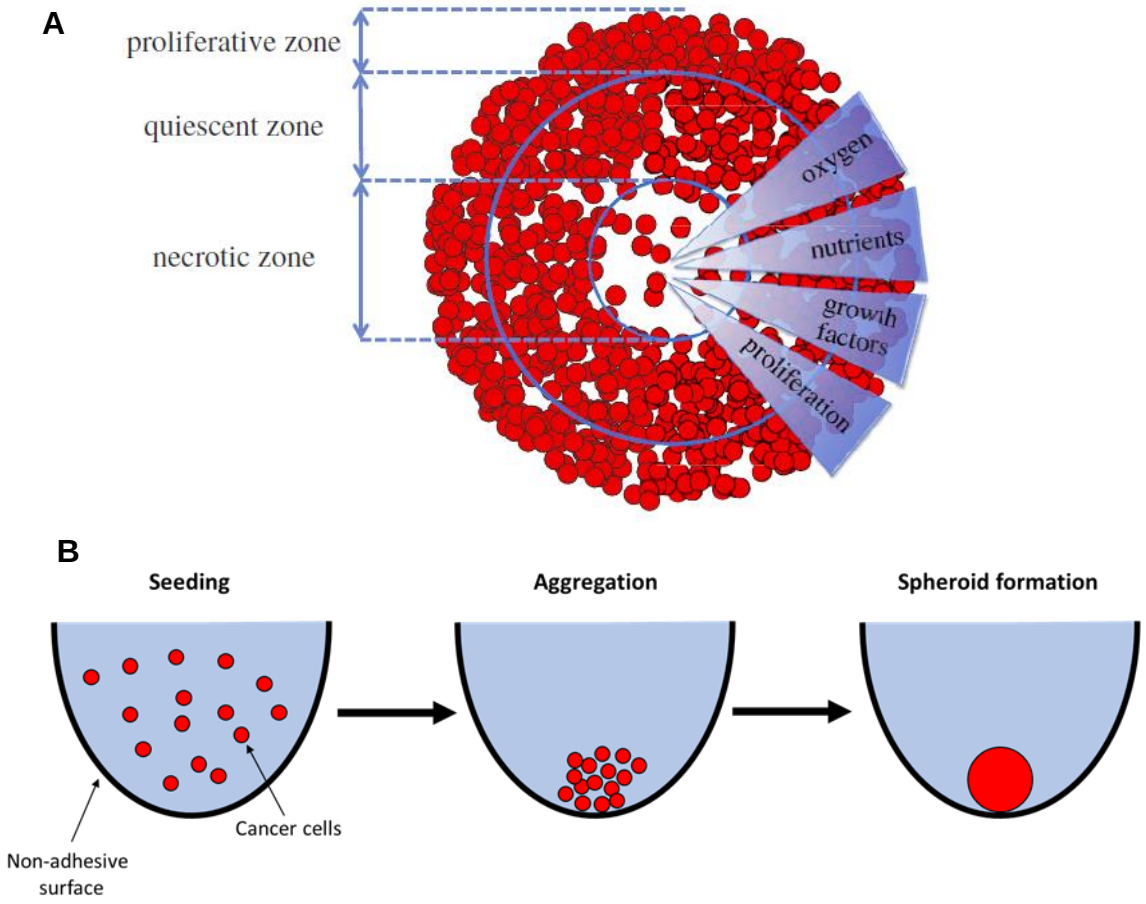

Figure 1.6. (A) Cross-sectional schematic of a representative MCTS, highlighting its spatial concentration gradients of oxygen, nutrients and growth factors, as well as its layered cell populations marked by differences in proliferation states. Adapted from Dini *et al.*[138] **(B)** The liquid overlay technique used in this work to produce MCTSs. The technique involves seeding cells onto a surface functionalised with a low-attachment substrate to eliminate cell-surface adhesion. This instead favours cell-cell aggregation that triggers spheroid formation.

While CLSM of in vitro cancer cell models is adequate to qualitatively assess the effect of MPB hydrophobicity on cellular association, an auxiliary method is necessary to quantitatively confirm the nanoparticle results shown by microscopy. Flow cytometry is one of several methods that can be used for that purpose and is advantageous for the high volume of data it generates in a short amount of time. The manner by which flow cytometry can evaluate nanoparticle associations with cells is achieved through a combination of light

scattering and fluorescence emission. Basic flow cytometer operation starts with a stream of sample cells focused via a carrier fluid so that they pass across a series of lasers in a single file, enabling individual cells to be analysed at a time. The light scattered by each cell in the forward (FSC) and side (SSC) directions relative to the incident laser is separately recorded by a series of detectors, which manifests as a signal 'peak' whose height and area provides information on cell size and granularity. While these parameters are not always directly tied to the total level of nanoparticle uptake by cells, they are important as overall indicators of cell health, which can therefore be used to potentially detect cytotoxic effects of nanoparticles on the tested cell population. More relevant to this work is the ability of typical flow cytometers to also detect fluorescent signals emanating from cells. As each MPB is tagged with an appropriate fluorescent label for previous in vitro/in vivo studies, suitable fluorescence detectors in the flow cytometer should be able to directly measure each MPBs fluorescence intensity originating from individual cells, and correlate this with their total uptake/association.

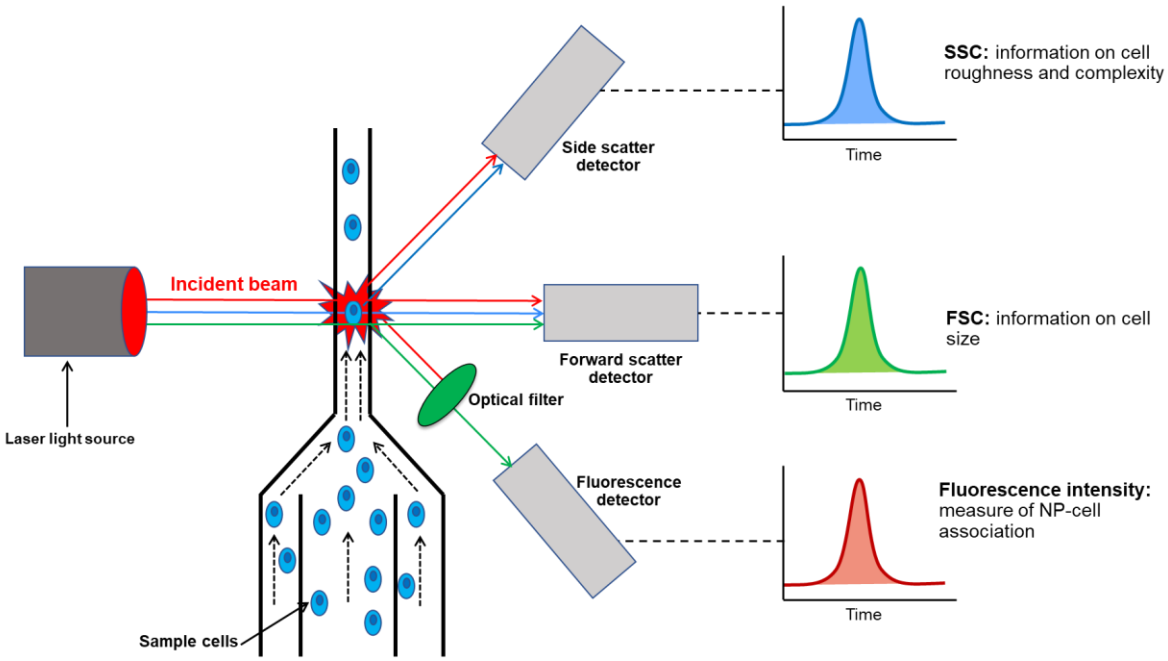

Figure 1.7. Typical set-up of a flow cytometer instrument highlighting basic principles of its' operation.

The third chapter marks a shift in our investigation's focus, from how nanoparticle hydrophobicity affects tumour passive-targeting and penetration to its effect on nanoparticles' interaction with serum proteins and cellular membranes. Using the same amphiphilic MPBs synthesised earlier, changes in their behaviour in the presence of biological components, such as serum proteins, will firstly be probed using dynamic light scattering (DLS). Gaining a deeper understanding of the PC beyond simple physicochemical changes to the nanoparticle-protein complex proves more challenging, however. The reason being most PC analytical techniques either characterise nanoparticle changes only before and after protein adsorption (such as via DLS or other chromatographic separation techniques), or only provide information on the final corona's composition. Conversely, uncovering the mechanisms behind protein adsorption at the nano-bio interface on a thermodynamic and molecular scale is a standard that can only be accomplished a limited number of techniques, such as isothermal titration calorimetry (ITC). By measuring heat changes from intermolecular binding between nanoparticles and other biomolecules, ITC has exhibited its usefulness in shedding light on the forces underlying PC formation.[139,140] Fundamentally, an ITC experiment is performed by multiple titrations of one molecular species (in this case, a single protein) into a sample cell containing a second analyte species (a nanoparticle). During the experiment, energy is either absorbed or released in the form of heat which originates from analyte binding events during each titration. As these binding events result in temperature changes to the sample cell, the system makes appropriate changes to the sample cell's heating rate in order to maintain its' constant temperature relative to a reference cell (i.e. to maintain isothermal

conditions). The requisite heating/cooling changes made over the experiments' duration can be subsequently plotted and integrated to yield a titration curve. From there on, an appropriately selected mathematical binding model can be used to fit the titration curve, which in turn can provide important thermodynamic parameters of the interactions, such as change in Gibbs free energy (ΔG), dissociation constants (K_D), stoichiometry of binding (n), change in enthalpy and entropy (ΔH and ΔS).

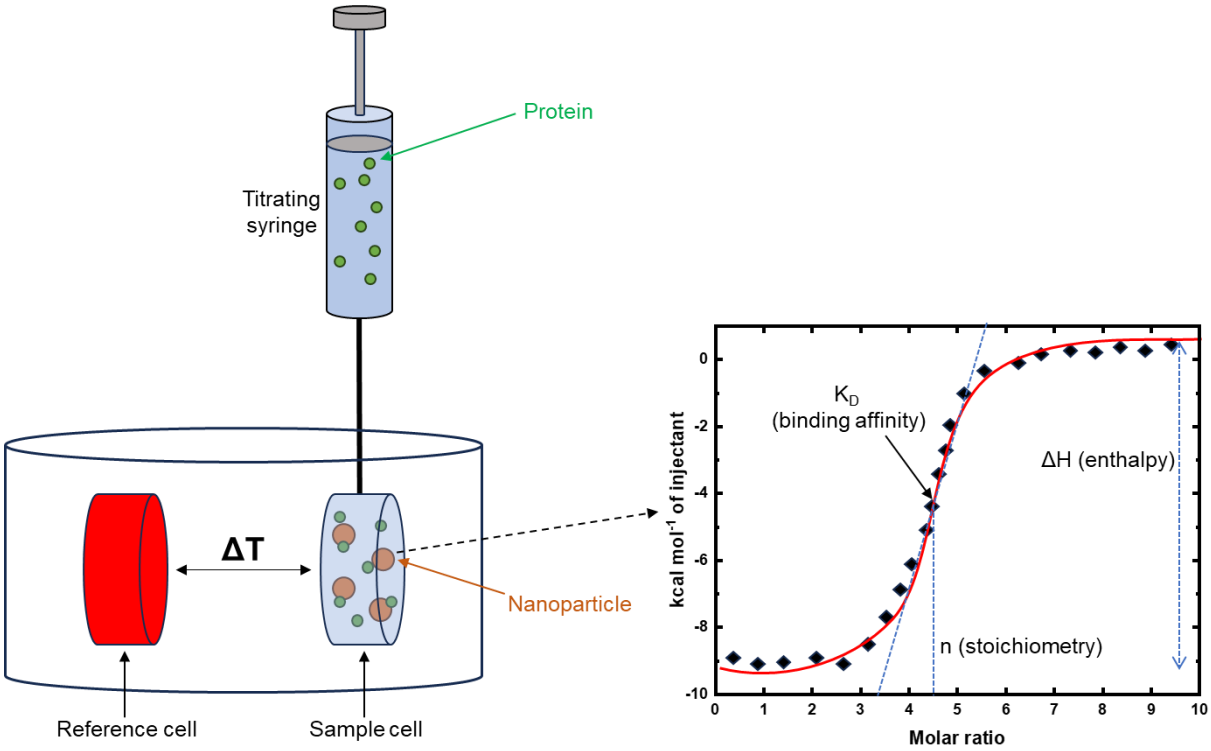

Figure 1.8. Typical set-up (left) of an ITC instrument and the extracted data (right panel) in the form of an adsorption isotherm, showcasing how various thermodynamic parameters are derived from binding events between the analytes of interest (in this context between nanoparticles and proteins).

From our preliminary investigations to how the hydrophobic-hydrophilic balance governs the MPBs' serum protein interactions, the next step will be to probe the influence of this parameter on their behaviour with model cell membranes. This is an especially important factor for any nanomaterial purposed for drug-delivery, as the cell membrane represents

an important frontier that must be successfully translocated for nanoparticles to deliver their payload. With the relevance of cellular membrane interactions in governing nanoparticles' biological behaviour being increasingly apparent, numerous biomimetic membrane models that can accurately replicate the fluidity and compositional complexity of natural cell membranes have been developed over time.[141,142] Most of these membrane models are additionally useful in that they are quite structurally robust and eliminate the need to raise and maintain biological cell cultures. One promising model in particular belonging to this group are tethered bilayer lipid membranes (tBLMs), which have been increasingly deployed to screen the membrane-disruptive activity of nanoparticles.[143–145] As shown in **Figure 1.9**, tBLMs essentially consist of a planar lipid bilayer self-assembled over a solid support/electrode (usually made of gold). Here, the planar membrane is suspended some distance over the solid surface via macromolecular tethering chains that are directly grafted to the solid gold substrate. Interspersed alongside these tether groups are shorter 'spacer' chains that helps to provide adequate submembrane space to form an aqueous ion reservoir. As the lipids are deposited atop the solid surface, the 'tether' groups serve as anchor points upon which the inner leaflet of the membrane is attached, followed by the upper leaflet to create the complete bilayer. The suspension of the membrane above the gold substrate via macromolecular linkers confers tBLMs with a few key advantages, such as enhanced structural stability in ambient conditions compared to alternate models such as black lipid membranes.[146,147] At the same time, tBLMs manage to retain sufficient fluidity that positions them closer in biophysical character to natural cellular membranes, as opposed to models like hybrid bilayer membranes (HBMs) where the membrane is formed in direct contact with a hydrophobic substrate, making it unsuitably rigid in studies examining transmembrane ion flux and incorporation of transmembrane proteins.[148,149] The most vital feature of tBLMs in this study however is the presence of a substantial

submembrane space between the solid substrate and the bottom leaflet, which can serve as an ion reservoir and enables sufficient transmembrane ion flux. As a natural outcome of the presence of ion reservoirs on both sides of the membrane, tBLMs offer the possibility of using appropriate electrochemical analysis techniques to characterise current flow (as generated by ion flux) across the membrane. Due to the excellent electrical sealing properties of the membrane combined both ion reservoirs, techniques such as electrochemical impedance spectroscopy (EIS) can be used to assess certain physical properties of the model membranes.

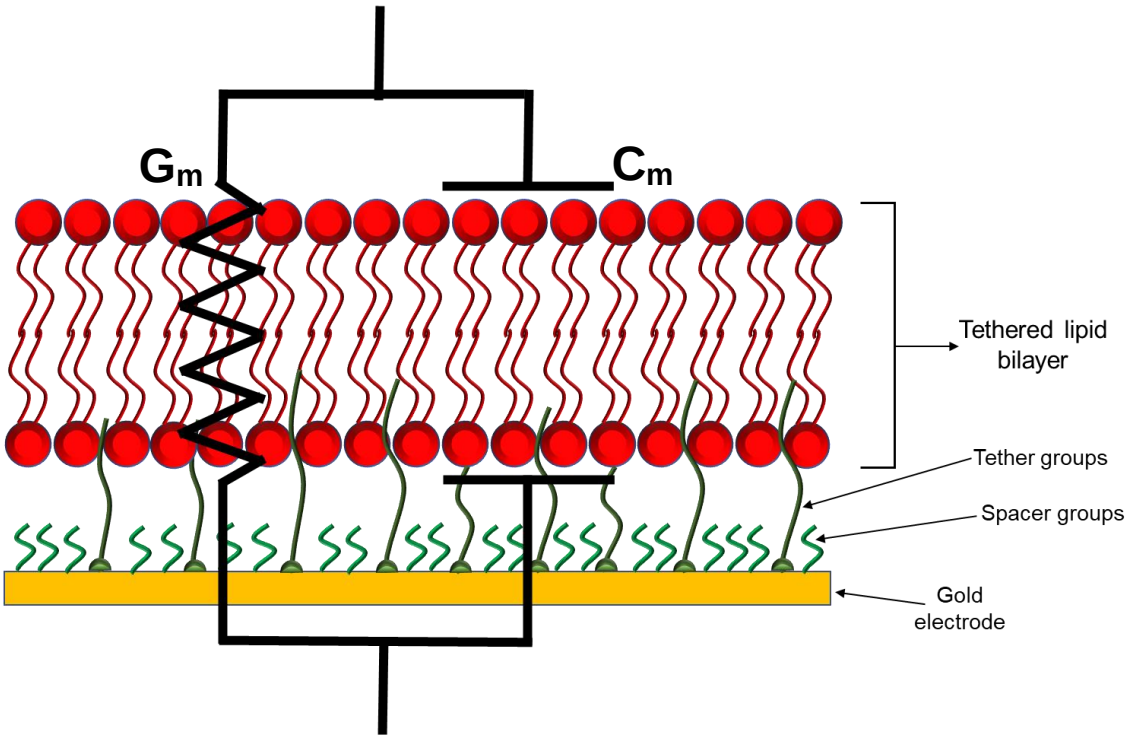

Figure 1.9. Schematic representation of a tBLM**,** highlighting the sub-membrane space between the bottom leaflet and the solid substrate. Since tBLMs allow for sufficient ion translocation across the membrane, the electrical properties and by extension, the physical stability of the membrane can be monitored through measurement of the membrane's capacitance (C_m) and conductance (G_m).

CHAPTER II

The Hydrophilic-Hydrophobic Balance of Molecular Polymer Brushes Dictates their Biodistribution and In Vivo Interactions with Cancer Cells and Tumours

2.1. Abstract

This research chapter sought to elucidate the effect of nanoparticle hydrophobicity/hydrophilicity on its efficiency in tumour penetration, biodistribution patterns, and passive tumour homing and accumulation, using MPBs as the nanoparticle template. Here, a series of MPBs with varying levels of hydrophobic-hydrophilic balance was constructed by adjusting the ratio of hydrophilic poly(ethylene glycol) methyl ether methacrylate (PEGMA) to the more hydrophobic di(ethylene glycol) methyl ether methacrylate (DEGMA). In vitro data gained from incubating the MPBs with 2D cell monolayers and 3D multicellular tumour spheroids (MCTS) showed marginal effects of hydrophobicity/hydrophilicity. However, the effects of adjusting this parameter were more pronounced upon MPB injection in tumour-bearing mice, wherein the more hydrophobic MPBs experienced greater deposition and retention within tumours.

2.2. Introduction

The potential of nanoparticles in massively improving the targeted delivery of therapeutics to tumours has been long documented in the past few decades and has amounted to a vast number of reported designs for this special purpose.[4,150] Even so, there are various systemic barriers confronting a nanosized drug delivery upon initial administration, which shortens their lifetime in the bloodstream and considerably reduces the dose fraction reaching the tumour target. To add to these complications, the remodelled microenvironment of the tumour creates added obstacles for nanoparticle tumour internalisation itself, further lowering the quantity able to apply a therapeutic effect.[151] Spurned by the sub-optimal performances of most nanoparticles against tumours in the clinic, research focus has turned towards determining the roles that a nanoparticle's physicochemical properties play in their tumour-targeting efficiency.[152] Up to now, general frameworks have been laid down to design nanoparticles with specifically engineered sizes, shapes/architectures and surface chemistries/charges that will ideally be able to surmount the various barriers in circulation and improve their internalisation into the tumour itself.[153,154] Even so, one physicochemical factor that has remained scarcely examined for its potential role in governing the anti-tumour efficiency of nanoparticles is their amphiphilicity, or hydrophilic-hydrophobic balance. Ferri *et al.* explored a possible relationship between nanoparticle surface hydrophobicity and uptake into cancer cells.[155] Their platform employed silver nanoparticles capped with P(MeO_2MA-c-OEGMA) copolymers of different monomer ratios, affording them particles with changeable hydrophobicity. Their findings demonstrated enhanced cellular uptake of the more hydrophobic formulations in L-929 fibroblasts, which was dependent to an extent on the presence of serum proteins. A similar structure-activity relationship study between nanoparticle hydrophobicity and their biological effects was reported by Moyano *et al.*[156] Their approach to modulating

nanoparticle surface hydrophobicity was however realised using a series of gold nanoparticles, appended with polymers bearing zwitterionic sulfobetaine terminal groups. These sulfobetaine moieties were modified with different substituents at the quaternary ammonium nitrogen, yielding variable hydrophobic levels in the final nanoparticles. Against MCF-7 cultures the gold particles all showed improved cellular uptake cancer cells when hydrophobicity was increased, and showed effective resistance to protein fouling in physiologically relevant serum conditions. To date however, few studies have holistically investigated how nanoparticle biodistribution, tumour-homing and tumour cell association change on the basis of their hydrophobicity in complex in vivo environments.[157] A methodical investigation in that direction would be especially valuable in unveiling how nanoparticles with different hydrophobicities perform as tumour-targeting agents within a more physiologically relevant model of a complete organism, where factors such as blood circulation, immunogenicity and renal clearance mechanisms need to be considered.

In this work, we demonstrate the capabilities of MPBs as a nanoparticle platform for a structure-activity study between nanoparticle hydrophobicity and their efficiency in tumour penetration, as well as tumour-homing/accumulation in vivo. The appeal of MPBs in studies such as this is driven by their ability to act as unimolecular particles with nanoscale dimensions,[158] whose physicochemical properties can be orthogonally tailored.[159] Herein, we exploit this versatility to synthesise MPBs with systematically varied hydrophilic-hydrophobic balances whilst leaving all other physical determinants ostensibly identical. To achieve these varied hydrophobicity levels, the MPBs' sidechains were polymerised as a random copolymer consisting of systematically controlled ratios of a hydrophilic and hydrophobic monomer: poly(ethylene glycol) methyl ether methacrylate (PEGMA, Mn = 300 g mol^{-1}) and di(ethylene glycol) methyl ether methacrylate

(DEGMA). Both monomers are derivatives of oligo(ethylene glycol) methyl ether methacrylate (OEGMA), consisting of a set number of ethylene glycol (EG) units appended to a methacrylate backbone. To date, several studies have explored the potential of P(OEGMA)-based nanoparticles for biomedical applications,[132,160] and a few investigations have hinted towards their applicability as tumour-targeting theranostics,[161,162] due to their excellent water solubility and biocompatibility,[163] greater efficiency in tumour uptake compared to PEG,[164] and its absence of a antigenic response compared to PEG.[165–168] Within the bounds of this work however, the most interesting and attractive feature of PEGMA and DEGMA is their differing hydrophobicity, which originates from the higher number of EG units in PEGMA (4-5) compared to DEGMA (2).[169,170] As such, incorporation of both of these monomers with broadly similar chemical structures allows us to precisely tune the hydrophilic-hydrophobic balance of the final MPBs. In elucidating how biodistribution, passive tumour-homing and tumour retention of the MPBs is affected by their amphiphilicity, 2D and 3D in vitro models were used in the form of monolayers and MCTSs, followed by a more thorough investigation using mouse tumour xenograft models to analyse the particles behaviour in vivo.

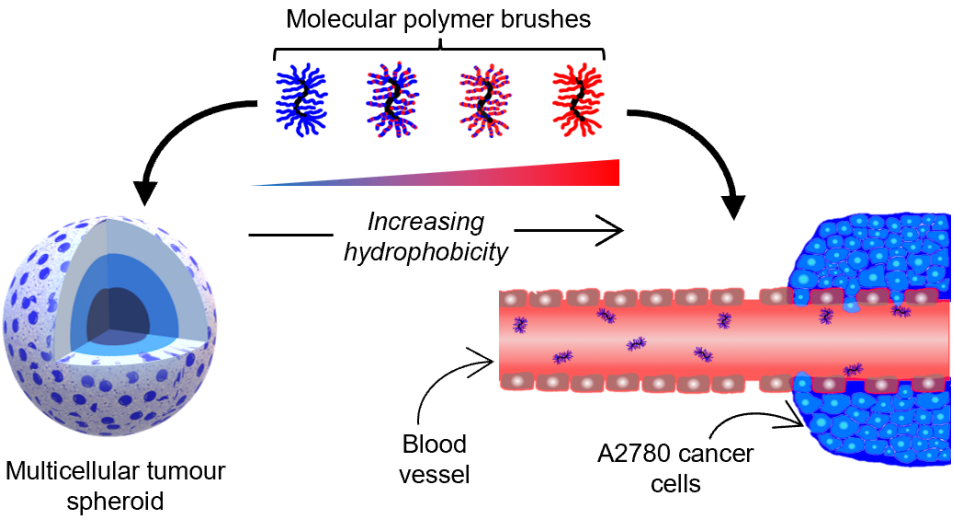

Figure 2.1. Overview of the approach adopted in this research chapter to studying the effects of nanoparticle hydrophobicity on their tumour accumulation and homing behaviour. A series of MPBs bearing different hydrophobicities were used as the test nanoparticle platform, and were successively tested against both in vitro and in vivo tumour models in the form of MCTSs and mouse tumour xenograft models respectively.

2.3. Experimental Section

2.3.1. Materials

Di(ethylene glycol) methyl ether methacrylate (DEGMA, 95%), poly(ethylene glycol) methyl ether methacrylate (PEGMA, 95%, Mn = 300 g mol^{-1}), glycidyl methacrylate (GMA, 95%), 2-hydroxyethyl methacrylate (HEMA, 95%), 4-cyano-4-(thiobenzoylthio)pentanoic acid (CTBPA, 98%), α-bromoisobutyryl bromide (α-BiBB, 98%), 1,1,4,7,10,10-hexamethyltriethylenetetramine (HMTETA, 97%), ATTO633-alkyne (in DMSO, 1 mg mL^{-1}), Cy5-alkyne (95%, in DMSO, 1 mg mL^{-1}) and phosphate buffer saline (PBS) tablets were purchased from Sigma Aldrich (Australia). 4,’’-azobis(4-cyanovaleric acid) (V501,pure solid, Alfa Aesar), copper(I) chloride (CuCl, ACS grade, Merck), ammonium chloride (NH4Cl, pure solid, Merck), sodium azide (NaN3, pure solid, Ajax), copper(II) sulfate pentahydrate (CuSO4.5H2O, pure solid, Ajax), anisole (≥ 99 %,

Merck), N,N'- dimethylformamide (DMF, ≥ 99 %, JAX) and ethanol (≥ 99 %, Merck) were obtained as stated and used as received. PEGMA, DEGMA, GMA and HEMA were passed through a short silica column to remove polymerisation inhibitors before use. CuCl was purified by washing with glacial acetic acid, diethyl ether and ethanol. Dulbecco's Modified Eagle's Medium (DMEM, with and without phenol red), Dulbecco's phosphate buffered saline (DPBS, no added calcium or magnesium), L-glutamine (200 mM, cell culture supplement), antibiotic-antimycotic solution (100x, containing penicillin and streptomycin), foetal bovine serum (FBS, heat-inactivated) and trypsin-EDTA (0.5%, no phenol red) were purchased from Thermo Fisher Scientific Ltd. RPMI 1640 cell culture media containing L-glutamine was sourced from Corning. DLD-1 and A549 cancer cell lines were sourced from the New research group (School of Chemistry, University of Sydney). A2780 ovarian cancer cells were purchased from ATCC. Female NCR nu/nu mice were purchased from In-House Breeding Colony of UCSD. High concentration Matrigel Membrane Matrix was sourced from Corning.

2.3.2. Characterisation Methods

Proton Nuclear Magnetic Resonance (^{1}H NMR): Analyses were carried out on a Bruker Avance 300 spectrometer set at 300 mHz and 300 K. Samples were prepared in deuterated chloroform (CDCl3) or deuterated methanol (MeOD).

Size-exclusion chromatography (SEC): SEC analyses were performed using a UFLC Shimadzu Prominence SEC system equipped with Phenogel^{TM} columns (5 µm, 10^4 Å and 10^5 Å). Dimethylacetamide (DMAc) containing butylhydroxytoluene (BHT, 0.05 % w/w) and LiBr (0.03 % w/w) was used as the eluent set to a flow rate of 1 mL min^{-1} at 50 °C. SEC samples were prepared by dissolution of material in DMAc and passing through a

0.22 µm nylon filter before analysis. Apparent molecular weights were derive from a calibration curve generated by a series of monodisperse poly(methyl methacrylate (PMMA) samples.

Fluorescence spectroscopy: Measurements were performed on an Agilent Technologies Cary Eclipse Fluorescence Spectrophotometer. An excitation and emission slit size of 5 nm was used with an excitation wavelength of 630 nm and 650 nm for ATTO633- and Cy5-labelled MPB solutions respectively. All samples were analysed at a prepared concentration of 0.2 mg mL^{-1} in a quartz microcuvette.

Infrared (IR) spectroscopy: Measurements were carried out on a Perkin Elmer Spectrum Two FTIR spectrometer using samples dried from acetone.

Dynamic light scattering (DLS): Analyses of the MPBs' Z-average hydrodynamic diameters (D_H) and cloud point temperatures (T_{CP}) were performed on a Malvern Zetasizer Nano ZS equipped with a He-Ne 633 nm laser. Light scattering data was collected at a 173° detector angle after an equilibration time of 180 s. Solutions were prepared for analysis by dissolving material in PBS x1 to a final concentration of 0.5 mg mL^{-1}. For T_{CP} measurements of brushes, the D_H was measured at increasing temperatures starting from 25 °C up to 70 °C, in 5 °C increments.

Statistical analysis: Statistical tests were performed using GraphPad Prism v8.0 (GraphPad Software) and Origin 8. Data are presented as means ± SEM. One-way analysis of variance (ANOVA) with Tukey's multiple comparison tests were used compare different groups and determine statistical significance (* $p < 0.05$, ** $p < 0.01$, *** $p < 0.001$, **** $p < 0.0001$).

2.3.3. Synthetic Methods

Synthesis of PHEMA backbone: HEMA (460 mg, 3.6 mmol), CTBPA (10 mg, 0.036 mmol) and V_{501} (2.5 mg, 9.0 mmol) were dissolved in DMF (1.5 mL) before undergoing three cycles of freeze-pump-thaw. The mixture was polymerized at 70 °C for 6 h before quenching *via* cooling and opening to air. The final product was purified by precipitating in diethyl ether and dissolving in DMF twice. Afterwards, the polymer was dissolved in a 2:1 mixture of dioxane and water before it was freeze-dried. Monomer conversion was calculated from ^{1}H NMR spectroscopy based on the relative reduction of the vinyl proton signals (ca. 5.5 – 6.5 ppm) from the reaction mixture before and after polymerization.

Synthesis of PBIEM: PHEMA (170 mg, 1.26 mmol equiv. of hydroxyl groups) was dissolved in anhydrous pyridine (10 mL, dried over molecular sieves overnight) over ice. α-BiBB (870 mg, 4.8 mmol) was added dropwise to the solution, after which the solution was stirred overnight at room temperature. For purification, the polymer was precipitated into MilliQ water, redissolved in THF and precipitated again into MilliQ water. The polymer was subsequently dissolved in dioxane for freeze-drying.

Sidechain grafting from PBIEM: In a typical procedure used to make the four MPBs used in this study, PBIEM (5 mg, 0.018 mmol equiv. of Br), GMA (25 mg, 0.18 mmol) HMTETA (9.6 µL, 0.018 mmol), and varying amounts of PEGMA and DEGMA were dissolved in anisole (5 mL). The mixture was degassed by three cycles of freeze-pump-thaw. Before the third freeze cycle, copper(I) chloride (1.8 mg, 0.018 mmol) was added to the mixture and the cycle was continued. The mixture was reacted at 65 °C for 18 h before quenching *via* cooling and exposure to air. Copper was removed by passing the mixture through a silica column. The product was partly purified by two cycles of precipitation and redissolving in cold hexane and anisole respectively. Lastly, the polymer brushes were

dissolved in acetone and dialyzed (MWCO = 14 kDa) into acetone for storage. The DP of the sidechains was calculated from conversion as measured by ^{1}H NMR, based on the relative reduction of the vinyl proton signals (ca. 5.5 – 6.5 ppm) in reaction feedstock samples before and after polymerization.

For the syntheses of the remaining brushes, the protocol was followed with no changes except for the molar percentage of PEGMA and DEGMA fed into the reactions, which are detailed in Table 1. The MPBs were denoted according to the molar percentage of the more hydrophobic DEGMA in their sidechains, ranging from the most hydrophilic D0% (0 DEGMA, 95% PEGMA300, 5% GMA), D20% (20% DEGMA, 75% PEGMA300, 5% GMA), D40% (40% DEGMA, 55% PEGMA300, 5% GMA) and finally the most hydrophobic member D60% (60% DEGMA, 35% PEGMA, 5% GMA).

Table 2.1. Reaction parameters for the four MPBs detailing the specific amounts of monomers used in the initial reaction feedstocks.

MPB	**Reaction feedstock quantities**					
	PEGMA		**DEGMA**		**GMA**	
	mole (mmol)	**mass (mg)**	**mole (mmol)**	**mass (mg)**	**mole (mmol)**	**mass (mg)**
D0%	3.34	1001	0	0	0.18	25
D20%	2.63	790	0.70	132	0.18	25
D40%	1.93	580	1.40	264	0.18	25
D60%	1.23	369	2.11	397	0.18	25

Fluorophore labelling of MPBs: PBIEM-*g*-P(PEGMA-*co*-DEGMA-*co*-GMA) (40 mg, 1.4 x 10^{-6} mmol equiv. of GMA), sodium azide (10 mg, 0.15 mmol) and ammonium chloride (10 mg, 0.15 mmol) were dissolved in DMF (3 mL) and stirred overnight at 50 °C. The polymer brushes were then dialyzed once into a 1:1 acetone and methanol mixture,

before being dialyzed again into neat acetone (MWCO = 3 kDa). PBIEM-*g*-P(PEGMA-*co*-DEGMA-*co*-GMA) (35 mg, 7.9 x 10^{-6} mmol), ATTO633 alkyne / Cy5 alkyne (20 µL, 1 mg mL^{-1} in DMSO), ascorbic acid (10 mg, 0.057 mmol) and $CuSO_4 \bullet 5H_2O$ (10 mg, 0.04 mmol) was dissolved in a mixture of water (2 mL) and methanol (1 mL). The solution was stirred in darkness at room temperature overnight. The mixture was dialyzed twice into acetone, then once into Milli-Q water (MWCO = 4 kDa). The polymer brushes were subsequently stored in darkness to avoid photo-bleaching.

2.3.4. In Vitro and In Vivo Experimental Methods

Monolayer and multicellular tumour spheroids (MCTS) culturing/uptake assay: DLD-1 and A549 cancer cell lines were grown in complete Dulbecco's Modified Eagle Medium (DMEM) supplemented with 10 % (v/v) foetal bovine serum (FBS), 1 % (v/v) penicillin/streptomycin and 1 % *L*-glutamine at 37 °C and 5 % CO_2. Cells were sub-cultured at regular 3-day intervals with trypsin-EDTA.

DLD-1 and A549 monolayers were cultured by pipetting 5 x 10^4 cells each into 35 mm µ-dishes (purchased from DKSH Holding AG) and incubating at 37 °C and 5 % CO_2 in complete DMEM supplemented with 2 % (v/v) FBS for 144 h. Afterwards, old growth media was carefully removed, washed with DPBS and replaced with DMEM-FBS solutions containing the MPBs (0.2 mg mL^{-1}, 2 mL total) and left to incubate for another 24 h. The samples were prepared for microscopic analysis by carefully draining the MPB-containing growth media, washing the monolayers twice with PBSx1, and adding 2 mL of DMEM (10 % (v/v) FBS, no phenol red).

DLD-1 MCTSs were formed by pipetting 10^4 cells each in Corning Costar Ultra-Low Attachment 96-well plate (n = 4 wells per sample) and incubating for 72 h. For the uptake assay, MCTSs had their old media removed and replaced with DMEM-FBS solutions containing the MPBs (0.5 mg mL^{-1}, 200 µL per well) and left to incubate for another 24 h. After dosing and incubation, the spheroids had their old media carefully removed and were washed with DPBS twice to remove any unbound MPBs. Each spheroid was then transferred to 35 mm µ-dishes containing DPBS (1 mL) for imaging.

Flo**w **cytometry: A549 cells were seeded at a density of 2.5 x 10^4 cells in 12-well plates and cultured for 24 h. Afterwards, old media was removed and the cells were washed with PBS (100 µL) per well before fresh media containing the MPBs (c = 0.2 mg mL^{-1}) was added. The cells were subsequently incubated at 37 °C for 24 h, after which they were washed with PBSx1 (2 x 100 µL) and detached from the surface by addition of trypsin-EDTA (200 µL) and incubation for 3 min. Fresh media (400 µL) subsequently added to the cell suspension to neutralise residual trypsin, after which the cells were centrifuged for 5 min at 300 *x g*. The cell pellet was subsequently resuspended in cold FACS buffer (Dulbecco's PBS supplemented with 2.5 % v/v of FBS, 5 mM EDTA and 0.01 % v/v of sodium azide) until they were used.

A549 cell samples were measured using a BD LSRII flow cytometer. Mean fluorescence intensities (MFI) of treated cells were derived from a population of at least 10,000 cells (n = 3 per sample).

Cell culture and tumour inoculation: A2780 ovarian tumour cells (ATCC) were cultured in RPMI media (Corning) with 10% (v/v) foetal bovine serum (FBS) (R&D Systems) and 1% (v/v) penicillin-streptomycin (ThermoFisher Scientific) and maintained at 37 °C with 5% CO_2.

All mice studies were approved by the Institutional Animal Care and Use Committee (IACUC) of the University of California, San Diego (UCSD). 6-8 weeks old female NCR nu/nu mice were purchased from the In-House Breeding Colony of UCSD. Only female mice were considered because ovarian tumours were chosen as a mouse model. All mice were placed on Teklad 10 protein rodent diet (Envigo) for at least 10 days prior to any imaging procedures to minimize autofluorescence. 2 x 10^6 A2780 cells were suspended in 100 µL of culture media and Matrigel (Corning) at a 1:1 ratio and subcutaneously injected into the right flank of each mouse for tumour inoculation. All tumours were established and monitored closely till 11 days post-inoculation, when all tumours reached 200-300 mm^3 in volume using the formula $v = l \times \frac{w^2}{2}$.

Biodistribution of injected MPBs: On day 11 post tumour inoculation, when tumours reached 200-300 mm^3, 500 µg Cy5-labelled MPBs (D0%, D20%, D40% and D60%) in 125 µL PBS were intravenously injected with n=4 mice per group and one PBS control group. Two studies were conducted: a 24 h study, where all mice were imaged at 9 h and 24 h post administration of the MPBs or PBS using an IVIS 200 system (Xenogen); then mice were sacrificed, and organs and tumours collected for further analysis.

A 48-h study was carried out, where mice were imaged at 9 h, 24 h and 48 h post administration of the MPBs or PBS; then mice were sacrificed, and organs and tumours collected for further analysis. Organs (brain, heart, lung, spleen, kidney, and liver) and tumours were collected and imaged using the same setting for whole animal imaging. All images were processed analysed using the Living Image v2.5 software (Xenogen), and Cy5 fluorescence intensity of each organ was quantified. As a secondary method for quantification of the fluorescence signals from the brushes, tissues were weighed and homogenized within 1 mL PBS using a Cole-Parmer LabGEN 125 homogenizer.

Homogenized samples were centrifuged at 8000 g for 5 min, and the tissue supernatant were collected to measure the Cy5 fluorescence using a Tecan Infinite M200 plate reader (excitation: 633 nm; emission: 665 nm; gain: 150); this experiment was done with n=2 samples from each experimental group. Amounts of brushes per tissue were calculated based on a standard curve using brushes of known concentration.

2.4. Results and Discussion

As part of this work, controlled radical polymerisation (CRP) techniques were used to prepare four biocompatible, oligo(ethylene glycol)-based bottlebrush polymers with varying amphiphilicity levels. In the first step of the MPBs' synthesis, reversible addition fragmentation chain transfer (RAFT) polymerisation was used to create a PHEMA precursor backbone with a degree of polymerisation (DP) of 50. By leveraging the pendant hydroxy groups situated along the backbone in an esterification reaction with α-BiBB, PHEMA was subsequently converted to PBIEM (**Scheme 2.1**). Analysis with ^{1}H-NMR before and after esterification verified the reaction's success as evidenced by the significant downfield shift of the ethylene peaks (peaks c and d, **Figure 2.2**), as well as the introduction of a new proton signal corresponding to the two newly introduced methyl groups of α-BiBB (**Figure 2.2**, peak e). SEC analysis presented a narrowly distributed population of the polymer backbones before and after functionalisation with dispersities of 1.17 and 1.32 for PHEMA and PBIEM respectively (**Figure 2.3**). It is also important to note the deviant behaviour exhibited by the backbones in the SEC matrix, manifesting as a shift of the converted backbone to a higher retention time despite the increase in molecular weight from the esterification. This discrepancy can be explained in terms of the polymers' changing polarity and therefore altered interactions with the SEC eluent. As

the polar PHEMA is converted to the less polar PBIEM, the hydrophobic effect triggers the slight intramolecular collapse and reduction in hydrodynamic volume of the polymer chains in the polar DMAc SEC mobile phase.

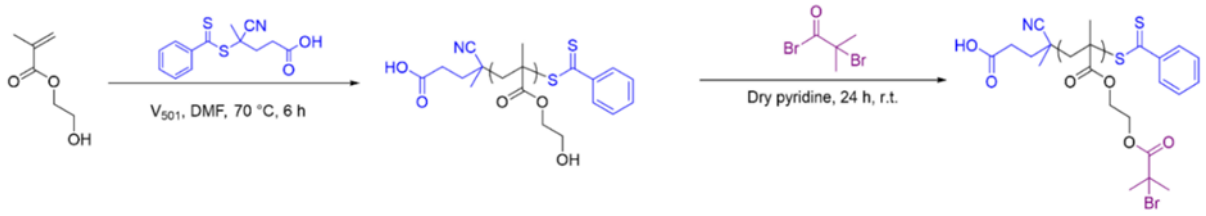

Scheme 2.1. Synthetic strategy used to prepare the PBIEM polyinitiator backbone from HEMA.

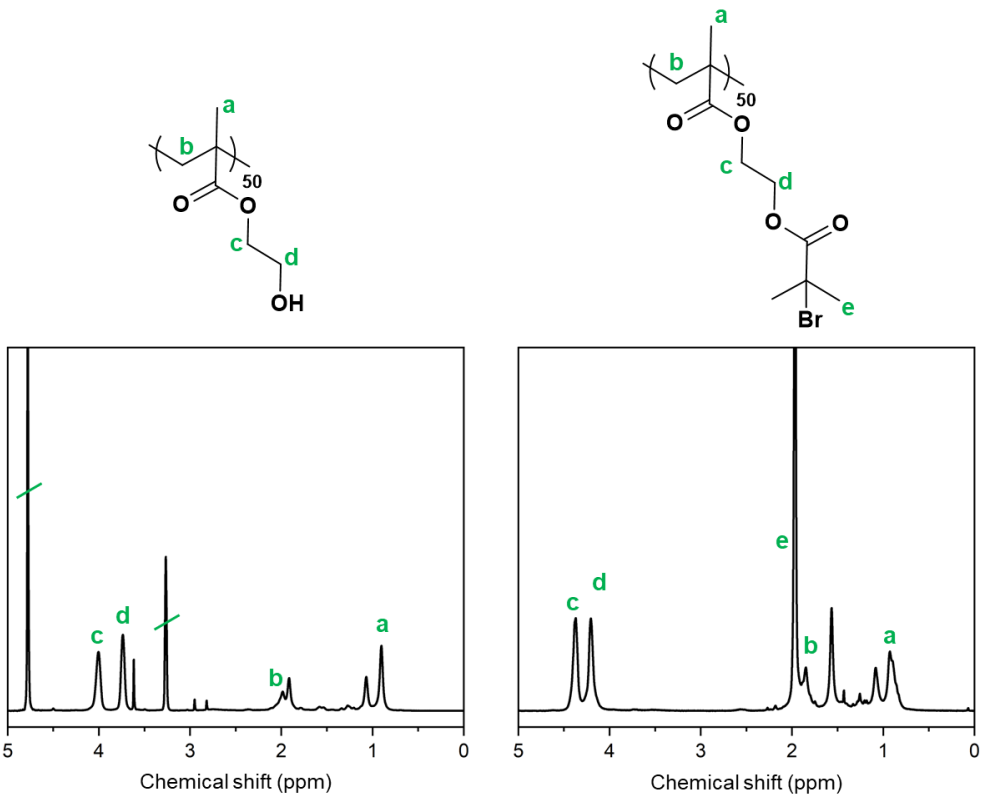

Figure 2.2. ^{1}H-NMR spectra of the **(A)** PHEMA backbone in MeOD and **(B)** PBIEM backbone in $CDCl_3$.

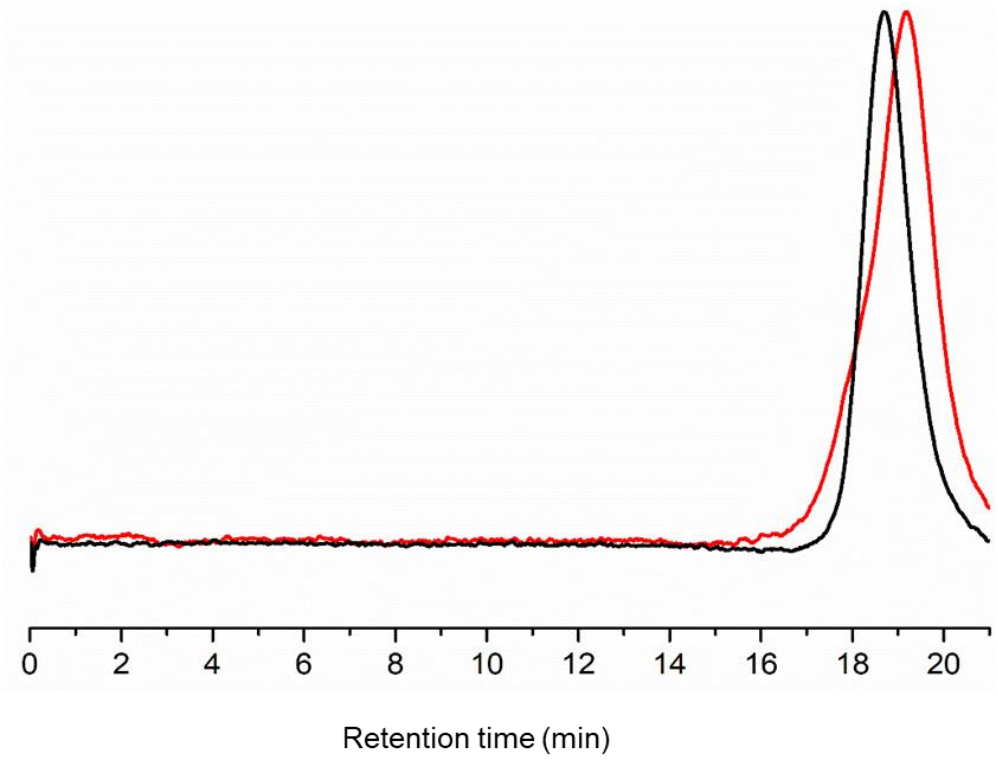

Figure 2.3. SEC chromatograms of PHEMA (black trace) and PBIEM (red trace) in DMAc.

The new PBIEM backbone, by virtue of its terminal bromide moieties, was subsequently used as a polyinitiator for the co-polymerisation of PEGMA, DEGMA and GMA via atom transfer radical polymerisation (ATRP) using the "grafting-from" approach. In this case, the ratio of the hydrophilic PEGMA to the relatively more hydrophobic DEGMA was methodically tuned in the ATRP reaction feedstock, affording a library of four bottlebrush polymer nanoparticles bearing different amphiphilicity levels. GMA was also copolymerised at a constant level of 5 mol% across all MPBs to provide a functional handle for future fluorophore attachment.

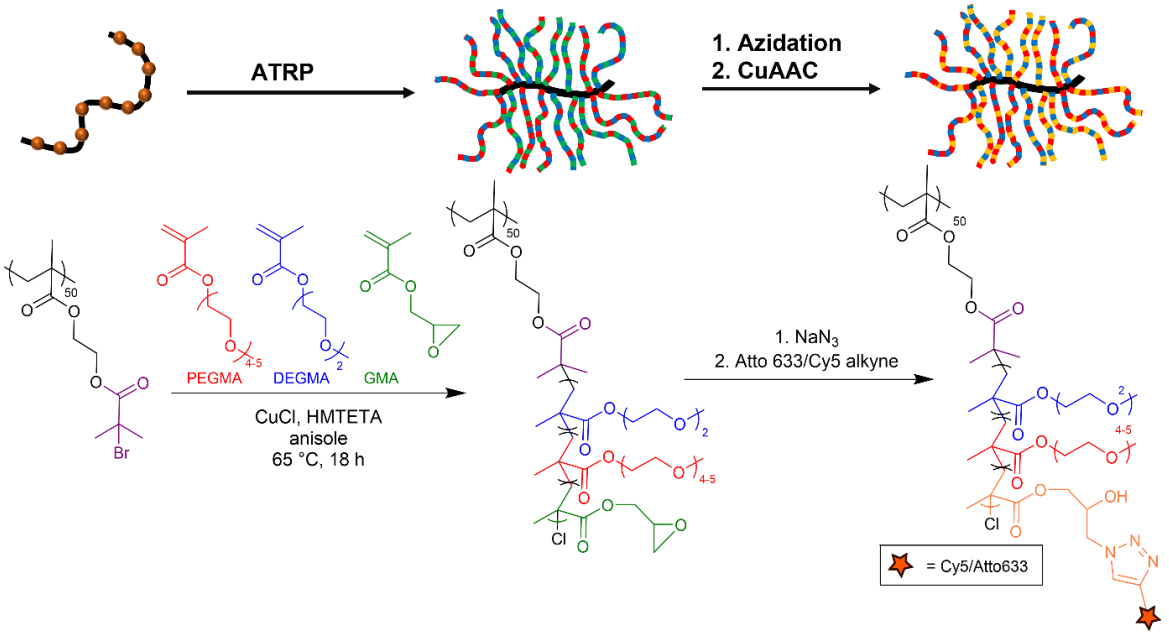

Figure 2.4. The polymerisation and post-modification strategy used to produce the four amphiphilic MPBs from a PBIEM backbone.

As with the precursor backbone, chemical characterisation of the brush series was carried out using ^{1}H-NMR to confirm the successful grafting of sidechains. Precise quantification via ^{1}H NMR spectroscopy of the DEGMA to PEGMA groups in the final products was difficult owing to the similar oxyethylene chemical environments in both monomers, and thus the corresponding signals from each were too overlapped to be reliably resolved. Ultimately, final sidechain composition was derived directly from the PEGMA:DEGMA ratio used for each MPBs' reaction feedstock. The similar reactivities and thus conversion rates of both PEGMA and DEGMA have been demonstrated in previous copolymerisation studies, so the final MPB sidechain composition could be extrapolated with confidence.[170,171] As the DP of the sidechains (140 on average) far surpassed that of the backbone (DP = 50), signals originating from the backbone could no longer be discerned in the brushes spectra (**Figure 2.5**). Nonetheless, the presence of GMA was satisfactorily confirmed by the weak signals at 2.6 – 2.9 ppm. Further evidence of the successful grafting

of sidechain monomers was seen in the SEC chromatograms of the final products (**Figure 2.6**, B). A shift of the pertinent peaks to much lower retention times compared to the starting backbone material (12-13 min and 19-20 min for the MPBs and backbones respectively) strongly indicated an increase in molar mass that could only stem from MPB formation. Shoulders appeared in the SEC chromatograms of D40% and D60%, revealing the presence of minor intercoupled brush-brush aggregates, but the occurrence of all the MPBs' peaks at similar retention times strongly evidenced their similar hydrodynamic volumes.

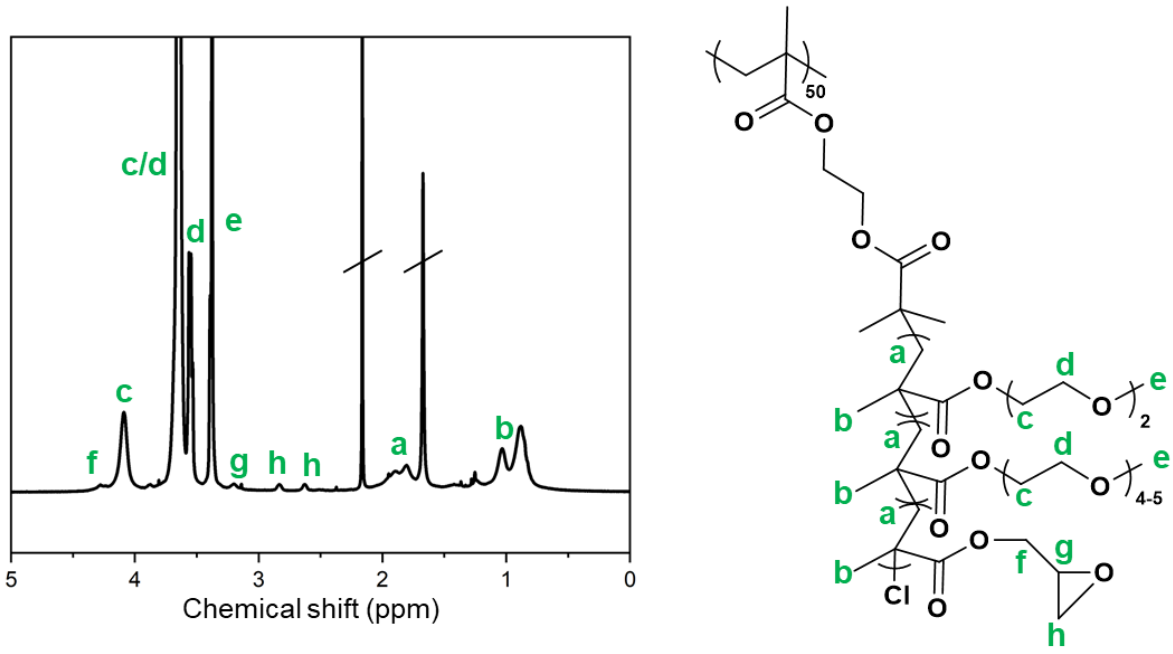

Figure 2.5. Representative ^{1}H NMR spectrum obtained in $CDCl_3$ of an amphiphilic MPB used in this study. Adapted from Ramamurthi *et al.*[172]

This was further corroborated with DLS analysis of the brushes in PBS, indicating dominant particle populations with comparable hydrodynamic diameters (**Figure 2.6**, A). The obtained D_H values for each MPB included: 40 nm (D0%), 46 nm (D20%), 41 nm

(D40%) and 40 nm (D60%). Although minor aggregation was apparent in the size distributions of D20%, D40% and D60%, it is important to consider the principles of Rayleigh/Mie scattering that underlie DLS measurements, which posit that the intensity of scattered light by colloidal particles is not only proportional to particle number but also their size. In this case, an increase in particle size by an order of magnitude will lead to a disproportionate 10^6 increase in scattered light. Hence, the signal from even a minimal number of large particles can overshadow that stemming from a larger population of smaller particles by comparison. Taking this into consideration, it is possible to disregard the large aggregates in the three MPBs populations, as the aggregates' intensity is low enough compared to the main intensity-weighted population to suggest that they exist in insignificant numbers.

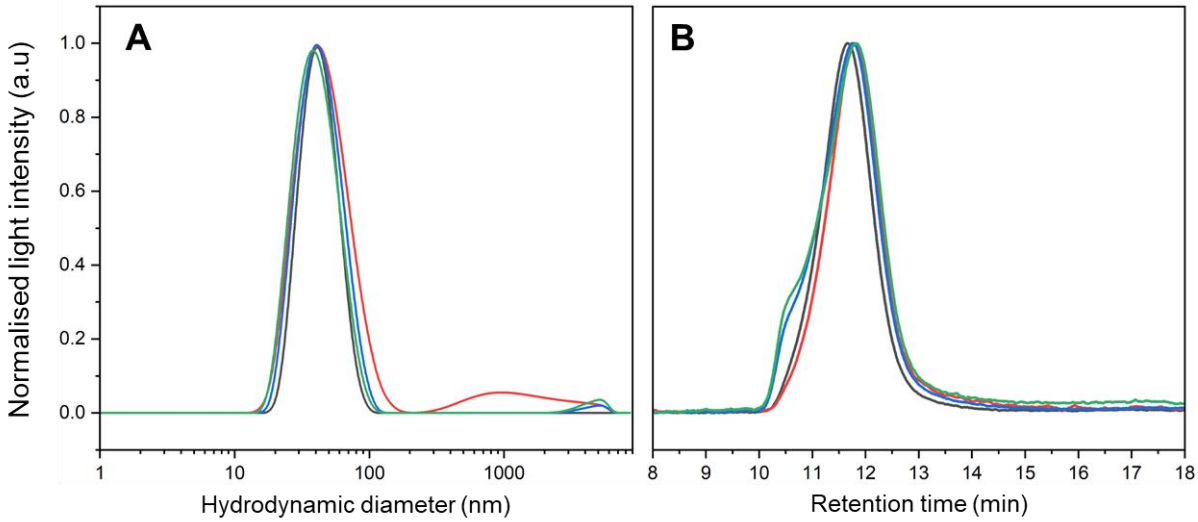

Figure 2.6. (A) Intensity-weighted hydrodynamic diameter distributions of the four MPBs in PBSx1 and **(B)** their SEC chromatograms obtained in DMAc; D0% (black), D20% (red), D40% (blue) and D60% (green). Adapted from Ramamurthi *et al.*[172]

To verify that each MPBs composition had successfully been translated into differences in amphiphilicity, each brush's T_{CP} was measured using DLS. These measurements exploited the polymers' LCST (lower critical solution temperature) behaviour which specifically entails a transition of the polymers from a fully solubilised state at low temperatures to a collapsed, globular form in aqueous environments as the temperature increases above their cloud point temperature (T_{CP}). This thermosensitive behaviour relies on the balance struck between bonds formed by the polymer chains with water molecules and with itself.[171] Below the T_{CP}, LCST-type polymers remain hydrophilic as their favourable interactions with solvating water molecules dominates, especially in the case of the oligo(ethylene glycol)-based monomers used here which can form hydrogen bonds via their oxygen atoms.[173] Conversely, elevated temperatures drive a net loss in polymer-water associations, thus triggering the hydrophobic effect and the polymers' intramolecular dehydration and collapse.[174,175] The LCST effect has been well documented in oligo(ethylene glycol)-based copolymers,[176,177] and has further been shown to be dependent on factors such as the number of ethylene glycol repeat units incorporated into the OEGMA-derivatives used.[178] In the case of this specific monomer class, polymer hydrophilicity is enhanced by virtue of increasing the ethylene glycol (EO) repeating units used and thus the available sites for polymer-water interactions. Correspondingly, it is expected that the T_{CP} of the MPBs would decrease with an increase in their hydrophobicity, which was observed accordingly in the phase transition curves of the MPBs as discerned via changes in their transmittance using UV-Vis spectroscopy or particle size using DLS (**Figure 2.7**). Measured T_{CP} values, along with other important chemical and physical information on the MPBs are summarised in **Table 2.1.**

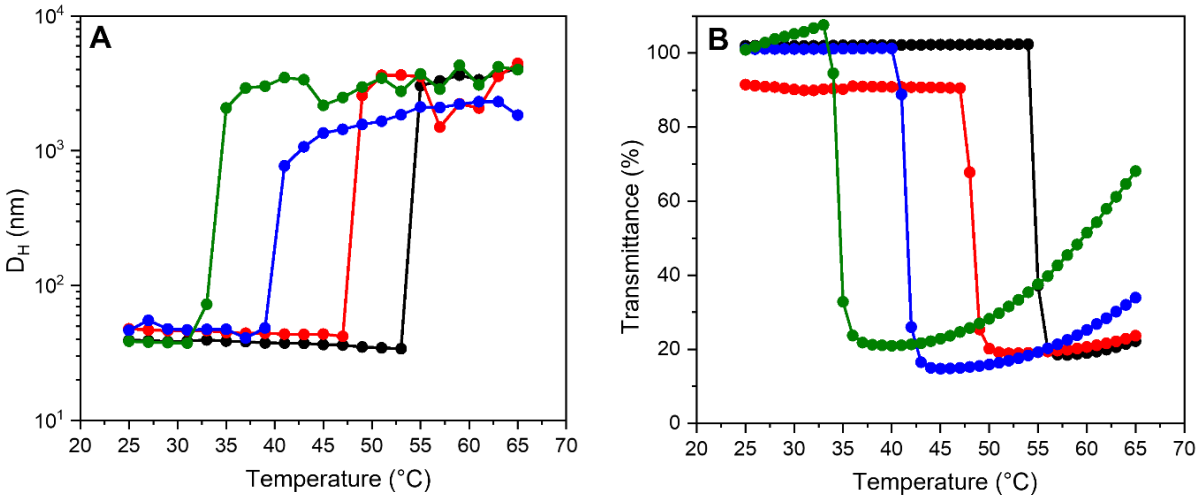

Figure 2.7. T_{CP} curves used to determine each MPBs' amphiphilicity as a function of **(A)** hydrodynamic diameter and **(B)** optical transmittance; D0% (black), D20% (red), D40% (blue) and D60% (green). MPB sample solutions were prepared and measured in PBSx1 (0.5 mg mL^{-1}). Adapted from Ramamurthi *et al.*[172]

Table 2.1. Summary of the chemical and physical properties of the MPB series

MPB	DP_{SC}	Mn_{NMR} (g mol^{-1})	Mn_{SEC} (g mol^{-1})	Z-average D_H (nm)	T_{CP} (°C) in PBSx1
D0%	152	358,000	1,110,000	40.0	55
D20%	160	318,000	1,079,000	46.1	49
D40%	160	351,000	990,000	41.0	39
D60%	164	346,000	923,000	40.0	35

Post-synthetic functionalisation of the MPBs to enable their observation in vitro and in vivo was accomplished via the GMA subunits comprising part of the sidechains. In a two-step modification, the epoxide groups of GMA were first converted to azides via an acid-catalysed ring-opening reaction. Dual analysis of the post-functionalised MPBs using ^1H NMR and IR spectroscopy confirmed the success of the conversion (**Figure 2.8** and **Figure 2.9**). Upon reaction, the weak signals formerly assigned to the GMA protons could

not be distinguished in the resultant ^{1}H NMR spectrum, as indicated in **Figure 2.8(B)**. IR spectroscopic analysis corroborated this further through the appearance of a stretch signal distinctive of an azide group (**Figure 2.9**, ca. 2100 cm^{-1}).

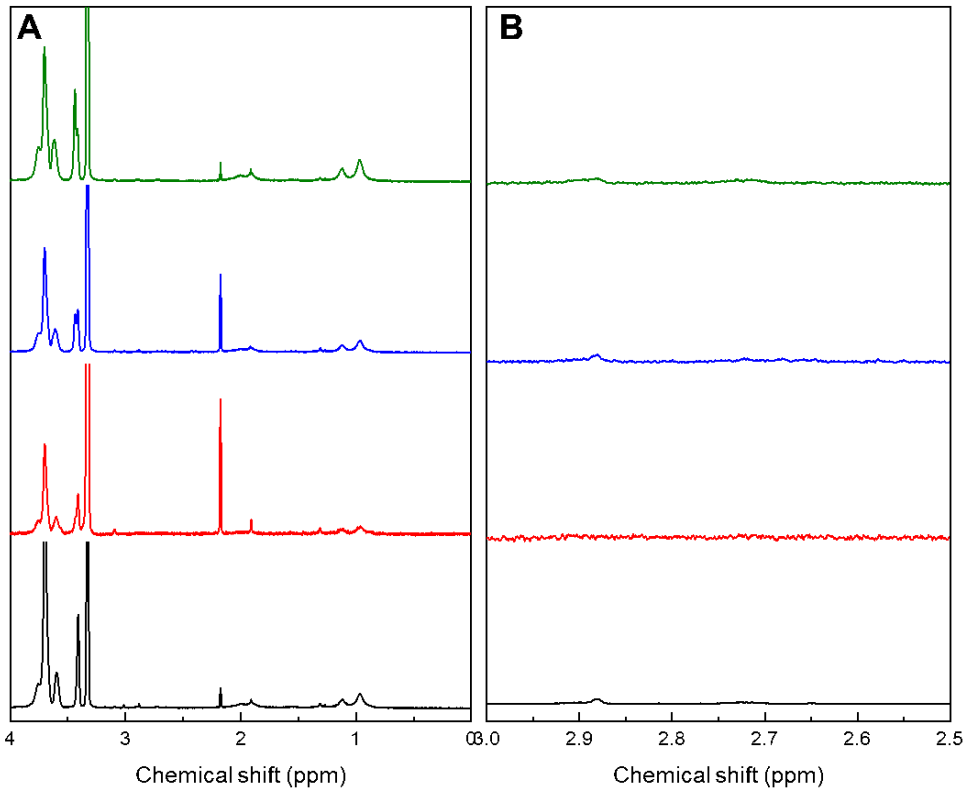

Figure 2.8. (A) Overview of NMR spectra of the amphiphilic MPBs; D0% (black), D20% (red), D40% (blue) and D60% (green) after azidation. The absence of signals pertaining to the former epoxide groups of GMA (magnified view shown in (**B**) between 2.5 – 3.0 ppm) supports their successful conversion into azido- moieties. Adapted from Ramamurthi *et al.*[172]

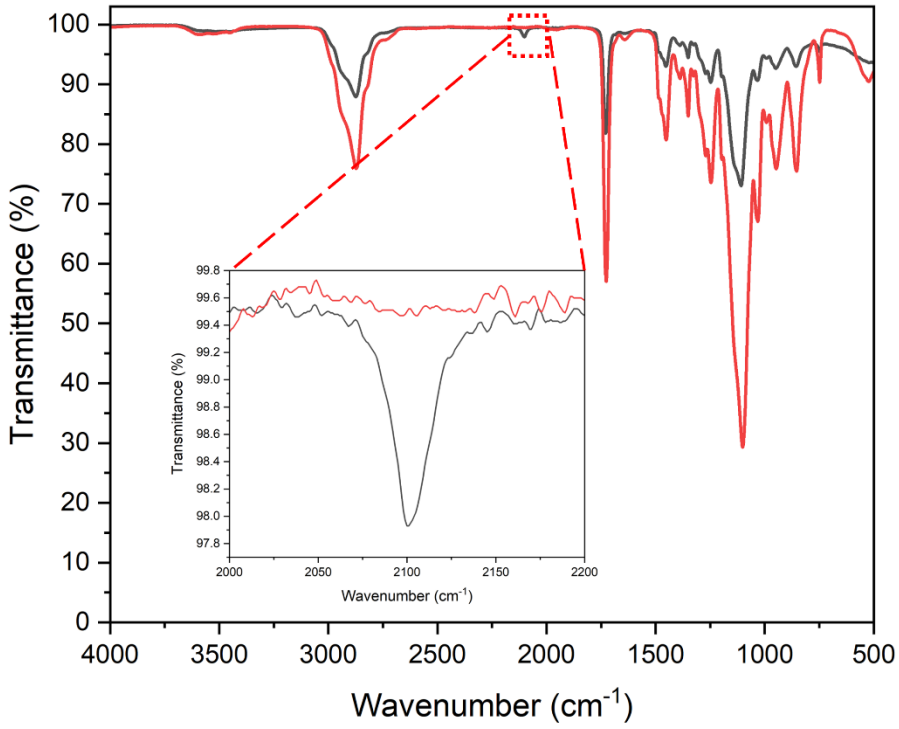

Figure 2.9. IR spectrum of a representative MPB sample before (red trace) and after (black trace) azidation. The presence of the pertinent azide stretch manifested as a new signal at approximately 2100 cm^{-1} (inlaid). Adapted from Ramamurthi *et al.*[172]

Following epoxide conversion, each brush's azide groups were used in a copper-catalysed azide alkyne cycloaddition (CuAAC) to attach an alkyne functionalised dye (either ATTO633 or Cy5) to permit their tracking in subsequent in vitro and in vivo tumour models. Fluorescence spectroscopy confirmed the successful dye attachment via the appearance of a strong emission peak at 650 nm and 670 nm for ATTO633-coupled MPBs and for Cy5-coupled MPBs (**Figure 2.10**).

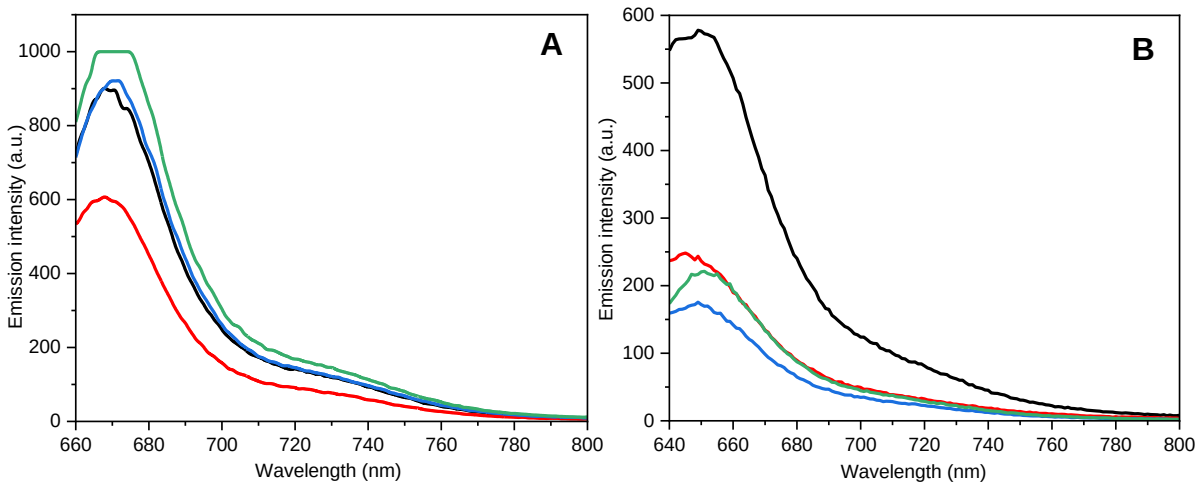

Figure 2.10. Emission spectra of (**A**) Cy5-tagged and **(B)** ATTO633-tagged MPB aqueous solutions; D0% (black), D20% (red), D40% (blue) and D60% (green) (λ_{ex} = 650 nm and 630 nm for Cy5- and ATTO633-tagged MPBs respectively). Adapted from Ramamurthi *et al.*[172]

With the MPB library synthesized with variable amphiphilicity levels and comparable dimensions, confocal laser scanning microscopy (CLSM) was used to probe the effects of each brush's amphiphilicity on their association with cancer cells and tumours in vitro. Initial experiments were conducted using two-dimensional (2D) monolayer cultures sourced from DLD-1 (an epithelial colorectal cancer line) and A549 (an epithelial lung cancer line) cells. Once monolayers had been grown to sufficient densities, they were incubated with MPBs (c = 0.2 mg mL^{-1} in PBSx1) for 24 h before imaging. Results of fluorescence CLSM imaging are shown in **Figure 2.11** and **2.12**. From evaluation of images from both cell lines, a common trend was observed wherein D0%, D20 and D40% experienced appreciable cellular association. Contrastingly, the association of D60% with both DLD-1 and A549 cells was negligible, exhibiting only sparse, highly intense fluorescence strongly indicative of nanoparticle aggregates. From this, we surmised that the thermoresponsive behaviour of D60% would be the primary factor in hindering its cellular association and uptake, as its low T_{CP} (35 ˚C) compared to the rest of the series

would trigger its premature dehydration and aggregation when incubated in the presence of the cell monolayers at 37 ˚C. The excessively large D60% intermolecular aggregates would likely encumber their subsequent endocytosis, thus leading to low cellular uptake. In that regard, D60% can be seen as an outlier in the MPB series wherein its T_{CP} falls lower than the incubation temperature used in most of this works' in vitro experiments. A more interesting analysis and comparison can be made between D0%, D20% and D40%, whose T_{CP} values all fall above 37 ˚C. In the case of D0%, its fluorescence intensity alongside DLD-1 cells, whilst appreciable compared to D60%, was noticeably subdued compared to the intermediately hydrophobic particles D20% and D40%. This was a trend that was similarly observed in the A549 cell line.

The patterns of MPB cellular association observed in both cell lines thus far may be attributed to several mechanisms proposed by past similar studies. Many of the theories to explain our findings are based on the characteristic coil-globule transition experienced by polymers upon dehydration above their T_{CP}. In agreement with this principle, work carried out by Salmaso et al. demonstrated the importance of the nanoparticle hydrophobic-hydrophilic balance in cellular trafficking.[179] In their work, inorganic gold nanoparticles were affixed with thermoresponsive poly(N-isopropyl acrylamide-co-acrylamide) chains, thus endowing them with LCST-like behaviour. When incubated alongside MCF-7 breast cancer cells, the gold nanoparticles were found to be internalised in an LCST-dependent manner, wherein endocytosis was significantly enhanced when the polymers had switched to a dehydrated globule-like state. The heightened surface hydrophobicity, as posited by the authors, may have encouraged the adsorption of serum proteins favourable to cell endocytosis hence triggering an increase in uptake. This trend has been independently detected in work conducted by Kurzhals *et al.* using SPIONs (super paramagnetic iron oxide nanoparticles) functionalised with polyoxazoline-derived copolymers, specifically

using poly(2-isopropyloxazoline) (PIPOX) and poly(2-ethyloxazoline) (PETOX).[180] The specific composition of the polymers was tailored to produce a series of nanoparticles with different T_{CP} values, and subsequently tested with cervical cancer HeLa cells. Unlike Salmoso, Kurzhals *et al.* attributed the favourable endocytic effects of SPIONs with lowered T_{CP} values to their ability to form slightly larger, metastable aggregates at lower temperatures that could be easily internalised.

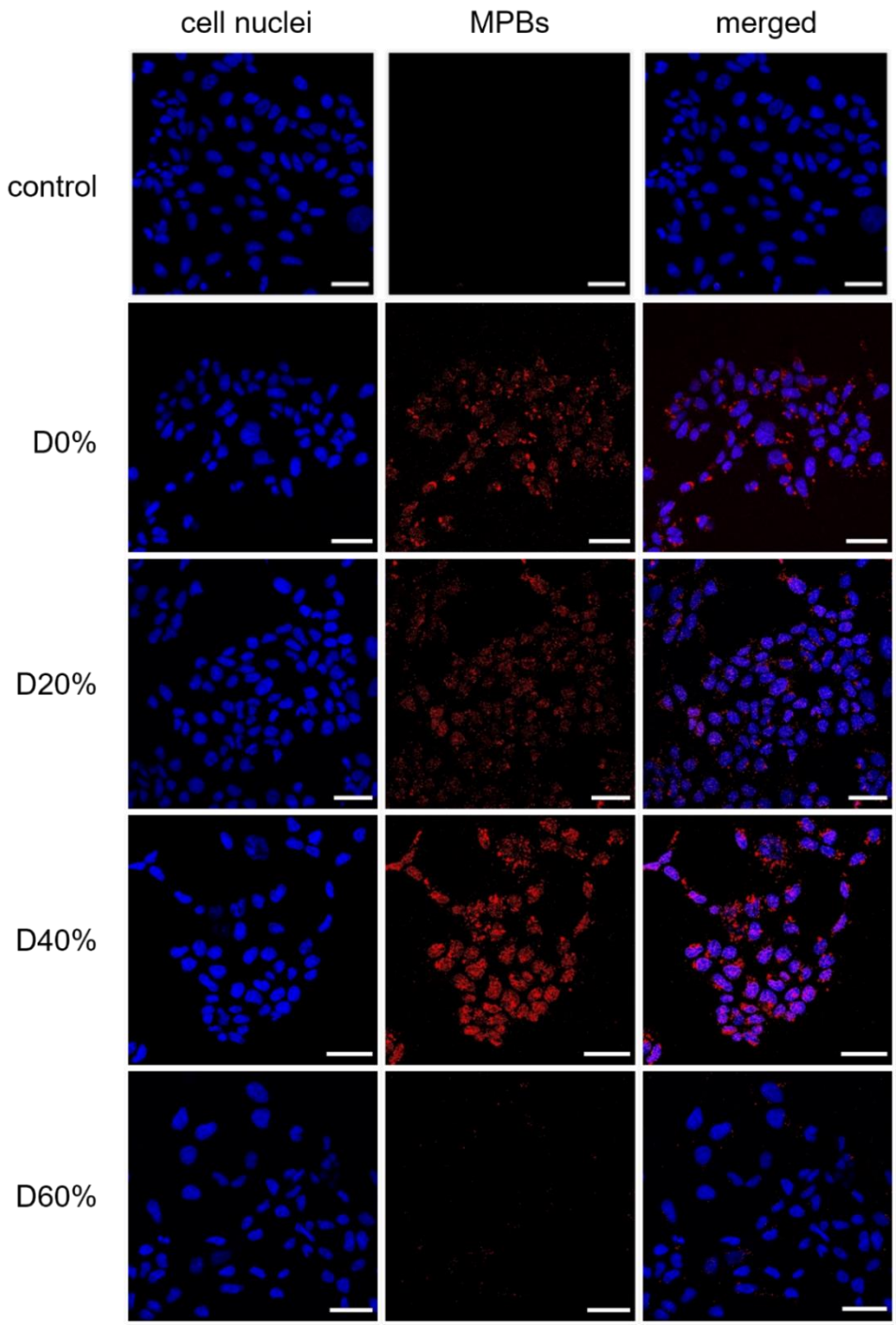

Figure 2.11. CLSM images of DLD-1 cell monolayers after 24 h incubation with ATTO633-tagged MPBs; D0%, D20%, D40% and D60% (images of a negative control monolayer featuring no MPBs are included in the top row). Fluorescence channels are divided into columns consisting of fluorescence emitted by cell nuclei (right), ATTO633-tagged MPBs (middle), and both nuclei and MPBs fluorescence channel merged (right). Scale bars = 50 μm. Adapted from Ramamurthi *et al.*[172]

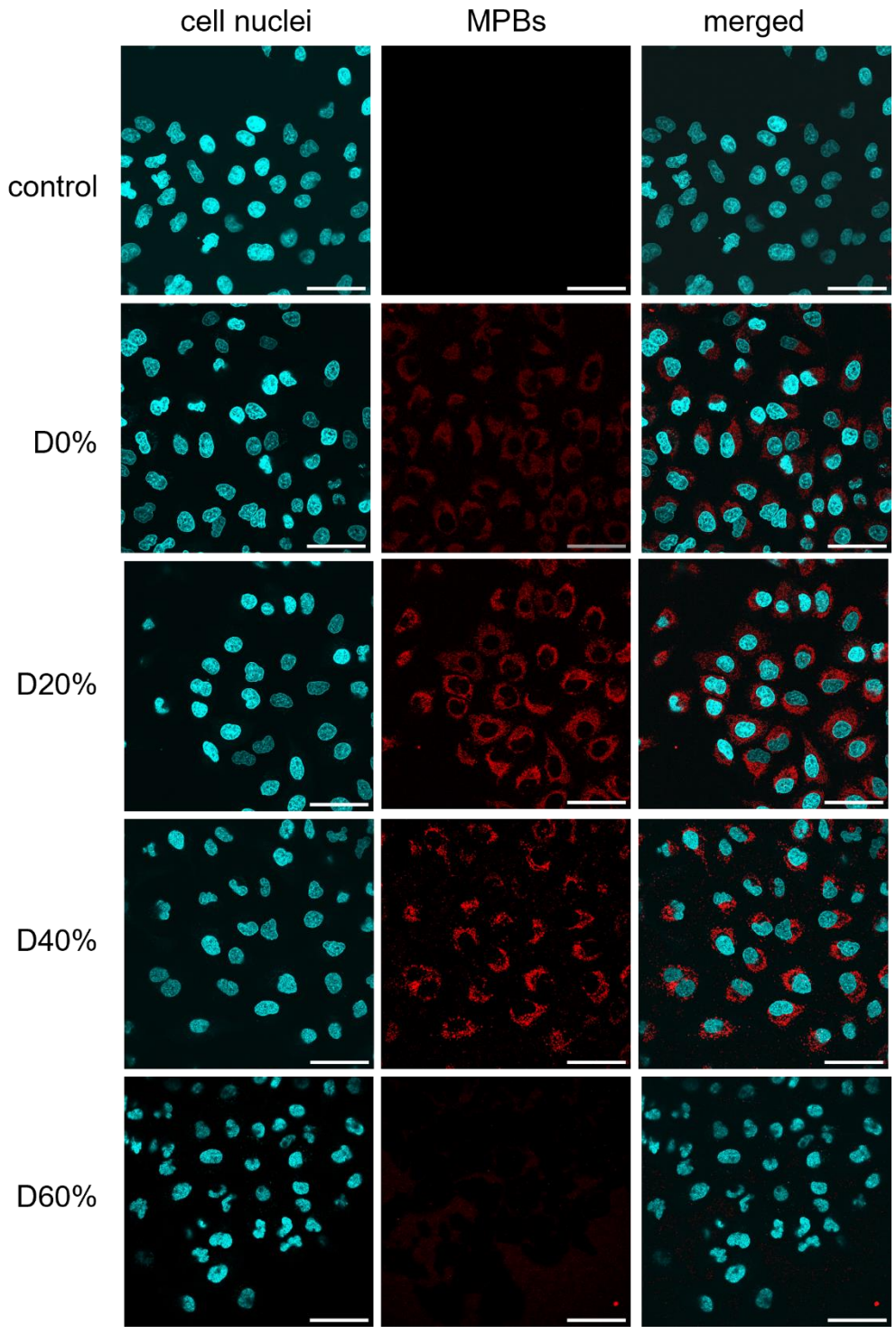

Figure 2.12. CLSM images of A549 cell monolayers after 24 h incubation with ATTO633-tagged MPBs; D0%, D20%, D40% and D60% (images of a negative control monolayer featuring no MPBs are included in the top row). Fluorescence channels are divided into columns consisting of fluorescence emitted by cell nuclei (right), ATTO633-tagged MPBs (middle), and both nuclei and MPBs fluorescence channel merged (right). Scale bars = 50 µm.

In order to further probe the amphiphilicity-dependence of tumour penetration by the MPBs, we next assessed their uptake in more complex, 3D MCTSs. DLD-1 cells were chosen as the starting cell line to grow the spheroids as they were found to be much more suitable for this purpose compared to A549 cells. As a preclinical nanomedicine screening platform, MCTSs represent a much more complex and faithful model of the tumour microenvironment compared to cell monolayers and have already been exploited to study parameters such as drug efficacy and nanoparticle tumoural penetration. Due to the proximity in which the cells comprising the spheroid are packed, these three-dimensional models feature layered cell populations, analogous to those found in clinical tumours, as well as gradients in oxygen and pH. To analyse the distribution of MPBs throughout the spheroids, epifluorescence images were captured at three equidistant depths of the MCTS (25, 50 and 75 μm; **Figure 2.13**). Due to the limited resolution of the microscope more than 150 μm above the objective, images beyond this depth could not be satisfactorily obtained. Even within this limited range however, there are key differences in tumour penetration between some of the amphiphilic nanoparticles, mirroring the observations made previously with the cell monolayers. Again, the presence of the most hydrophobic MPB (D60%) was insignificant even at shallow depths of 25 μm, likely due to its thermally-induced aggregation into sub-micron to micron-sized particles at the incubation temperatures used (37 °C). Considering the limited interstitial space between the spheroids' tightly packed cells, we envisage that the resultant agglomerates would be significantly encumbered as they attempt to diffuse through these junctions in the MCTS. On the other hand, D0%, D20% and D40% all underwent appreciable penetration into the tumour spheroids, up to the maximum observed depth of 75 μm. Nonetheless, their penetration into the core regions starts to be hindered at this point, seen clearly as high

intensity regions of MPB fluorescence mainly localised at the periphery, rather than throughout the tissue as observed at 75 and 50 µm.

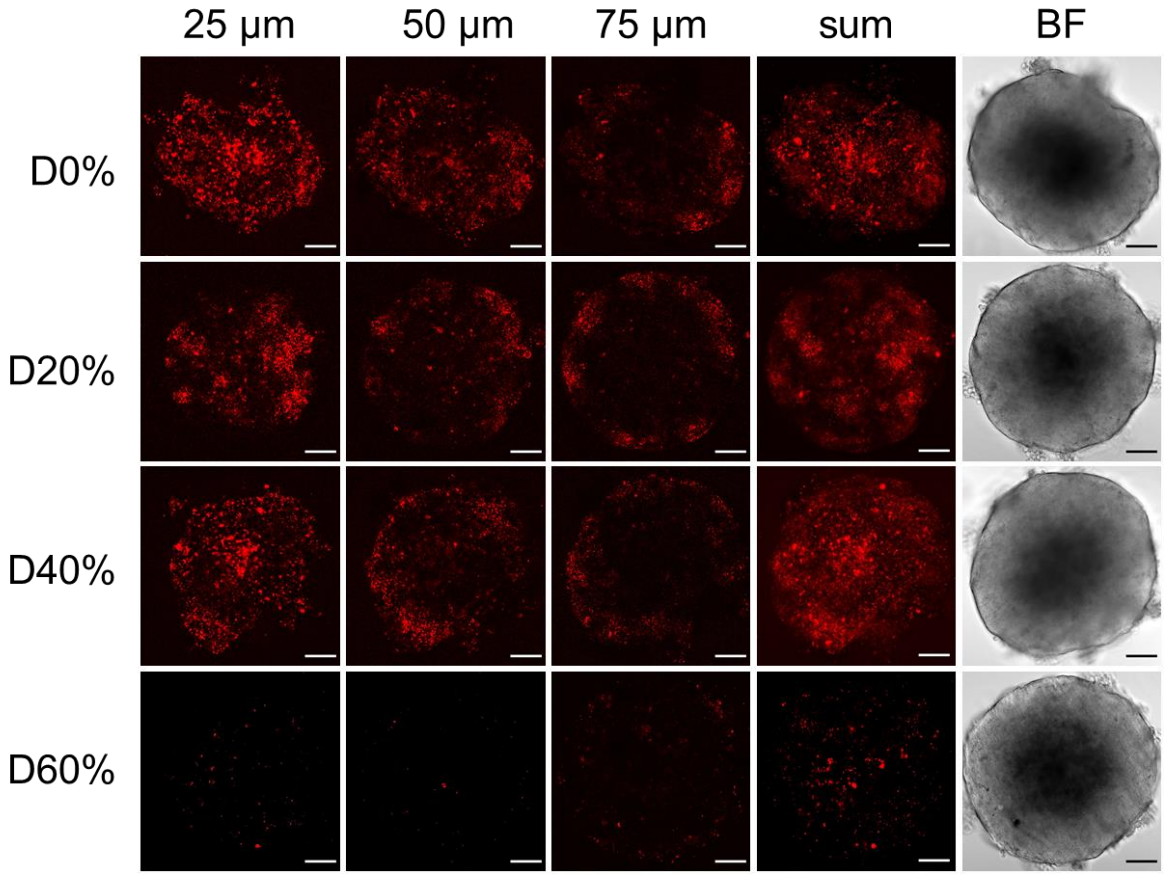

Figure 2.13. CLSM images of DLD-1 multicellular cancer cell spheroids after 24 h incubation showcasing different penetration levels of A) D0%, B) D20%, C) D40%, and D) D60% at different depths within the tumour (red fluorescence, columns 1st – 3rd columns). Sum images of z-stacks from 0 to 75 µm were obtained to give an overall indication of each MPBs tumour penetration efficiency (4th column). Brightfield (BF) images of each tumour spheroid were also taken to establish spheroid viability (5th column). Scale bars = 100 µm. Adapted from Ramamurthi *et al.*[172]

As a quantitative measure, flow cytometry was used to analyse and verify the findings made with confocal microscopy, as the former is often limited to only giving qualitative indications of nanoparticle-cell association. Like confocal microscopy, flow cytometry is a powerful high throughput technique that directly relies on measurement of fluorescent

signals that can stem from the cell or an appropriately tagged fluorescent nanoparticle, as these MPBs are. In conditions similar to those used in the in vitro monolayer and spheroid experiments, A549 cells were incubated with MPBs (c = 0.2 mg mL^{-1}, 37 °C) for 4 and 24 hours before harvesting and analysis, with results represented as MFI (mean fluorescence intensity) of the particles' fluorescence when excited at 630 nm (the excitation wavelength of ATTO633). To ensure the validity of the measurements, a sequential gating strategy was applied to the analysed cell samples to isolate single, viable cells and thence derive the relevant MFI value, as demonstrated in **Figure 2.14** on a sample of untreated A549 cells. From the initial population, the first gate (P1) was applied to a plot of the forward scatter area (FSC-A) and side scatter area (SSC-A), to distinguish viable cells from smaller cell debris. From the P1 population, multicellular aggregates were filtered from the analysis by mapping the FSC-A against the cells' forward scatter height (FSC-H), yielding a population of single cells (P2). Next, the side scatter area of cells of the P2 population was compared with their side-scatter height (SSC-H) as an additional measure to filter out nonviable cells to give the final population of interest (P3). From this final population, the ATTO633 fluorescence intensities of individual cells can be measured and processed into a histogram to derive the relevant MFI values. The MPBs association with A549 cells after 24 h of incubation is represented in **Figure 2.15**, highlighting the exceptionally increased association of D20%, followed by D40%, D0% and D60%. The heightened association of the two intermediately hydrophobic MPBs (especially D20%, whose association is almost 2-fold that of D0%/D60%) seems to suggest an intermediate hydrophilic-hydrophobic balance may favour enhanced cellular uptake. It is also interesting to observe that even though D60%'s premature aggregation would have severely compromised its cell internalisation efficacy, D0% exhibits similarly low cell associations not significantly different from D60%.

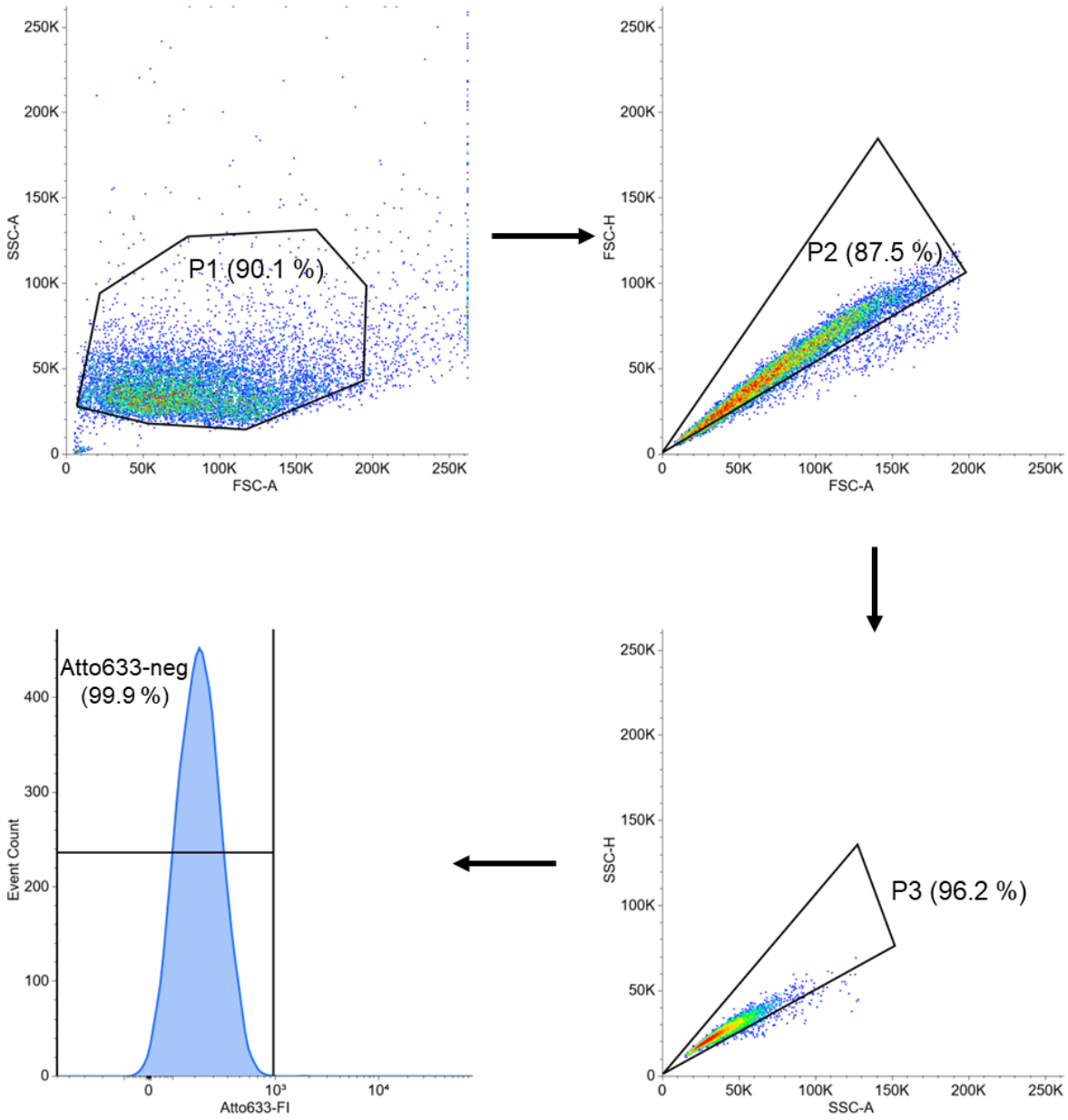

Figure 2.14. The cell gating workflow used on untreated A549 cells during flow cytometric analyses to isolate viable cells for MFI measurements. Successive gates to exclude cell debris (P1) and multicellular aggregates (P2, P3) yielded a cell population (P3) from which cell autofluorescence could be detected (histogram, bottom left panel) and appropriately excluded from MFI measurements of MPB-treated cells. The proportion of cells as a percentage of its parent population post-gating is indicated in brackets.

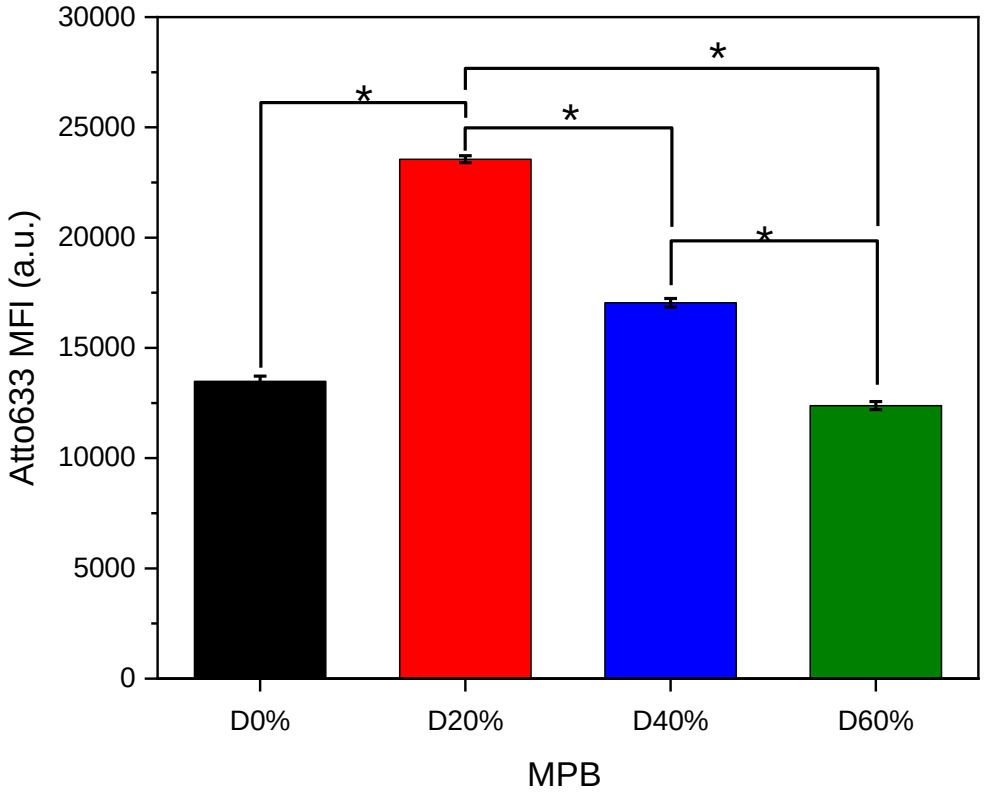

Figure 2.15. MFI values (representing overall cellular association levels) obtained from flow cytometry analyses of ATTO633-tagged MPBs incubated with A549 cell monolayers after incubation for 24 h.

In vivo analysis was carried out next to better understand how each MPBs hydrophilic-hydrophobic balance would lead to changes in their biodistribution and tumour homing using more comprehensive biological models. To accomplish this, tumours derived from subcutaneous A2780 ovarian cancer cells were cultivated in nude mice to be used as the *in vivo* model of choice. A portion of the azido-functionalised MPBs were subsequently tagged with Cy5 alkyne via the CuAAC reaction used previously, enabling them to be monitored once injected into the mice using IVIS imaging. Once tumours had reached adequate volumes of 200 – 300 mm^3 11 days post-inoculation, the Cy5-labelled MPBs were intravenously injected at a total concentration of 4 mg mL^{-1}. The mice were then

imaged post-administration at 9 h, 24 h and 48 h time-points to evaluate the MPBs' long and short-term biodistribution and tumour accumulation, the results of which are visualised in **Figure 2.16**.

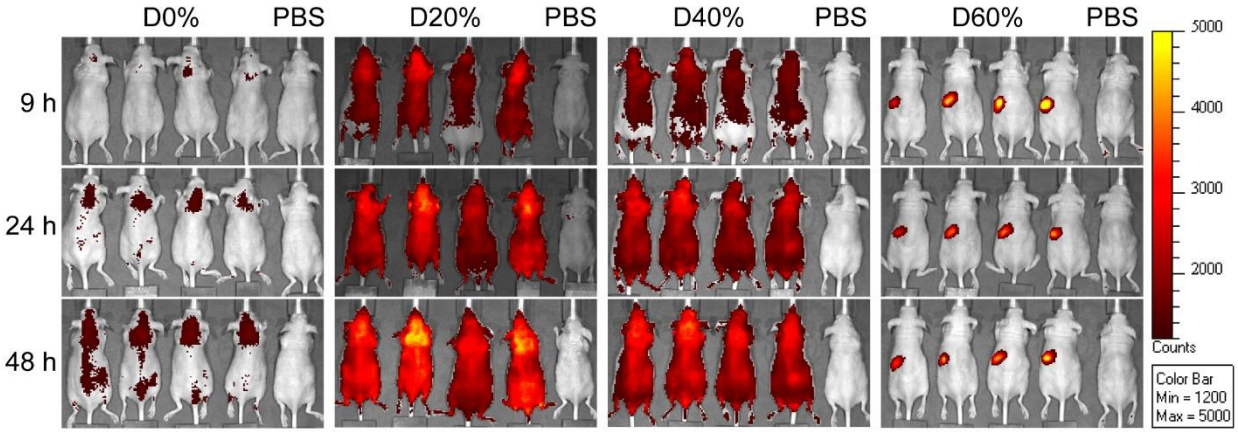

Figure 2.16. Live dorsal images collected from sacrificed A2780 tumour-bearing mice post-administration of each MPB. Mouse specimens used as negative controls were injected with PBSx1 saline solution containing no MPBs and are represented as the last specimen in each row for each MPB. Adapted from Ramamurthi *et al.*[172]

Regardless of circulation time, preliminary IVIS imaging of the euthanised mice showed D0% exhibiting minimal fluorescence at 9 h post-administration, although long-term circulation was maintained overall, leading to an increase in delocalised distribution throughout the mice's organs. By contrast, D20% and D40%'s accumulation was substantial even at 9 h compared to D0%, which only increased further (judging from the strength of their fluorescence signals) up to 48 h post-administration. Similar to D0% however, the observed pattern of D20% and D40%'s apparent fluorescence was highly diffuse throughout the bodies of the mice models used, implying non-specific biodistribution and prolonged circulation lifetimes. Converse to the biodistribution trends noticed so far, Cy5 fluorescence of the D60% MPB was chiefly sequestered within the spleen and remained mostly unchanged at 24 h and 48 h post-administration.

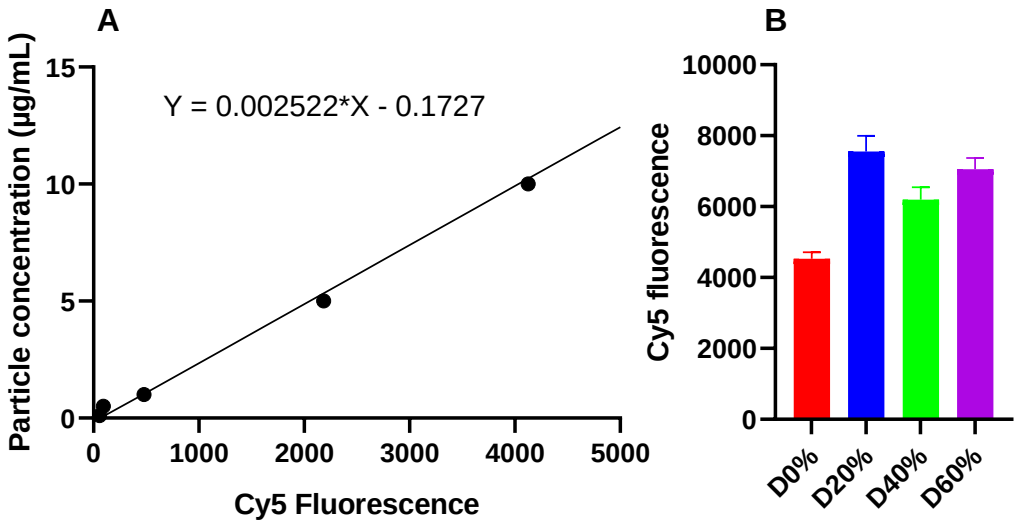

Figure 2.17. (A) Standard curve relating the Cy5 fluorescence and mass concentration of D0%. **(B)** Measured Cy5 fluorescence intensities of solutions of the tagged MPBs (0.01 mg mL^{-1}). Intensity values for each particle are represented as means ± SEM (n = 3). Adapted from Ramamurthi *et al.*[172]

To gain a more detailed insight into the MPBs' systemic distribution as a function of their hydrophobicity, xenograft mice organs and tumours were harvested and imaged ex vivo at 24 h and 48 h after MPB administration. Once imaged, the collected organs were afterwards homogenised and analysed via a fluorescence plate reader to quantify the total accumulated quantity of MPBs per organ via fluorescence (Figure 2.19). However, given that the different MPB formulations displayed varying fluorescence emission intensities after appending with Cy5, it was necessary to develop a standard curve to account for these differences in emission. This was accomplished using measured emission values from the MPBs at 0.01 mg mL^{-1}, from which intensity ratios between the MPBs to D0% were calculated; D0% / D20% = 0.599, D0% / D40% = 0.731 and D0% / D60% = 0.642. The obtained ratios could subsequently be substituted into the standard curve equation, allowing individual MPB mass concentrations in the tumour and other organs to be

determined. Overall, the data collected at 24 h from both IVIS imaging and plate-reader based assays shows D0%, D20% and D40% being primarily captured in the liver and the spleen, both the primary organs of the RES system. Across these three MPBs, uptake in the liver was marginally higher than in the spleen (1.3 – 1.5-fold). This trend persisted upon 48 h of incubation. The drastically different biodistribution of D60% observed in the harvested organs was confirmed via the plate-reader assay, wherein an extremely high fraction of the D60% dose was detected in the spleen (1023 ng at 24 h, 1327 ng at 48 h) as shown in **Table 2.2** and **Figure 2.19**. A potential cause for this extremely heightened splenic uptake could be the thermally-induced phase transition of D60% as noted previously. At the elevated temperature of the mice models (36.6 °C), D60%'s dehydration and collapse into much larger and hydrophobic aggregates may drive its early capture by the liver's Kupffer cells and the spleen's macrophages, which are known to quickly clear particles in the 100–- 200 nm size range, with increasing particle size favouring splenic capture compared to liver accumulation.[181] In cases where particles exceed 200 nm in size, their ability to be transported across the endothelial slit of splenic sinuses is compromised, leaving them to accumulate within the red pulp regions of the spleen to be cleared later by resident splenic macrophages.[182–185] Nevertheless, the majority of all the MPBs were deposited in the spleen and liver, implicating their primary capture by macrophages that led to early clearance (**Table 2.2**, **Figure 2.19 A, D**).[68]

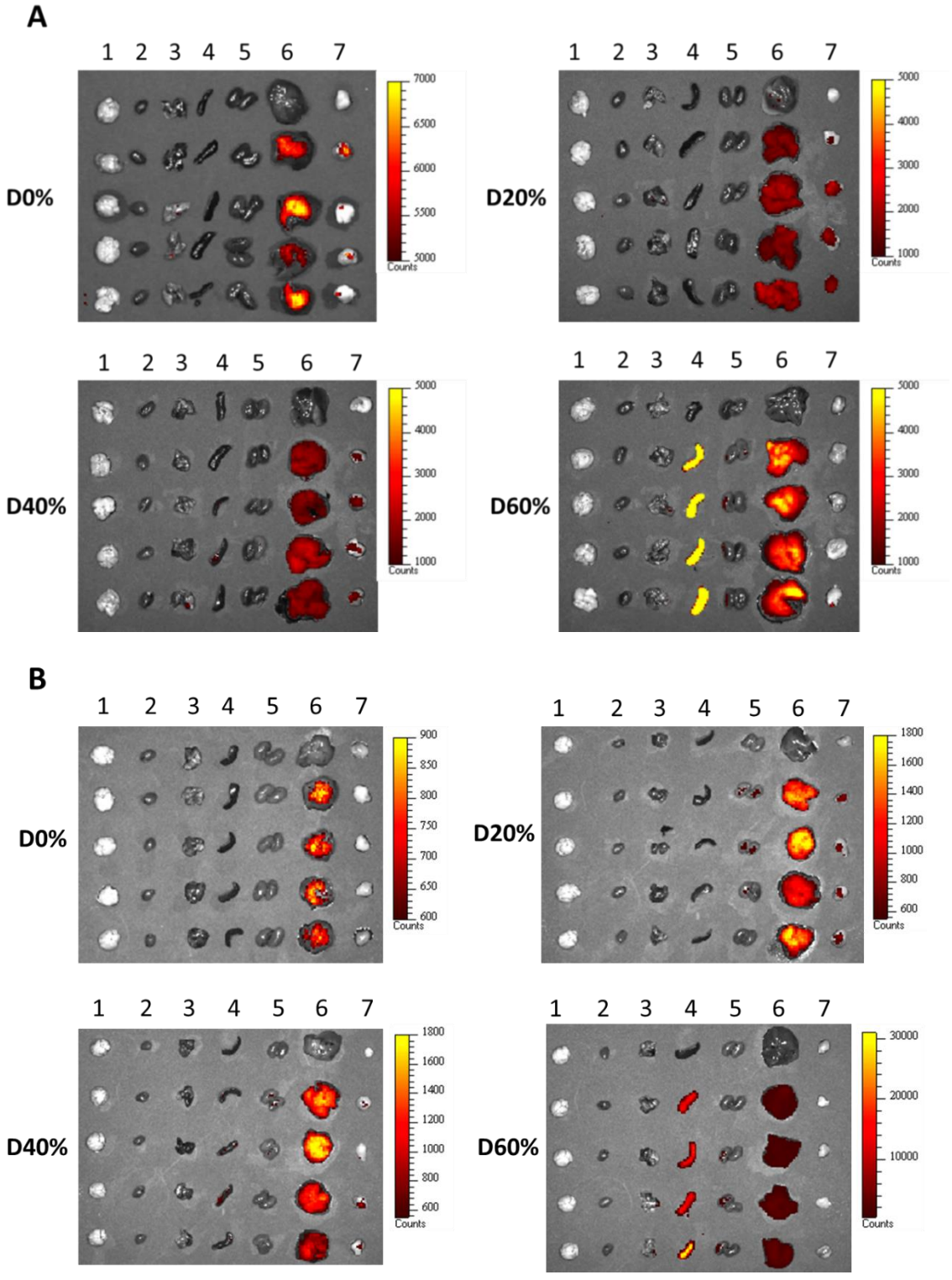

Figure 2.18. IVIS images collected of key organs harvested from tumour-bearing nude mice at **(A)** 24 h and **(B)** 48 h post-administration of Cy5-labelled MPBs. Replicate whole-organ images were taken from (1) brains, (2) hearts, (3) lungs, (4) spleen, (5) kidneys, (6) liver and (7) A2780 tumours. Adapted from Ramamurthi *et al.*[172]

Table 2.2. Uptake levels of MPBs in tumours and RES clearance organs (liver and spleen). Adapted from Ramamurthi *et al.*[172]

MPB uptake (ng MPB mg^{-1} organ)	D0%		D20%		D40%		D60%	
	24 h	**48 h**	**24 h**	**48 h**	**24 h**	**48 h**	**24 h**	**48 h**
Liver	16.2	21.1	21.2	29.9	30.7	45.5	27.3	57.3
Spleen	13.0	14.6	14.5	19.6	20.9	31.7	1023	1327
Tumour	5.2	3.2	6.3	8.5	6.2	8.0	2.0	2.3

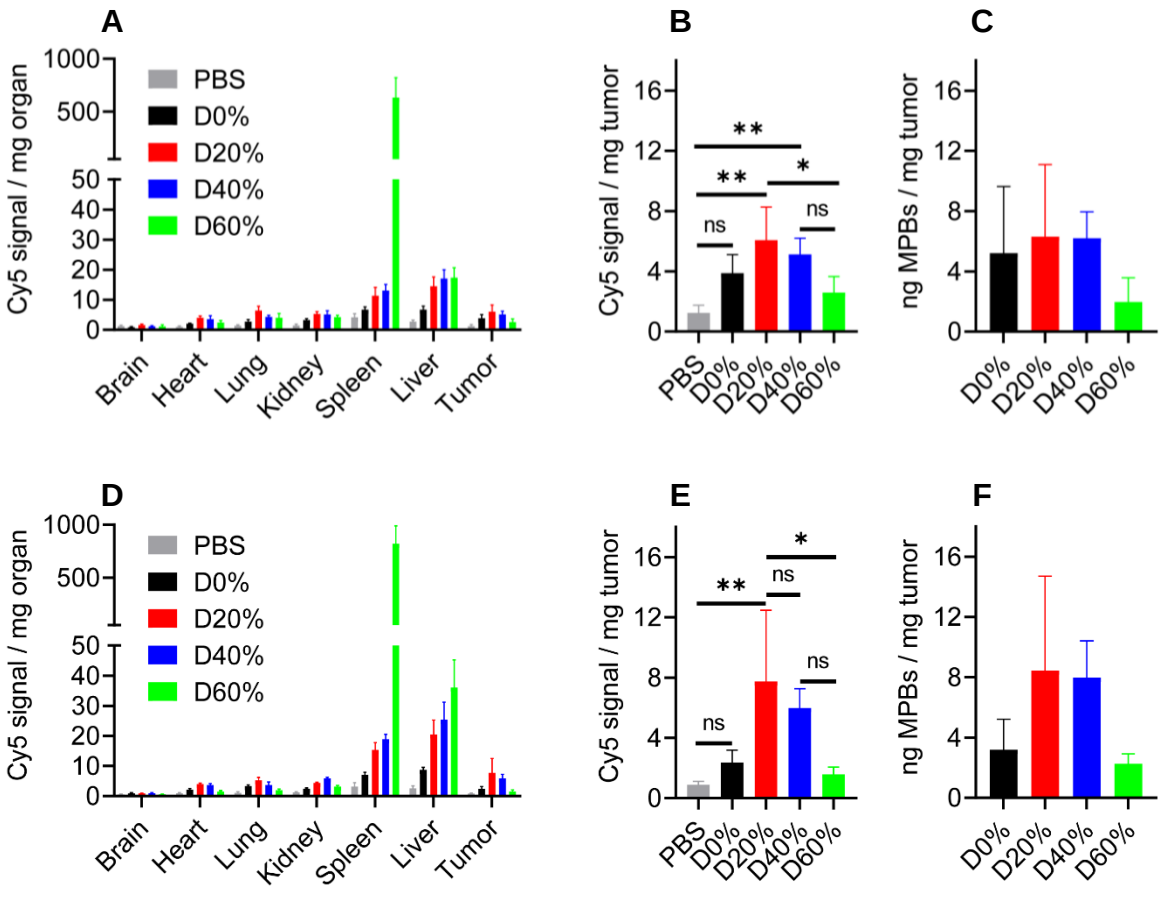

Figure 2.19. Biodistributions of Cy5-labeled MPBs post-intravenous bolus administration in A2780 tumour-bearing NCR nude mice. Plate reader measurements of each organ's fluorescence signal at **(A, B)** 24 h and **(D, E)** 48 h post-administration. Post-harvesting tissue homogenization allowed the amount of MPBs accumulated in tumours at **(C)** 24 h

and **(F)** 48 h to be measured using the standard curve. Data are presented as means ± SEM (n = 4). * denotes p-values < 0.05 and ** denotes p-values < 0.01. Adapted from Ramamurthi *et al.*[172]

From our analysis of the broad biodistribution patterns of the MPBs and its dependence on their hydrophobicity, we next examined the particles' performance in tumour homing in vivo. IVIS analyses of the tumours 24 h and 48 h post-administration showed tumoural accumulation of D0%, D20% and D40% via their Cy5 fluorescence (**Figure 2.18 A** and **B, column 7**). This finding was further supported by plate-reader measurements of homogenised tumour tissue at both timepoints (**Figure 2.19, B-C, E-F**). For reasons previously linked to premature macrophage-mediated clearance, D60% was notably absent or achieved negligible levels in the tumour compared to the rest of the MPB series. In focusing on D0% compared to D20%, an interesting finding was made when comparing their levels 24 h and 48 h post-administration. While D0% managed to achieve respectable levels at 24 h (5.2 ng), its levels noticeable fell to 3 ng a further 24 h after that, indicating favourable initial tumour deposition but compromised long-term retention. Conversely, D20% and D40% achieved the highest initial levels in the tumour at 24 h after their administration (6.3 and 6.2 ng respectively), and their long-term accumulation only increased to 8.0 – 8.5 ng at 48 h. Taking these results together seemingly implies that although nanoparticle hydrophilicity may favour sufficient tumour accumulation in the short-term, longer-term accumulation of nanoparticles in tumour tissue is dependent to an extent on increased particle hydrophobicity.

2.5. Conclusions

In this chapter, the versatility of MPBs as nanoparticle platforms for structure-function-property studies was demonstrated to study the effects of nanoparticle hydrophobicity on their efficiency in associating with cancer cells and tumours. This was achieved via careful control of the MPBs' composition of hydrophilic and hydrophobic monomers in their sidechains, affording four particles with distinct hydrophobicity levels. We subsequently used this particle array against in vitro cancer cell/tumour models which showed moderately hydrophilic/hydrophobic particles achieving optimal uptake and association levels. To advance the study, the tumour accumulation behaviour and biodistribution of the particles in the context of nanoparticle hydrophobicity was then examined in more complex in vivo tumour-bearing mice models. As expected, the majority of the injected particles was sequestered in the MPS clearance organs (spleen, liver and kidney), regardless of their hydrophilic-hydrophobic character. The most hydrophobic particle D60% however was found to a much greater extent in the MPS clearance organs than the other MPBs. When focusing on the mice tumours specifically, the role of nanoparticle hydrophobicity was apparent in dictating the MPBs' initial tumour accumulation and long-term retention. In this case, the moderately hydrophobic MPBs D20% and D40% not only showed enhanced initial tumour deposition compared to the other particles, but their levels also improved from 24 h to 48 h. The high hydrophilicity of D0% on the other hand compromised its long-term accumulation, leading to a noticeable drop in levels in the same time period. By contrast, D60% showed consistently low levels within the tumour, which did not improve with time. In summary, our findings gleaned from these in vitro and in vivo cancer models have validated the important role played by the hydrophilic-hydrophobic balance of nanoparticles in governing their biological interactions and fate,

which will be particularly relevant for informing future tumour-homing nanoparticle designs.

CHAPTER III

Influence of the Hydrophilic-Hydrophobic Balance of Molecular Polymer Brushes on their Serum Protein and Cell Membrane Interactions

3.1. Abstract

The third chapter advanced the findings of the previous chapter to investigate whether the hydrophilic-hydrophobic balance of the MPBs would trigger substantial differences in the particles' affinity with serum proteins and associations with cellular membranes. The study was performed with the intention of better determining whether the intermediate hydrophobicity levels of D20% and D40% led to the formation of protein coronas that boost their uptake in cancer cells, as was observed in the previous work. To that end, size analyses via DLS of the particles in serum-containing conditions indicated that all the MPBs, with the exception of D60%, possessed relatively good stability with no apparent protein adsorption at 37 °C. However, the relevance of the MPBs interactions with proteins was more apparent when the MPBs were tested for cancer cell association under different serum conditions. Even though the moderately hydrophobic particles showed the highest uptake in the presence and absence of proteins, a conspicuous reduction in cell uptake was noted when the MPBs were incubated alongside serum proteins, thus highlighting the importance of the corona in governing the biological activity of nanoparticles. Even so, the MPBs differing hydrophobicities exerted insignificant effects on their translocation and disruption of model cell membranes. Moreover, all four MPBs exhibited low affinities for bovine serum albumin (BSA) when studied using isothermal titration calorimetry (ITC). We theorised that the non-existent effect of hydrophobicity in these experiments may be laid down to the similar hydration levels all the MPBs experience at temperatures below their cloud points (which was used in the model cell membrane and ITC experiments), leading to virtually similar behaviour in their protein and cell membrane binding.

3.2. Introduction

Practical application of engineered nanoparticles for tumoural drug delivery has so far proved advantageous compared to small-molecule drugs alone. Yet their behaviour transitioning from in vitro to complex animal/human models is often poorly regulated and unpredictable. This has often led to suboptimal clinical outcomes in terms of lowered intratumoural accumulation, overwhelming phagocytic capture and sequestration into MPS clearance organs, and cytotoxic side-effects. Resolving these persistent issues necessitates a comprehensive understanding of the events taking place at the nanoparticle-biological interface, which is often highly dynamic and thus presents a difficult area to fully elucidate. Amongst the interactions that nanoparticles can participate in with biological entities, the formation of the protein corona is often one of the most influential in mediating their biological fate. In theory, this corona arises upon the nanoparticles' immersion within biological fluids, triggering spontaneous adsorption of proteins on their surface.[186] The rapid encasing of the particle's surface in this way is encouraged to minimise the intrinsically high free surface energy of nanoparticles through a combination of charge neutralisation and shielding of hydrophobic surface regions.[28] Due to the degree of coverage imposed by the protein corona, nanoparticle behaviour and function in biological systems can be drastically altered in unpredictable ways, since the PC effectively superimposes its own 'identity' over that of the bare nanoparticle. From that point, the body essentially 'recognises' and acts upon the nanoparticle in accordance with the identity of the various proteins adsorbed, which often results in adverse effects to the nanoparticle's performance. So far, a wealth of research has demonstrated that the presence of the protein corona can result in heightened cytotoxicity, loss of colloidal stability, impaired endocytic uptake and tumoural accumulation, and greater immunogenicity. Since the establishment of the protein corona as an academic research

point and with growing recognition of the central role it plays in nanomedicine, efforts to control or at best, reduce protein adsorption onto nanoparticles has become a major endeavour.[187–189] However, it has been repeatably demonstrated that despite the ability of certain nanoparticles to supress protein adsorption to an extent with properly modified surfaces, protein fouling is not completely eliminated.[190–192] Underlying these attempts to control and diminish nanoparticle protein adsorption is the increasing awareness of a nanoparticle's intrinsic properties in dictating the character of the final protein corona. Synthetic aspects such as surface charge,[193,194] size,[195,196] and curvature[197] have proven to be influential in directing the identity and amount of proteins adsorbed as part of the 'hard' and 'soft' components of the corona, which in turn can have substantial effects on the particle's biological fate. Perhaps a factor of even greater significance to this phenomenon however is the nanoparticle's surface hydrophobicity, since hydrophobic interactions are one of the key means by which proteins associate with neutral, non-polar regions of nanoparticles.[198] Overall, the current array of studies looking into this property-behaviour relationship have largely implied that nanoparticle hydrophobicity governs not only the relative amount of proteins adsorbed,[84,199,200] but also the final corona's composition in certain cases.[201,202] In one of the earliest investigations in this direction, Linse *et al.* employed copolymer-based nanoparticles with different degrees of hydrophobicity, size and curvature, as regulated from the ratio of hydrophilic N-isopropylacrylamide (NIPAM) and the more hydrophobic N-tert-butylacrylamide (BAM) incorporated.[199] To study subsequent protein binding behaviour, isothermal titration calorimetry was used to model human serum albumin (HSA) adsorption onto the nanoparticles surface. Barring those particles bearing high surface curvatures, the most hydrophobic particles tested experienced 100% coverage with a dense layer of HSA, whereas only a sparse protein corona was formed on the most hydrophilic counterparts. In spite of the perceived effect

of the particles' hydrophobicity on their protein surface coverage however, ITC revealed little difference in affinity as indicated by similar measured K_A values. In a later study using a similar array of NIPAM/BAM-based nanoparticles, Linse *et al.* established differences in association/dissociation rates and corona composition dependent upon particle hydrophobicity.[84] Their study reported faster association and dissociation rates of certain protein types such as albumin and fibrinogen on the more hydrophobic 50:50 NIPAM/BAM particle surfaces, as validated by surface plasmon resonance (SPR) experiments. Apolipoprotein A-I by contrast experienced much longer residence times, and was detected in greater abundance (50 times more) on the 50:50 nanoparticle than on the hydrophilic 65:35 when analysed with SDS-PAGE (sodium dodecyl sulfate–polyacrylamide gel electrophoresis) and LC-MS (liquid chromatography-mass spectrometry). Besides proteins, the effect of hydrophobicity on the prevalence of biomolecules such as cholesterol and triglycerides in the PC has also been established with the same copolymer nanoparticles, with lowered hydrophobicity diminishing their levels when measured with enzymatic assays.[203] In agreement with these trends, Su *et al.* found that the hard coronas of their hydrophilic nanoparticles underwent faster protein exchange compared to their hydrophobic counterparts.[202] Their gold nanoparticles, functionalised with set ratios of hydrophilic triethylene glycol and hydrophobic undecane-based ligands showed preferences for different protein types based on their hydrophobic identity. Specifically, antithrombins and vitronectin seemed to be favoured by the more hydrophilic particles, fetal hemoglobin and serum albumin was more common on the hydrophobic particles surface, and prothrombin and talin 1 significantly comprising the intermediately hydrophobic particles' coronas.Considering the current knowledge base on the relationship between nanoparticle hydrophobicity and the features of the final protein corona that forms, we sought to elucidate whether the varied hydrophilic-hydrophobic

balance levels would likewise simulate differences in the MPBs' interactions with proteins and whether this would translate into differences in their in vitro behaviour. This goal was partly motivated by the favourable in vitro outcomes observed in the moderately hydrophobic/hydrophilic particles D20% and D40% against cancer cell models, which we attempt to explain via the findings of this research chapter. To advance our understanding further and potentially explain the favourable in vitro performance of D20% and D40% against cancer cells, we also attempted to discern how the MPBs interactions with cellular membranes might vary in accordance with variable hydrophobicities as well as the presence or absence of a protein corona. As medicinal nanomaterials need to be internalised within cells to deliver their cargo, their interfacial associations with the cell's bilayer lipid membrane represents an important stage that determines their biological activity, including aspects such as cytotoxicity and internalisation efficiency.[204] To date however, the effect of hydrophobicity in unimolecular particles such as MPBs, using random copolymers of hydrophilic/hydrophobic components, has been scarcely studied. Here, we employed the same MPBs synthesised in the previous work and successively examined how the particles underwent physicochemical changes such as size changes using DLS. Afterwards, the MPBs' cell association against A549 cancer cells in the presence and absence of serum proteins was monitored via CLSM and flow cytometry, to determine a possible effect of nanoparticle hydrophobicity on particle-protein associations and how this would subsequently affect their cellular uptake. ITC was then used to narrow down and study the hydrophobicity-dependence of the MPBs affinities with a chosen model protein (bovine serum albumin, BSA). Concurrently, the nanoparticles were also tested against tethered bilayer lipid membranes, which serve as reliable biomimetic models of natural cell membranes. Hence, they served platforms upon which the influence of MPB

hydrophobicity (in conjunction with the absence or presence of proteins) on the membrane-associating behaviour could be probed.

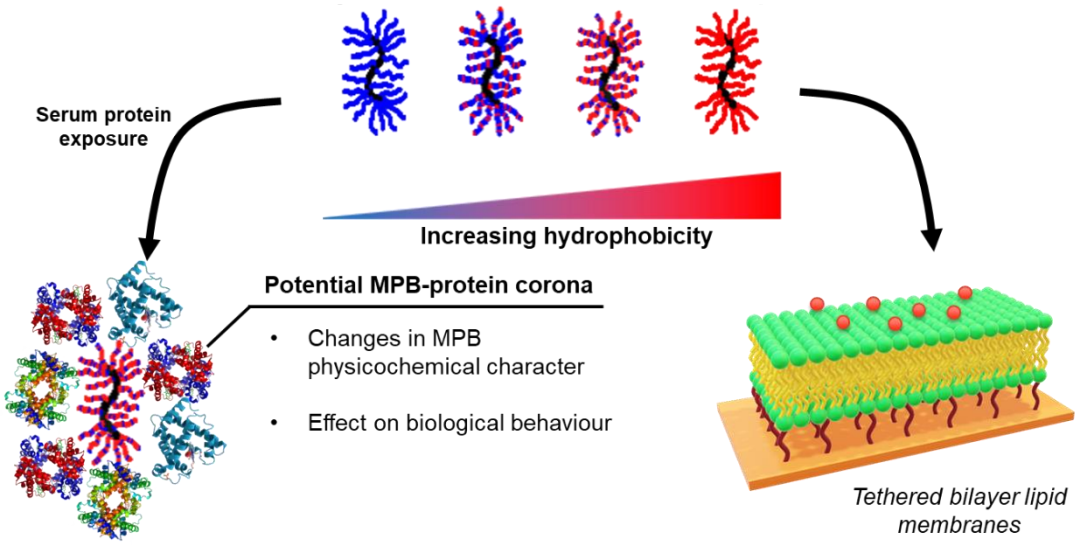

Figure 3.1. Overview of the approach adopted in this research chapter to studying the effects of nanoparticle hydrophobicity on their tumour accumulation and homing behaviour. A series of MPBs bearing different hydrophobicities were used as the test nanoparticle platform, and were successively tested against both in vitro and in vivo tumour models in the form of MCTSs and mouse tumour xenograft models respectively.

3.3. Experimental Section

3.3.1. Materials

2-(dimethylamino) ethyl methacrylate (DMAEMA, 98 %), poly(ethylene glycol) methyl ether methacrylate (PEGMA, 95%, Mn = 300 g mol^{-1}), phosphate buffer saline (PBSx1) tablets, ATTO633-alkyne (in DMSO, 1 mg mL^{-1}), bovine serum albumin (BSA, lyophilised powder) and 1,1,4,7,10,10-hexamethyltriethylenetetramine (HMTETA, 97%)

were purchased from Sigma Aldrich (Australia). Copper(I) chloride (CuCl, ACS grade, Merck) and 1,2-dioleoyl-sn-glycero-3-phosphocholine (DOPC, Avanti Polar Lipids) were sourced from the specified supplier and used as received. Pre-coated gold electrode slides and six-well flow cell cartridges (product code: SDx-T10) and slide assembly clamp and jig (product code: SDx-A1) were obtained from SDx Tethered Membranes (Australia).

Dulbecco's Modified Eagle's Medium (DMEM, with and without phenol red), Dulbecco's phosphate buffered saline (DPBS, no added calcium or magnesium), L-glutamine (200 mM, cell culture supplement), antibiotic-antimycotic solution (100x, containing penicillin and streptomycin), foetal bovine serum (FBS, heat-inactivated) and trypsin-EDTA (0.5%, no phenol red) were purchased from Thermo Fisher Scientific Ltd. A549 cancer cell lines were sourced from Elizabeth New's research group at the School of Chemistry, University of Sydney.

3.3.2. Characterisation Methods

Proton Nuclear Magnetic Resonance (^{1}H NMR): Analyses were carried out on a Bruker Avance 300 spectrometer set at 300 mHz and 300 K. Samples were prepared in deuterated chloroform ($CDCl_3$) or deuterated methanol (MeOD).

Dynamic light scattering (DLS): Analyses of the MPBs' Z-average hydrodynamic diameters (D_H) in the presence/absence of serum proteins were performed on a Malvern Zetasizer Nano ZS equipped with a He-Ne 633 nm laser. Light scattering data was collected at a 173° detection angle after an equilibration time of 180 s. MPB solutions were prepared in PBSx1 ($c = 0.5$ mg mL^{-1}) supplemented with or without FBS (5 % v/v) as necessary.

Isothermal titration calorimetry (ITC): ITC analyses were carried out using a MicroCal Isothermal Titration Calorimeter (ITC200) equipped with a 280 µL sample cell. MPB and BSA samples were prepared by dissolution in PBSx1 (pH 7.4), dialysed over 2 days against PBSx1 to negate buffer mismatch, and degassed using a Thermovac sample degasser (MicroCal) before each experiment. ITC analyses were carried out by sequential injection of solutions of BSA (15 mg mL^{-1}, 227 µM) against MPB solutions (4 mg mL^{-1}, corresponding to 3.6, 3.6, 4.0 and 4.2 µM of D0%, D20%, D40% and D60% respectively) and monitoring the resultant heat changes. Experiments were conducted at 25 °C using an initial delay of 300 s and a starting injection of 0.5 µL. This was followed by 19 successive titrant injections, spaced 2 min apart. A control experiment consisting of BSA titrated into buffer was performed to measure heats of BSA dilution. Final data was processed using the onboard Origin ITC data analysis software. Baseline correction was achieved by subtracting the obtained heat of dilution from the raw heats of BSA-to-MPB titrations.

Tethered bilayer lipid (tBLM) formation: The tBLMs used in this work were assembled on gold electrode slides surface-functionalised with spacers (benzyldisulphide, bis-tetraethylene glycol, 90% of surface) and membrane tethering groups (benzyldisulphide tetraethyleneglycol monophytane, 10% of surface). The gold electrode slide was subsequently attached to a six-well flow cell cartridge, followed by lipid bilayer assembly using the solvent exchange technique as per the supplier's instructions. This technique was performed by aliquoting 8 µL of a DOPC solution (3 mM in ethanol) into each of the six wells in the flow cartridge followed by a 2 min incubation period. Immediately afterwards, each well was flushed with 100 µL of PBSx1 three times to create the tBLMs.

Electrochemical impedance spectroscopy (EIS): EIS measurements were made on each tBLM well using a connected tethaPod reader (SDx Membranes Ltd, Australia) to

characterise the tBLMs before, during and after MPB incubation. An alternating current (AC) mode was used with a 25 mV amplitude and frequency scanning from 0.1 Hz – 2000 Hz. Once tBLM conductance values were stabilised for at least 10 min, aliquots of the MPBs (100 µL, 0.2 mg mL^{-1}) in PBsx1 (supplemented with or without 5 % v/v FBS) were added to each well. Membrane conductance (G_m) from tBLM exposure to the MPBs after predetermined exposure times were quantified as the percentage change relative to each tBLM's initial conductance, according to the following equation;

$$Change\ in\ conductance\ (\%) = 100\ \times \frac{G_m^t - G_m^0}{G_m^0}$$

Where G_m^t denotes the conductance at time *t* (in min) and G_m^0 denotes the tBLM's initial conductance before MPB addition.

Statistical analysis: Statistical tests were performed using GraphPad Prism v8.0 (GraphPad Software) and Origin 8. Data are presented as means ± SEM. One-way analysis of variance (ANOVA) with Tukey's multiple comparison tests were used compare different groups and determine statistical significance (* $p < 0.05$)

3.3.3. Synthetic Methods

Synthesis of cationic MPBs: In a representative procedure used to make C25% (comprising 75% PEGMA and 25% DMAEMA), PBIEM (5 mg, 0.018 mmol equiv. of Br), HMTETA (9.6 µL, 0.018 mmol), PEGMA (790 mg, 2.63 mmol) and DMAEMA (138 mg, 0.88 mmol) were dissolved in anisole (4 mL). The mixture was degassed by three cycles of freeze-pump-thaw. Before the third freeze cycle, copper(I) chloride (1.8 mg, 0.018 mmol) was added to the mixture and the cycle was continued. The mixture was

reacted at 65 °C for 18 h before quenching *via* cooling and exposure to air. Copper was removed by passing the mixture through a silica column. The product was partly purified by two cycles of precipitation and redissolving in cold hexane and anisole respectively. Lastly, the polymer brushes were dissolved in acetone and dialyzed (MWCO = 14 kDa) into acetone for storage. The DP of the sidechains was calculated from conversion as measured by ^{1}H NMR, based on the relative reduction of the vinyl proton signals (ca. 5.5 – 6.5 ppm) in reaction feedstock samples before and after polymerization.

3.3.4. In Vitro and In Vivo Experimental Methods

Monolayer culturing/uptake assay: A549 cancer cell lines were grown in complete Dulbecco's Modified Eagle Medium (DMEM) supplemented with 10 % (v/v) foetal bovine serum (FBS), 1 % (v/v) penicillin/streptomycin and 1 % *L*-glutamine at 37 °C and 5 % CO_2. Cells were monitored for confluence and passaged every 2-3 days with trypsin-EDTA.

A549 monolayers were cultured by pipetting 5 x 10^4 cells each into 35 mm µ-dishes (purchased from DKSH Holding AG) and incubating at 37 °C and 5 % CO_2 in complete DMEM supplemented with 2 % (v/v) FBS for 144 h. Afterwards, old growth media was carefully aspirated, washed with DPBS and replaced with DMEM solutions containing the MPBs (0.2 mg mL^{-1}, 2 mL total) and left to incubate for the appropriate amount of time. For serum protein-dependent cell uptake assays, the MPB solutions were prepared in either DMEM containing no FBS, or DMEM supplemented with FBS (5 % v/v) and subsequently added to the monolayers after old media was removed. The monolayers were left to incubate for a further 4 h afterwards to minimise cell starvation induced by the absence of

FBS. For the energy-dependent internalisation assay, monolayers were incubated with MPB-containing DMEM solutions (supplemented with 5 % v/v FBS) at either 37 °C or 4 °C for 4 h. Monolayer samples were prepared for microscopic analysis by carefully draining the MPB-containing growth media, washing the monolayers twice with PBSx1, and adding 2 mL of DMEM (5 % (v/v) FBS, no phenol red).

Flo**w **cytometry: A549 cells were seeded at a density of 2.5 x 10^4 cells in 12-well plates and cultured for 24 h. Afterwards, old media was removed, and the cells were washed with PBS (100 µL) per well before fresh media (supplemented with or without 5 % FBS as indicated) containing the MPBs (c = 0.2 mg mL^{-1}) was added. The cells were subsequently incubated at 37 °C for 4 h, after which they were washed with PBSx1 (2 x 100 µL) and detached from the surface by addition of trypsin-EDTA (200 µL) and incubation for 3 min. Fresh media (400 µL) subsequently added to the cell suspension to neutralise residual trypsin, after which the cells were centrifuged for 5 min at 300 *x g*. The cell pellet was subsequently resuspended in cold FACS buffer (Dulbecco's PBS supplemented with 2.5 % v/v of FBS, 5 mM EDTA and 0.01 % v/v of sodium azide) until they were used.

A549 cell samples were measured using a BD LSRII flow cytometer. Mean fluorescence intensities (MFI) of treated cells were derived from a population of at least 10,000 cells (n = 3 per sample).

3.4. Results and Discussion

In this chapter, we extended our investigation into the role of amphiphilicity of soft polymeric nanoparticles on their biological activity, namely on how this parameter governs their interactions with serum proteins and cellular membranes. The initial stages of this investigation began with the synthesis of positively charged MPBs. Our justification for their synthesis was to provide analogues of our MPBs bearing cationic charges that could be used as a reference point for the effects of nanoparticle surface charge on membrane/protein interactions. Previous literature work has already established the important role played by nanoparticle surface charge in affecting their biological behaviour. This is especially true for nanoparticles bearing cationic surface charges, which are generally known to be much more cytotoxic towards most cell types on account of their enhanced membrane-disruptive activity.[205–207] The brushes were synthesised in a similar fashion to the earlier amphiphilic MPB series, using ATRP in a grafting-from strategy to copolymerise DMAEMA and PEGMA sidechains from a PBIEM backbone.

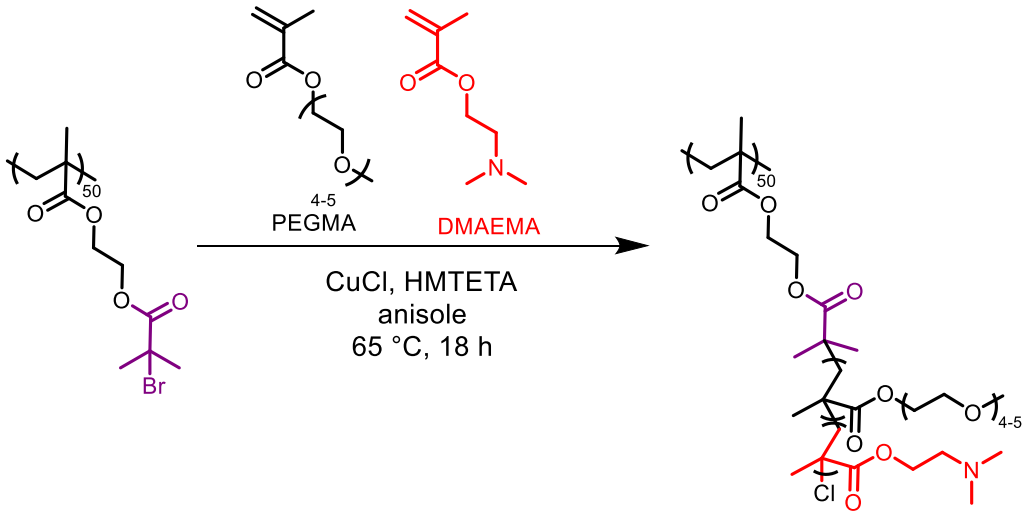

Scheme 3.1. Synthetic route used to prepare the cationic MPBs (C25% and C50%) from PBIEM. The MPBs serve as positive control samples and a reference point due to their posited strong interactions with cellular membranes and serum proteins.

Two different feedstock ratios of the monomers were used, yielding two MPBs with similar side-chain lengths (DP = 120 and 118 for C25% and C50% respectively) and theoretically varied charge densities localised along their sidechains; C25% (bearing 25 % DMAEMA and 75 % PEGMA) and C50% (consisting of 50 % DMAEMA and 50 % PEGMA). At the physiological pH levels used in most of this work, the pKa of the pendant DMAEMA groups (approximately 7.3-7.5) translates to their partial protonation at the physiological pH.[208] Basic characterisation of the cationic MPBs' chemical composition was carried out using ^{1}H NMR (**Figure 3.2**), which confirmed successful incorporation of DMAEMA and PEGMA.

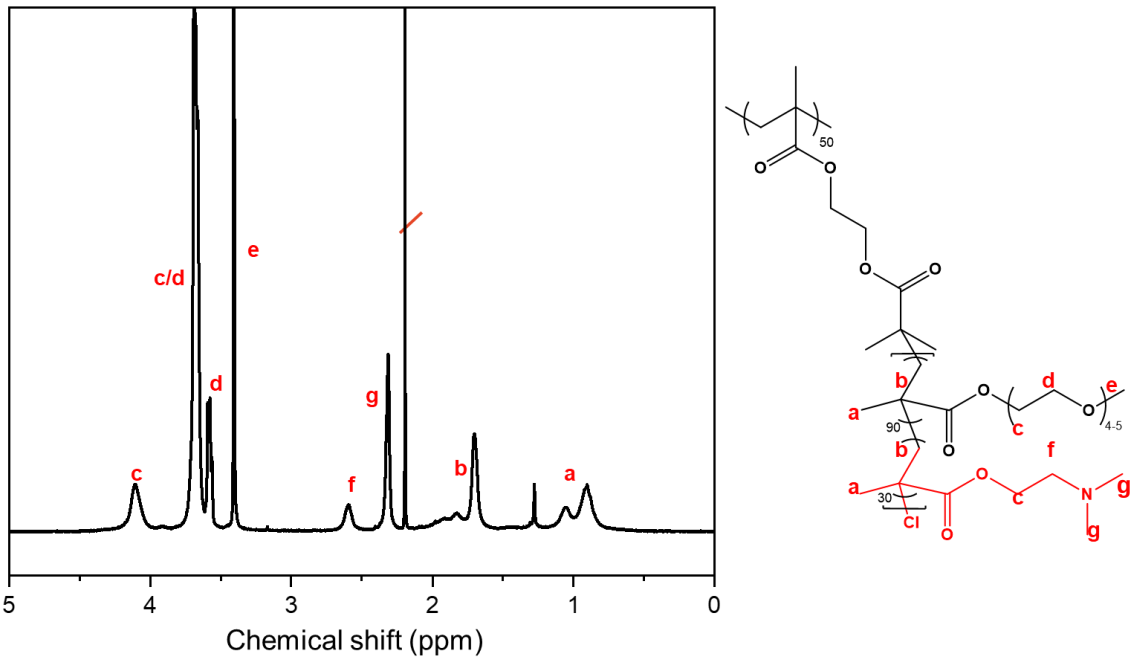

Figure 3.2. ^{1}H NMR spectrum of a representative cationic MPB (C25%) in MeOD.

Once the cationic MPB control samples were synthesised, DLS was subsequently used in a preliminary analysis of the amphiphilic MPBs interaction with foetal bovine serum (FBS), which is normally used as a cell growth supplement in our in vitro experiments. Here, it provides a convenient source of serum proteins with which nanoparticle-protein

interactions can be probed. In this experiment, MPBs were incubated at a temperature of 37 °C in PBSx1 solutions containing FBS (5 % v/v) overnight, before being analysed using DLS to investigate the stability of the MPBs in the presence of serum proteins, as measured by particle size. Discounting D60% on account of its particularly low T_{CP}, D0%, D20% and D40% seemed to exhibit meagre changes in their Z-average hydrodynamic diameters, apart from a broadening of the main peak in the presence of FBS. Considering the R^6 dependency of measured particle size by DLS Interestingly, D60%'s incubation above its T_{CP} in the presence of serum media triggered its aggregation into particulates with mean diameters of 355 nm, much smaller than the polymer-only aggregates formed in the absence of FBS (2752 nm). This is possibly due to the enhanced surface hydrophobicity and consequently high surface energy of the D60% intermolecular aggregates at the test temperature of 37 °C (which is above the MPB's cloud point), in turn facilitating fast protein adsorption onto the aggregates' surface. As the MPB's aggregates' surfaces are stabilised by the protein shell much more readily than those consisting of the polymers alone, the final MPB-protein complexes may have formed more stable aggregates of smaller sizes. Indeed, it is known that hydrophobic nanomaterial surfaces will likewise encourage surrounding proteins to adsorb via their own hydrophobic regions,[209,210] and has been demonstrated upon thermal transitions of LCST-type polymer decorated nanoparticles in their collapsed state.[211,212] Interestingly, in cases such as the poly(2-isopropyl-2-oxazoline) (PiPOx)-coated thermoresponsive nanoparticles used by Bertin *et al.*, size comparisons of the nanoparticles in different serum conditions showed aggregation behaviour that contradicted our observations. Here, thermally-triggered dehydration and collapse of their nanoparticles produced agglomerates of 52 nm in serum-free media, compared to the 510 nm polymer-protein aggregates observed in the presence of proteins.[213] The reason for this apparent trend was laid down to possible destabilisation

of the nanoparticles by the proteins above their T_{CP} by the authors, which goes against our proposed hypothesis of the protein corona as a stabiliser of the highly hydrophobic D60% aggregates.

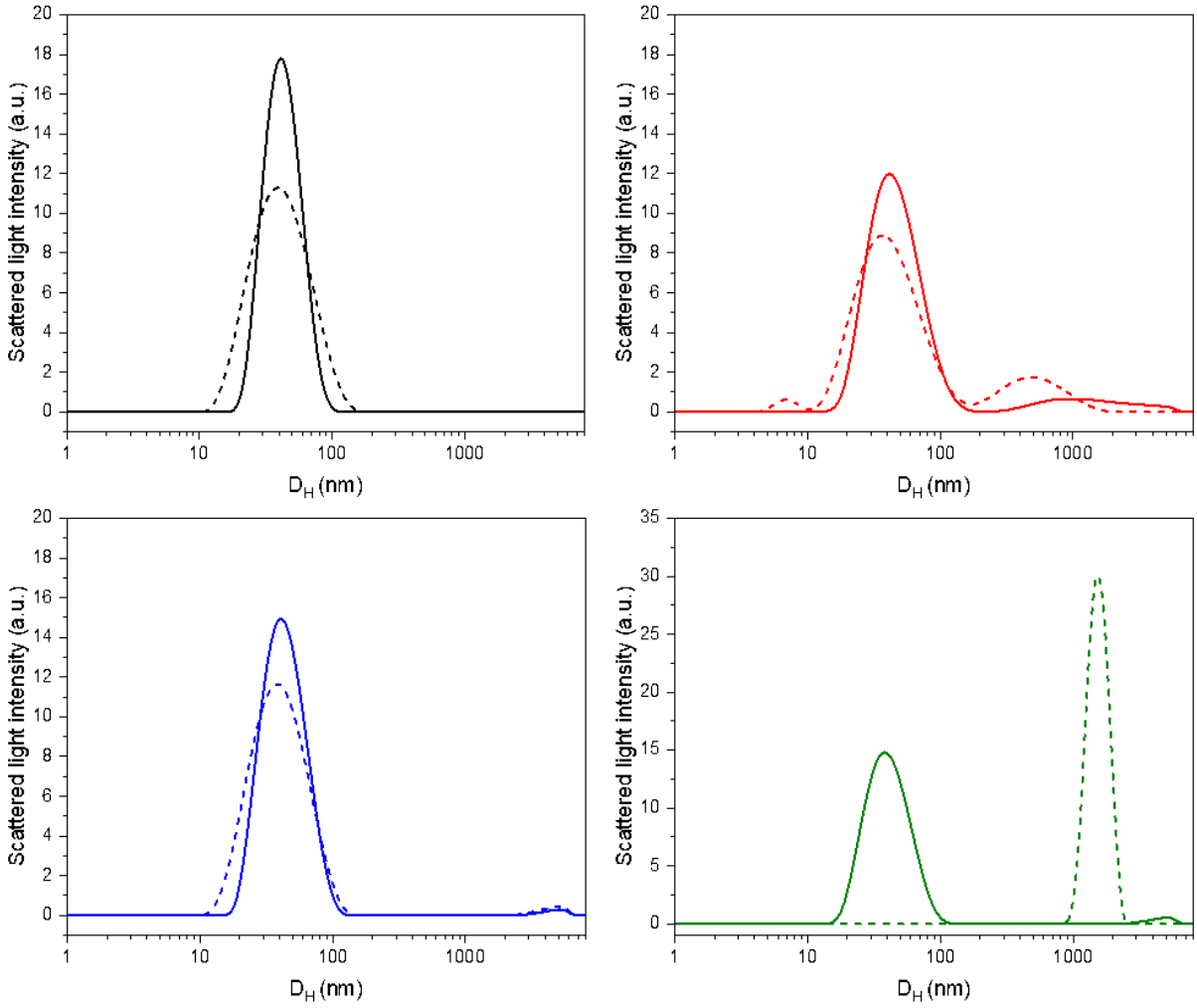

Figure 3.3. Intensity-weighted distributions of the hydrodynamic sizes of the amphiphilic MPBs; D0% (black), D20% (red), D40% (blue) and D60% (green) in PBSx1 (solid) or PBSx1 containing 5% v/v FBS (dashed) at 37 °C.

Table 3.1. Hydrodynamic diameters (D_H) and polydispersities (PDI) of the amphiphilic MPBs measured before and after incubation in FBS-containing PBSx1 (5 % v/v) at 37 °C.

Sample	(-) 5% v/v FBS		(+) 5% v/v FBS	
	D_H (nm)	**PDI**	**D_H (nm)**	**PDI**
D0%	40.0	0.1	44.9	0.2
D20%	45.4	0.31	46.1	0.36
D40%	41.0	0.15	42.6	0.22
D60%	2752	0.5	355.1	0.42

Even with the apparent stability of the hydrophilic MPBs (D0%, D20% and D40%) in the presence of serum, we next sought to observe the potential impact that serum proteins might have on nanoparticle biological interactions onto a cellular scale, as well as its interdependence on the particles' hydrophobicities. To accomplish this, the cellular association of ATTO633-tagged MPBs into A549 cells under serum-present and serum-absent conditions was studied using flow cytometry. Given the importance of FBS as a growth supplement in cell culturing, incubation times with the MPBs were shortened to 6 h to prevent excessive cell starvation and maintain adequate cell viability. As with previous flow cytometry analyses in this work, the MFI values of each MPB was used to correlate total MPB association with the A549 cells. In parallel, 2D A549 cell monolayers were also exposed to the MPBs in serum-free and serum-present conditions, then visualised using CLSM as a qualitative assessment.

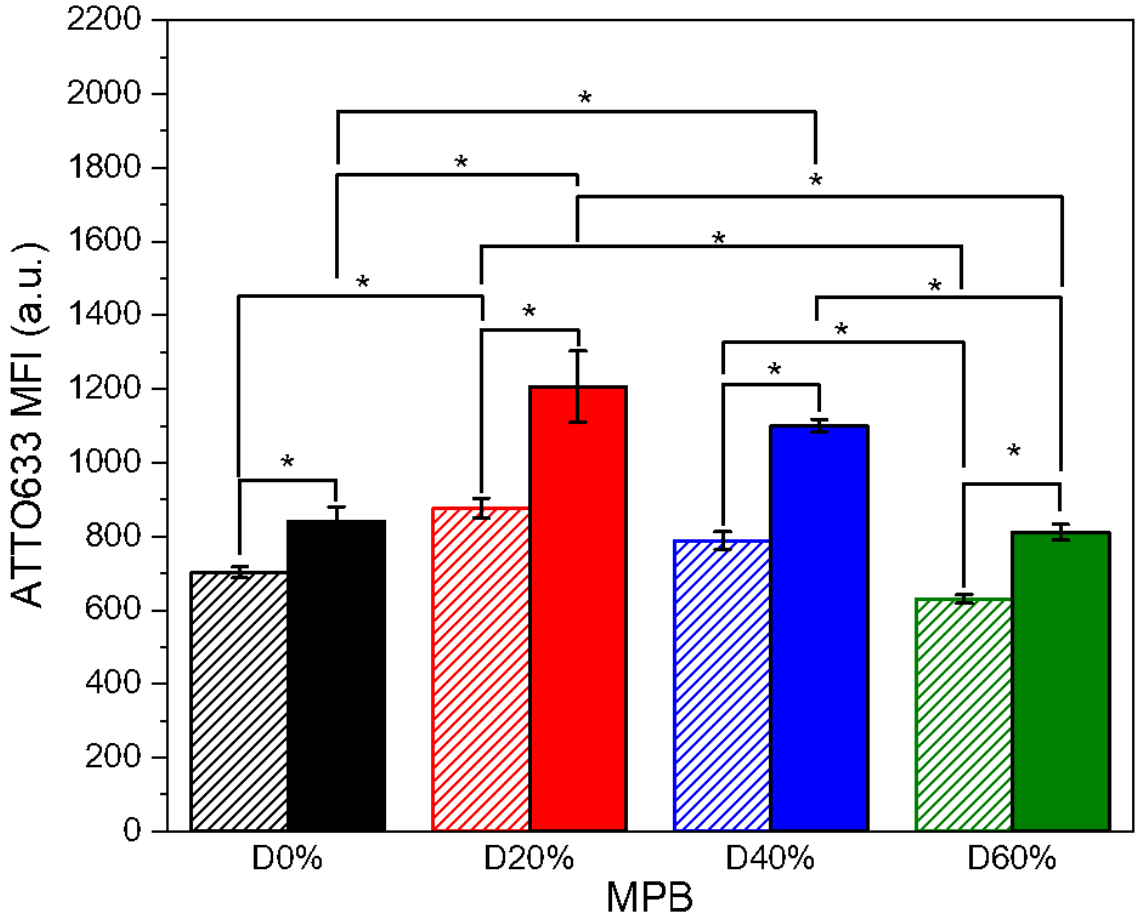

Figure 3.4. MFI values obtained from cytometric analysis of A549 cells incubated with ATTO633-tagged MPBs in FBS-absent (solid columns) or FBS-supplemented (lined columns) cell culture media at 37 °C after 6 h. Data is represented as the mean MFI value with error bars representing the SEM ($n = 3$, $p < 0.05$).

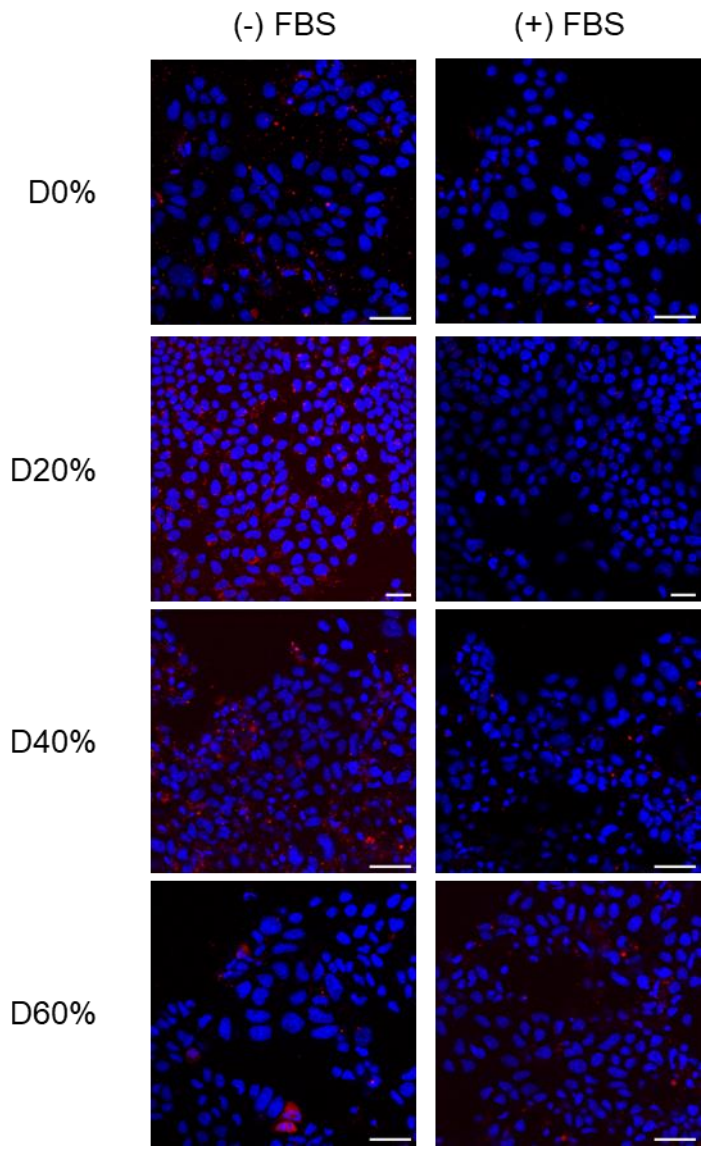

Figure 3.5. CLSM images of A549 cell monolayers after 4 h incubation with ATTO633-tagged MPBs; D0%, D20%, D40% and D60% Monolayers were exposed to MPBs in serum-containing media ((+) FBS), or serum-free medium ((-) FBS)) before being imaged. Images were collected from fluorescence by cell nuclei (blue) or the MPBs (red) and overlaid to produce the images above. Scale bars = 50 μm.

As can be seen from the obtained MFI values and confocal microscopy images under both serum-containing and serum-free environments (**Figure 3.4, Figure 3.5**), differences in nanoparticle hydrophobicity led to differences in cellular association, albeit with the trend

remaining unchanged in both protein conditions. In both cases, the intermediately hydrophobic particles D20% and D40% once again exhibited the greatest uptake into the A549 cells, followed by D0% and lastly D60% as evidenced by flow cytometry. However, a more interesting observation emerges upon comparison of overall MPB uptake between protein-absent and protein-present conditions. When the MPBs were incubated in protein-containing conditions, their uptake into cells was markedly reduced in comparison to conditions where serum proteins were absent. While this set of results seems to negate any potential role of the hydrophilic-hydrophobic balance in regulating nanoparticle cellular uptake, it does qualitatively confirm the importance of the presence of serum proteins in regulating nanoparticle behaviour within complex biological environments, such as their ability to be internalised into cells. A likely explanation for these results can be tied again to changes in the surface energy of the particles when biomolecules such as proteins are introduced. In serum-free conditions, we envision that without proteins potentially adsorbing onto the surface, the MPBs surface energy at the periphery remains high enough to drive sufficiently strong adhesion onto the cellular membrane, thereby increasing their internalisation.[214] By contrast, any proteins that coat the nanoparticle surface could reduce these nonspecific interactions between the MPBs and cellular membrane, thus reducing their uptake. Correlating these findings to similar investigations across the literature proves more difficult than normal, as the presence of protein coronas around a variety of nanoparticles in vitro has shown contradictory findings either boost[215] or worsen[214,216,217] their cellular internalisation depending on various factors such as the material/architecture of the selected nanoparticle, the cell-line used, as well as other variables linked to the selected in vitro experimental conditions. For the interest of this work however, a particular focus on those studies utilising P(OEGMA)- or PEG-decorated nanoparticles to compare uptake in the presence or absence of a protein corona will be discussed further, as they are

compositionally comparable to the PEGMA/DEGMA system used for our MPBs. Summarily, many of these studies observe improved endocytosis of their chosen PEG/OEGMA-based nanoparticles upon incubation in a protein rich matrix, in opposition to our own findings. In a representative example, Onivyde (a liposomal formulation) was used by Carraciolo *et al* to test the effects of PEGylation on cellular uptake with and without a protein corona. They found that when precoated with proteins in human plasma, uptake was boosted compared to unexposed Onivyde in a PANC-1 pancreatic cancer cell line. Similarly, the cellular internalisation of PEG-decorated gold nanoparticles purposed as MRI contrast agents was noticeably augmented when protein coronas were allowed to form on their surface, as shown by O'Toole *et al*.[218] Moreover, this pattern in cellular uptake persisted in nanoparticles of different sizes (4 nm versus 10 nm) and also under different particle exposure times (90 min and 4 h). In factoring in nanoparticle hydrophobicity, only one study to our knowledge has explored the interdependency between this parameter and protein absence/presence on nanoparticle endocytosis efficiency.[155] The findings of this work by showed that silver nanoparticles surface-decorated with two DEGMA-co-PEGMA copolymers of varied molar ratios (5 % and 10 % DEGMA) led to differences in cellular uptake, wherein the more hydrophobic particle experienced a slightly greater uptake in the presence of serum proteins, compared to the hydrophilic particle. Upon incubation in serum-free media however, an intriguing trend was detected in that the more hydrophilic particle was internalised more easily, with a greater difference in uptake compared to its more hydrophobic counterpart. The authors attributed the lowered cellular uptake of the 5% DEGMA-functionalised particles in serum presence due to its' higher hydrophilic PEGMA content, which due to its chemical similarities to PEG, may have compromised its ability to be endocytosed into cells.[219,220] Both of these findings are in stark contrast to uptake patterns observed in this work, and

thus would warrant further investigation, especially as the aforementioned studies all utilise OEGMA-platforms conjugated to inorganic nanoparticle bases, as opposed to the 'soft' unimolecular and completely organic particles used in this work. Hence, a possible interdependency between the chosen nanoparticle's architecture and its hydrophilic-hydrophobic balance could explain these discrepancies.

The cellular uptake results gleaned from flow cytometry and confocal microscopy analyses under different serum conditions underlines the importance of proteins in controlling the biological processes that nanoparticles can intercede in. To investigate further, ITC was used to probe the thermodynamic aspects of interactions between a model serum protein (albumin) and the MPBs. ITC is a highly sensitive technique that lends itself well to the study of nanoparticle interactions with proteins and other biomolecules at the molecular level, with numerous studies already referencing its use in literature. However, as the instrument cannot discriminate between heat changes by different species pairs, as well as limits of currently used binding models, multicomponent mixtures such as FBS cannot be used in conventional analyses. Hence, the choice was made to use BSA (bovine serum albumin) as the model protein, as serum albumin is known to be the most abundant species in blood by concentration,[221] and has been well documented in similar studies investigating the nanoparticle-protein corona.[222,223]

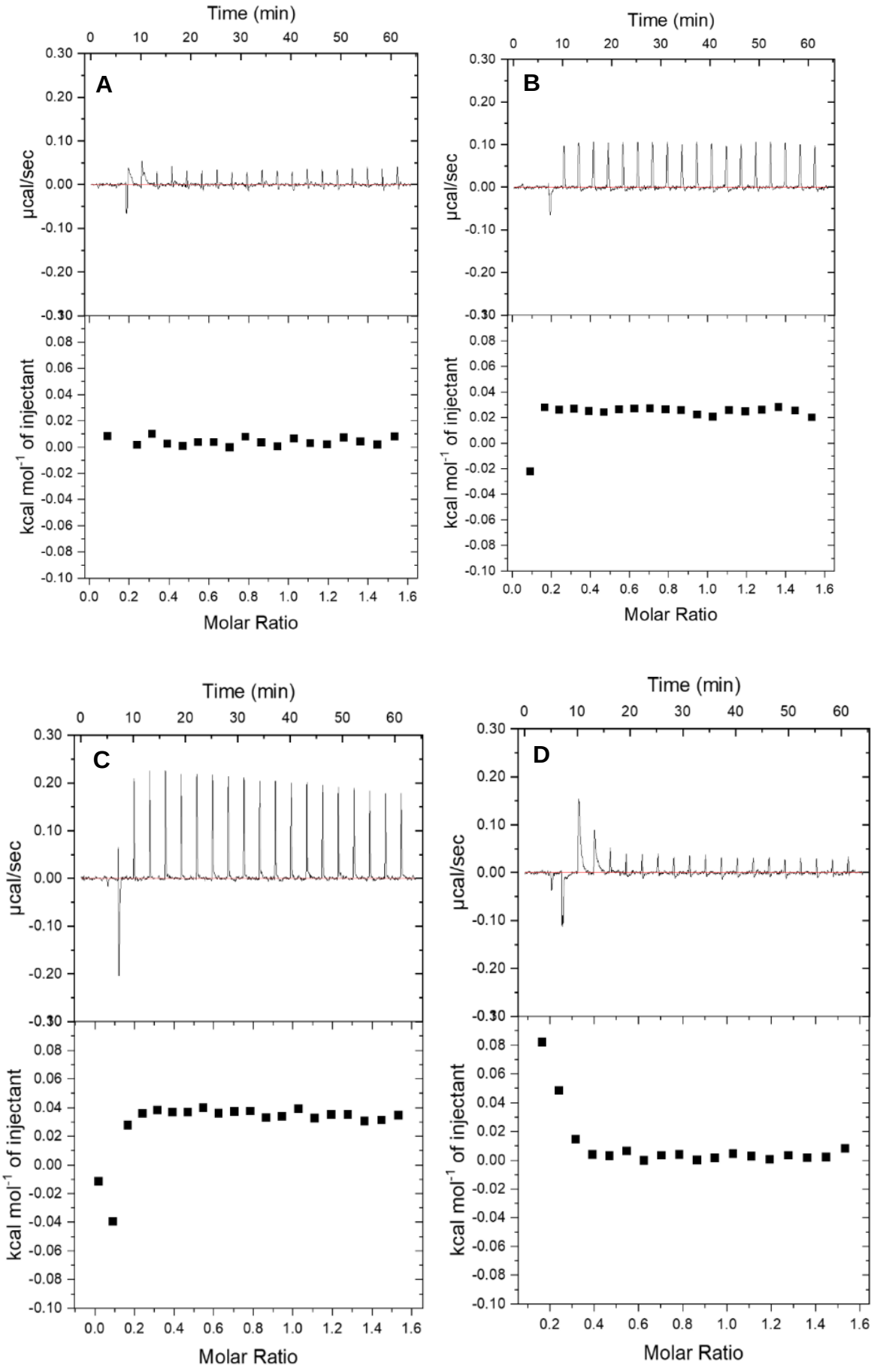
A
B
C
D
Time (min)
µcal/sec
kcal mol-1 of injectant
Molar Ratio

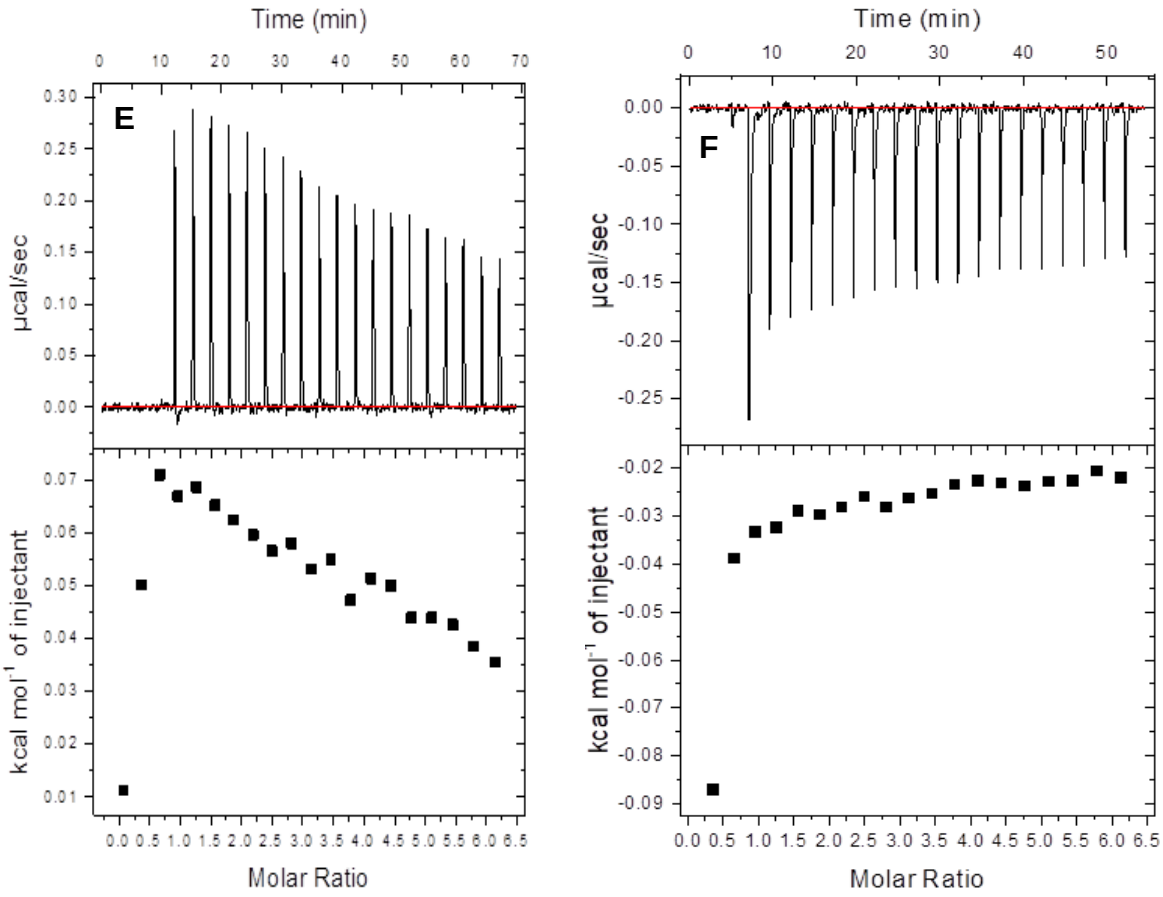

Figure 3.6. ITC thermograms of amphiphilic MPBs; (A) D0%, (B) D20%, (C) D40% and (D) D60% from their titration against BSA. Each thermogram shows raw heat changes measured in µcal per second per injection of BSA (30 mg mL^{-1}) into a solution of MPB (2 mg mL^{-1}) in the top panel. Bottom panels indicate enthalpy changes per injection, measured in kcal per mole of injectant. Heats of dilution were derived from a control experiment involving the injection of BSA at the same concentration titrated into blank buffer (panel E). A positive control experiment was also carried out using the cationic C25% brush (panel F).

As shown in the MPBs' final calorimetric profiles (**Figure 3.6**), injection of BSA into MPB solutions all exhibited positive peaks of small magnitudes, signifying an endothermic process. In this case, the small positive peaks arising from BSA being injected into all the MPB solutions are overshadowed by similar endothermic signals associated with heat

changes from dilution of BSA into pure buffer (**Figure 3.6, E**), indicating that the bottlebrush polymers do not significantly interact with the protein. Because of this lack of significant binding, important thermodynamic parameters such as changes in enthalpy, entropy and association constants cannot be extracted with sufficient confidence. Furthermore, the relative resistance of all the brushes to BSA adsorption seems to indicate that this antifouling behaviour is not significantly affected by each brush's different hydrophobic-hydrophilic balance. It is important to note also that the chosen temperature for these ITC experiments means the MPBs' sidechains exist in their fully extended and hydrated state in the presence of BSA. In this swollen form, P(OEGMA) derivatives are known to possess excellent resistance towards protein adhesion, primarily attributed to their hydrophilic ethylene oxide sidechains that encourages sufficient hydration, in combination with the steric repulsion effect.[224] For that reason, the subtle variations in the hydrophilic-hydrophobic balance levels across the MPB series may not be enough to effect noticeable changes in binding patterns with serum albumin. Indeed, it has been generally observed that below their LCST/T_{CP}, thermosensitive polymer brush-coated nanoparticles provide a largely protein-repellent surface against a variety of proteins such as albumin, lysozyme, fibrinogen and fibronectin and even multi-protein mixtures such as bovine serum.[211,225,226] Hence, regardless of the chemical make-up and varied hydrophobicities of our test MPBs, it seems that the similar hydrated states adopted by all the brushes at $T < T_{CP}$ takes precedence in preventing non-specific interactions with BSA. By contrast, isotherms derived from BSA titration against the positively charged C25% MPBs exhibited highly exothermic signals, indicating strong interactions with the BSA species. This likely arises as a result of the strong electrostatic interactions between the positively charged DMAEMA sidechains and BSA, whose isoelectric point at pH 4.5 – 4.8[227] grants it a negative charge.

Given the importance of the cell membrane as one of the frontiers through which engineered nanomaterials modulate certain biological effects such as cytotoxicity and cellular trafficking routes, we next employed various models and assays to study the possible effects of nanoparticle amphiphilicity on cell membranes. To start, a straightforward MTT assay was used to evaluate the cytotoxicity of the amphiphilic nanoparticles with A549 cells as the chosen cell line. This well-known colorimetric assay relies on the formation of formazan from the reduction of MTT, which can be subsequently solubilised in DMSO and be analysed via UV- Vis spectroscopy to measure its characteristic absorbance at 560 nm. Averaged results taken from triplicate absorbance readings exhibit relative cell biocompatibility (≥ 90%) of all the MPBs at low concentrations (0.1 – 0.25 mg mL^{-1}), although cell viability experienced a greater decline across the MPB series in the 0.5 - 1 mg mL^{-1} concentration range. This confirms that the low MPB concentrations used in previous in vitro experiments will not exert significant cytotoxic effects on the tested cells.

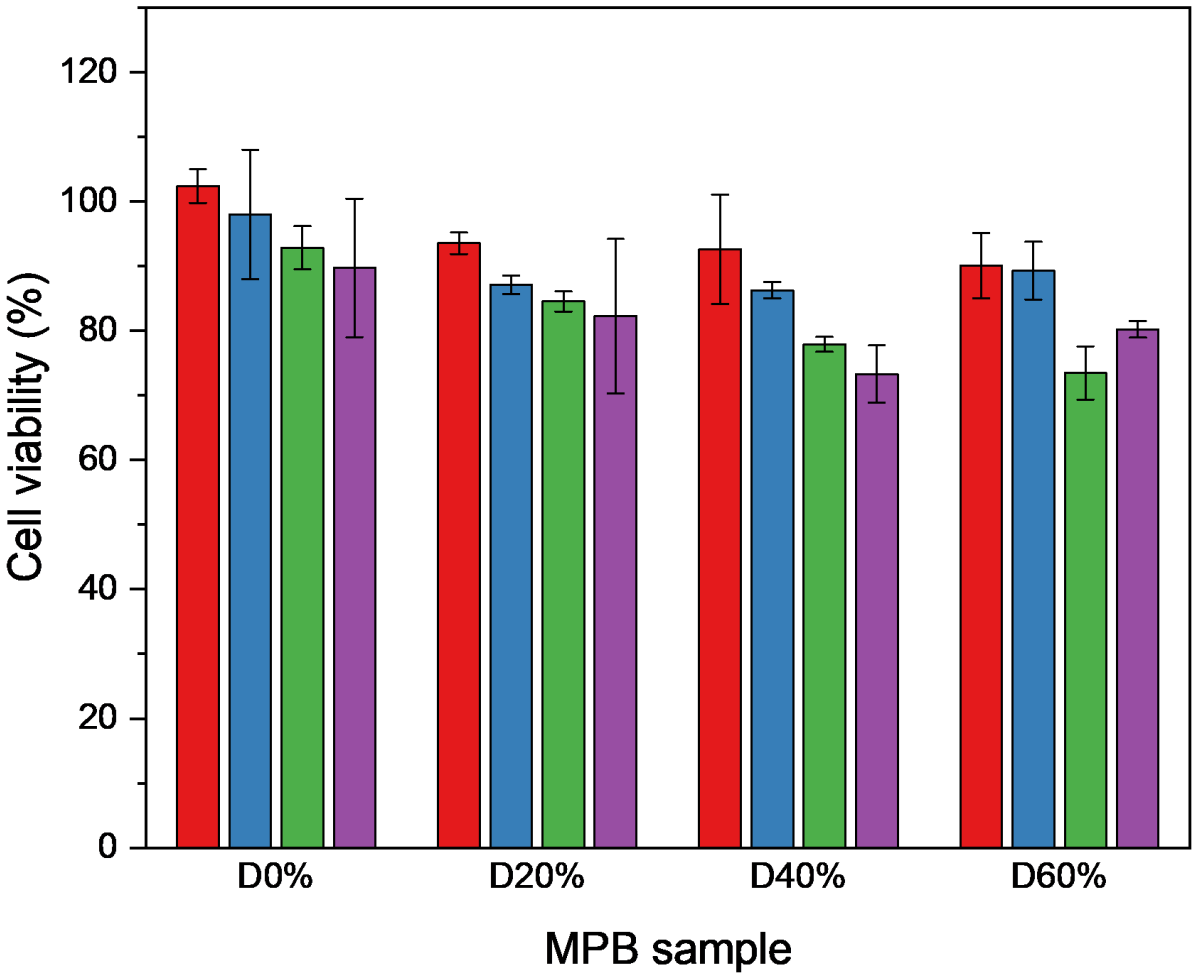

Figure 3.7. Cell viability as measured via the MTT assay of A549 cells when exposed to varying concentrations of the amphiphilic MPBs. The tested concentrations include 0.1 mg mL^{-1} (red bars), 0.25 mg mL^{-1} (blue bars), 0.5 mg mL^{-1} (green bars) and 1 mg mL^{-1} (purple bars). Results are represented as means ± SD (n = 3).

Following cytotoxicity tests of the MPBs, the effect of amphiphilicity was next probed using tBLMs to ascertain how this parameter could induce membrane deformations/defects to differing extents. The tBLM models here are derived from DOPC, a phospholipid commonly used in model membrane studies featuring a zwitterionic head group.[228] As part of this experiment, DOPC bilayer lipid membranes were assembled over tether-functionalised gold electrodes and allowed to incubate in PBSx1 buffer, before

MPB solutions of known concentrations were aliquoted on the membranes and incubated at room temperature for 3 h, with EIS used to monitor the membrane conductance over the given time period. Since the flow of ions is modulated by the extent of phospholipid packing across the membrane,[144] the resulting conductance can be indirectly tied to the membrane's structural integrity as it is subjected to changing conditions (i.e. the adherence and/or penetration of nanoparticles). Changes in phospholipid packing, either poration, perturbation or local gelling, will consequently facilitate or impede transmembrane ion flux, leading to changes in conductance. The final impedance spectra of the amphiphilic MPBs together with the cationic nanoparticle positive controls are visualised in **Figure 3.9**, with the final changes in conductance relative to each membrane's initial conductance reading documented in **Table 3.2.** Before the MPBs were investigated however, electrical impedance measurements were carried out on a concentration series of a representative MPB (D20%). This was done to optimise the concentrations of MPBs used in subsequent experiments, specifically by choosing a concentration that was low enough to prevent osmotic pressure-driven changes to the cell membrane, whilst retaining a high enough polymer presence to effect noticeable changes when incubated onto the tethered bilayers. Four concentrations spanning 10 – 0.2 mg mL^{-1} were used as part of this preliminary run and are represented in **Figure 3.8**. Starting from 10 mg mL^{-1}, the magnitude of conductance increases experienced after 3 h of MPB incubation by the DOPC bilayers fell from 33% (10 mg mL^{-1}), to 24% (1 mg mL^{-1}) and finally to 15% and 14% at 0.5 mg mL^{-1} and 0.2 mg mL^{-1} respectively. As the change in membrane conductance between the latter two concentrations is not significantly different, a final concentration of 0.2 mg mL^{-1} was chosen for future experiments.

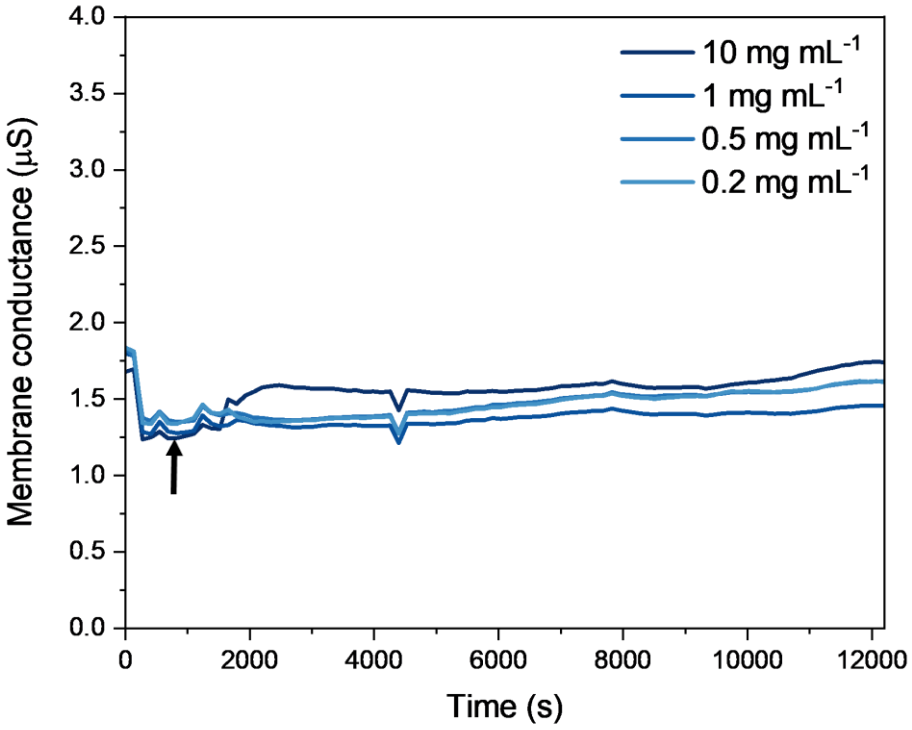

Figure 3.8. Membrane conductance over time of DOPC-based tBLMs after exposure to various concentrations of a representative amphiphilic MPB (D20%). Sample addition to the tBLMs is indicated by the black arrow.

Table 3.2. Quantified changes in conductance of the DOPC tBLMs after 90 min and 180 min of exposure to varying concentrations of a representative amphiphilic MPB (D20%).

Sample concentration (mg mL^{-1})	Conductance change (%)	
	90 min incubation	180 min incubation
10	+21	+33
1	+6.3	+24
0.5	+7.9	+16
0.2	+6.4	+15

At a shorter timescale of 90 min, the tethered membranes exposed to D0%, D20% and D40% all experienced a small rise in conductance with similar magnitudes (+8.5 to +8.7 %, **Figure 3.9, Table 3.3**). The resultant increase indicates slight perturbations of the membrane induced by the nanoparticles, which furthermore could not be reversed upon washing the tBLMs after the allocated exposure time, thus implying the nanoparticles are adhered well to the membrane. However, the similar extent to which membrane disruption occurs signifies a negligible level of influence of nanoparticle amphiphilicity on nanoparticle-membrane associations, at least in the amphiphilicity range represented by D0% - D40%. A curious result is observed in the case of D60%, which by contrast induced an overall decrease in conductance, as opposed to an increase. This can be construed as evidence for local gelling of the phospholipids in a more confined space, thus blocking ion transport. True to expectations, both C25% and C50% induced drastic destabilisation of the membrane, with conductance increase ranging from 29 % for C25% and 121 % for C50% after a 3 h incubation, which we attribute to the strong electrostatic bonding that forms between the positively charged DMAEMA moieties and the phosphorylcholine groups of DOPC. The fact that these experiments were conducted at room temperature means that the nanoparticle-induced stiffening of the membrane by D60% cannot be attributed to its thermosensitive collapse and aggregation alone. This would therefore warrant further investigation, as beyond a certain point, amphiphilicity seems to influence nanoparticle behaviour and deformation of the cell membrane. Nonetheless, since the particles are exposed to the tBLM in their swollen, hydrated forms with extended chains, the negligible membrane disruption of the MPBs is to be somewhat expected, given that nanoparticles bearing non-ionic, hydrophilic polymer brush surfaces (analogous to the MPBs) typically trigger insignificant destabilisation of the bilayer.[145,205] Unfortunately, systematic investigations into the membrane-penetration ability of nanoparticles as

mediated by their hydrophobicity has mostly been limited to computational studies[229,230] or involves comparison of nanoparticles co-opting charged surface functionalities alongside hydrophilic/hydrophobic elements, which therefore complicate analysis of membrane effects on the basis of hydrophobicity alone.[231,232] However, it has been noted that in block poly(ethylene glycol-co-propylene oxide) polymer chains, their efficiency in membrane translocation was dependent on achieving a certain balance between the hydrophobic propylene oxide lengths and the hydrophilic polyethylene oxide block. While more hydrophobic polymers enabled them to easily penetrate and embed themselves within the membrane, they could not efficiently translocate across to the other side. Conversely, the extremely hydrophilic test polymers were able to comfortably adhere onto the membrane surface, but were hampered in their membrane-embedding activity.[233]

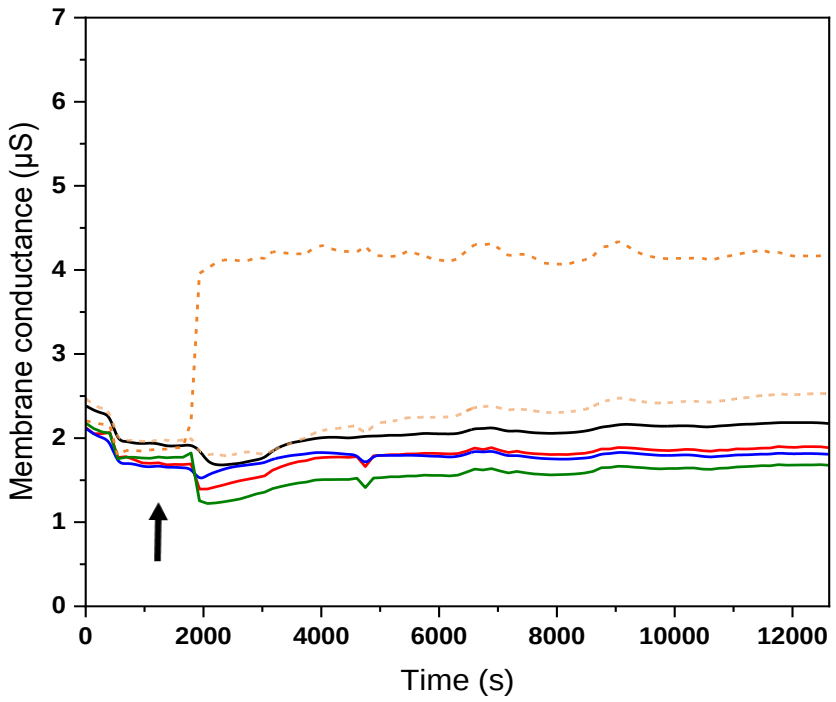

Figure 3.9. Membrane conductance of DOPC tBLMs measured over time after exposure to the amphiphilic MPBs in PBSx1; D0% (black), D20% (red), D40% (blue) and D60% (green). In addition, C25% (light orange, dashed) and C50% (dark orange, dashed) were tested as positively charged control nanoparticles. Sample addition to the tBLMs is indicated by the black arrow.

Table 3.3. Quantified changes in conductance of the DOPC tBLMs after 90 min and 180 min of exposure to the amphiphilic and cationic MPBs

Sample	Conductance change (%)	
	90 min incubation	180 min incubation
D0%	+8.7	+14
D20%	+8.5	+13
D40%	+8.5	+10
D60%	-11	-5.1
C25%	+18	+29
C50%	+121	+121

In a parallel experiment the EIS measurements were repeated with the MPBs pre-incubated in buffer containing FBS before addition to tBLMs, to evaluate how serum proteins intercede in the interplay between each particle's hydrophobicity and bio membranes. Conductance changes from these experiments are reported in **Table 3.4** and **Figure 3.10**. The most striking difference transitioning to the protein-containing condition is the much stronger destabilisation induced by the MPBs in the presence of serum (ranging from conductance increases of 83 % - 185 % amongst the amphiphilic MPB series).

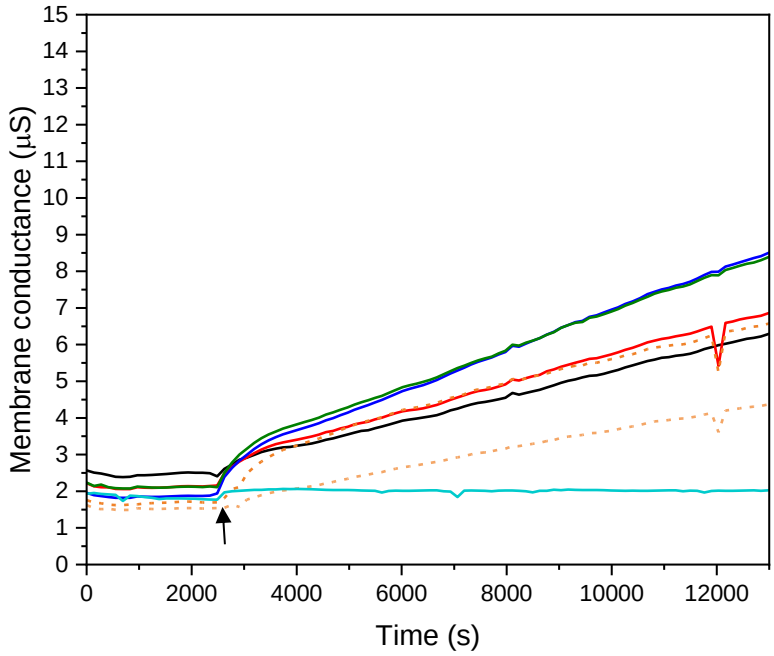

Figure 3.10. Membrane conductance of DOPC tBLMs measured over time after exposure to the amphiphilic MPBs co-incubated with FBS (5 % v/v in PBSx1); D0% (black), D20% (red), D40% (blue) and D60% (green). In addition, C25% (light orange, dashed) and C50% (dark orange, dashed) were tested as cationic control nanoparticles. FBS (5 % v/v in PBSx1) was used as a negative control (teal, solid). Sample addition to the tBLMs is indicated by the black arrow.

Table 3.4. Quantified changes in conductance of the DOPC tBLMs after 90 min and 180 min of exposure to the amphiphilic and cationic MPBs when incubated in PBSx1 supplemented with FBS (5 % v/v).

Sample	Conductance change (%)	
	90 min incubation	180 min incubation
D0%	+83.2	+164
D20%	+119	+221
D40%	+185	+344
D60%	+164	+303
C25%	+97.6	+187
C50%	+181	+290

The perturbation effects of the MPBs on the bilayer membranes in the presence of serum proteins represent a significant change in membrane interaction behaviour compared to the serum-free condition (**Figure 3.10** and **Table 3.4**). Such a result strongly implicates a co-operative mechanism between the MPBs and surrounding proteins that modifies membrane adhesion behaviour, a mechanism that has been previously documented with some nanomaterials.[217,234,235] In one particularly interesting instance, quartz crystal microbalance with dissipation monitoring (QCM-D) and neutron reflectometry (NR) was carried out by Silvio *et al.* to monitor the severity of biomembranes disruption by PS nanoplastics coated with hard/soft coronas.[236] Intriguingly, they reported that the soft corona surrounding the particles induced more severe disruption of the supported lipid bilayers (SLB) tested than particles isolated with the hard corona/ free proteins/particles themselves. These findings are of particular interest to us since the majority of similar studies seem to indicate that protein coronas tend to mitigate particle adhesion to the membrane and subsequently compromise its internalisation efficiency,[217] the opposite of

which is seen here. Another interesting trend observed in our data is an apparent correlation between the particles' increasing hydrophobicity and a corresponding larger disruption of the membrane's structural stability, with D40% achieving the highest magnitude in conductance increase after 90 min (+185 %) and 180 min (+344 %). Curiously, these results Although these differences cannot be explained by FBS alone (which showed a mere increase of 11 % when added on its own), it is nevertheless difficult to separate and pinpoint the membrane-disruptive effects of any potential MPB-protein complexes from that of either free proteins or MPBs. Nonetheless, it is generally accepted that surface hydrophobicity of nanoparticles has considerable effects on specific facets of the protein corona, such as the total amount of proteins adsorbed,[202,213] the specific identities[237,238] or the conformational profiles of the proteins comprising the corona.[239,240] With this in mind, understanding the reasons why the trends thus observed with our tBLM models would require a thorough analysis of these particular aspects of the particles protein corona, to discern how they differ with each particles unique hydrophobicity level.

In the context of serum-free interactions, the negligible effect of amphiphilicity on the particles' translocation efficiency across the DOPC tBLMs indicates that while these OEGMA-based materials can adhere somewhat well at the membrane interface, their endocytosis into cells seems to be an energy-driven process. To confirm this, a simple in vitro experiment involving incubation of DLD-1 monolayers alongside tagged-MPBs was carried out at low (4 °C) or high (37 °C) temperatures and subsequently imaged using CLSM. The obtained results shown in **Figure 3.11** all exhibited diminished cellular association of the MPBs at 4 °C, implicating an energy-dependent endocytic process required for the MPBs to traverse the cell membrane. D60%'s association into the monolayers was consistently low across both tested temperatures. Overall, these in vitro findings are in good agreement with the insubstantial changes to the tBLMs' structural integrity observed across all the MPBs via EIS,

which seem to support the notion that regardless of the hydrophilic-hydrophobic balance, the MPBs cannot efficiently translocate across lipid bilayer membranes passively when in their fully extended, hydrated state.

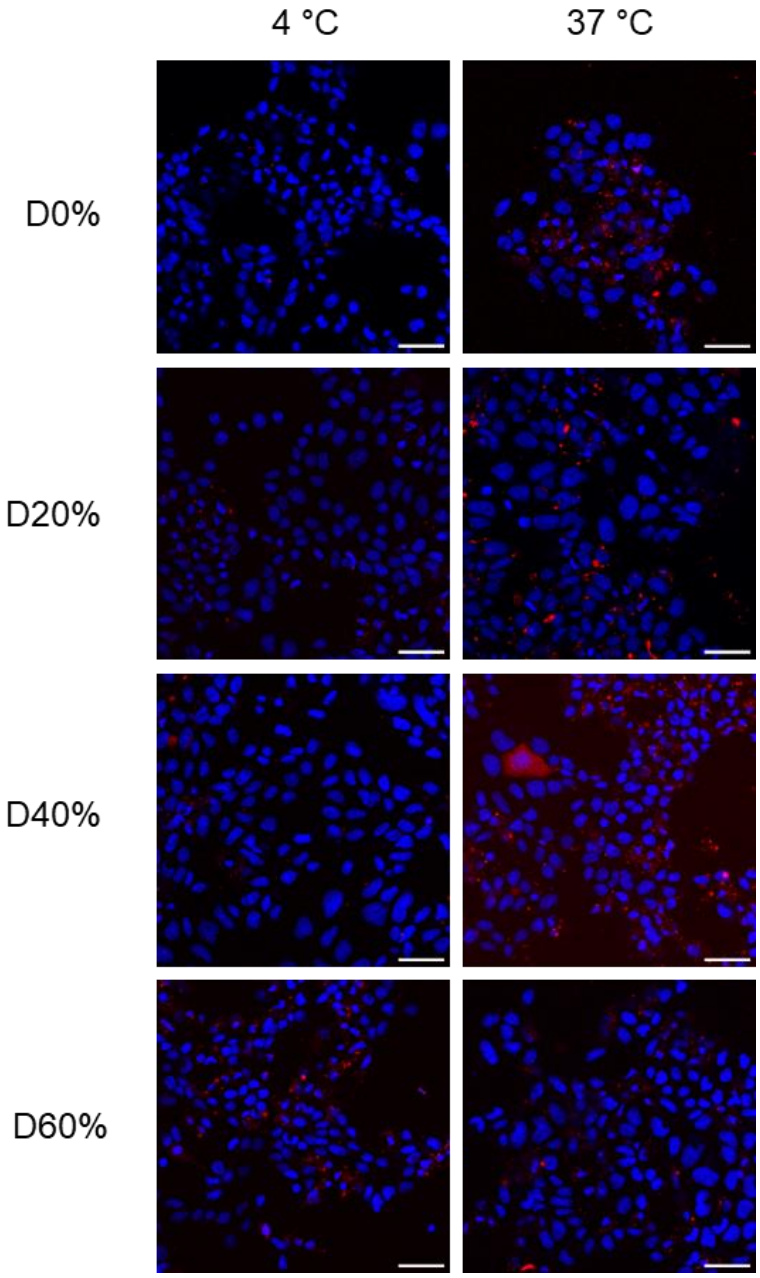

Figure 3.11. CLSM images of DLD-1 cell monolayers after 4 h incubation with ATTO633-tagged MPBs; D0%, D20%, D40% and D60%. Monolayers were incubated at either 4 °C or 37 °C. Images were collected from fluorescence by cell nuclei (blue) or the MPBs (red) and overlaid to produce the images above. Scale bars = 50 µm.

3.5. Conclusions

In this chapter, our work into the amphiphilicity-dependent biological behaviour of MPBs was continued. More specifically, we probed the joint effects of nanoparticle hydrophobicity on their interactions with serum proteins and cellular membranes, and how these interactions in turn affected the particles' behaviour in vitro. In first assessing their affinity for a ubiquitous serum protein (serum albumin), the particles displayed similar 'stealth' properties and general resistance to its adsorption, as measured by ITC, which we attribute to the high hydration of all the MPBs at the temperature chosen for analysis. For potentially the same reason, the bare MPBs also exhibited meagre perturbation effects against DOPC tBLMs serving as model membranes, again showing little difference in that regard based on particle hydrophobicity. However, upon co-incubation in protein-containing serum media, drastic changes manifested in the particles' cellular uptake and membrane-disruptive behaviour, wherein the surrounding proteins hampered uptake in the former and induced more drastic destabilisation in the latter. Moreover, increasing particle hydrophobicity (up to D40%) alongside serum proteins seemed to encourage more severe membrane destabilisation. Although the mechanisms behind the conflicting results between the cell monolayers and model membranes cannot be satisfactorily explained at this stage, the results reinforce the importance of the protein corona as a confounding factor in forecasting how nanoparticles will act in a biological environment when surrounded by co-factors such as proteins.

CHAPTER IV

Conclusions and Future Work

Over the course of this work, RDRP techniques were leveraged to form a series of MPBs featuring systematic variation of their hydrophilic-hydrophobic character. The suitability of these materials in orthogonally screening the biological effects of a chosen physicochemical parameter was proven through the materials' characterisation, showing them to bear different hydrophobicity levels (as evinced by differences in thermoresponsive behaviour) whilst retaining similar hydrodynamic sizes, surface charge and shape. As demonstrated through early in vitro cancer cell models, cellular internalisation of the nanoparticles was improved through an increase in particle hydrophobicity up to a certain limit. CLSM discerned this via increased cellular association in 2D cancer cell monolayers, in addition to more physiologically accurate 3D MCTSs. Strikingly, the impact of varied amphiphilicity also manifested in the MPBs biodistribution behaviour when tested *in vivo* using tumour-bearing mice models. From the initial IV injected dose, a majority fraction of the MPBs were ultimately and predictably sequestered in the MPS organs (liver and spleen), although significant differences in MPS organ accumulations were even observed on the basis of MPB hydrophobicity. More interestingly, an ideal balance of hydrophobicity and hydrophilicity seemed to elicit positive results on the long-term retention of MPBs in the tumour tissue. This was exemplified by the apparent reduction of D0% (i.e. the most hydrophilic particle) from 24 to 48 h, whilst D20% and D40% contrarily experienced an uptick in tissue levels in the same period.

With these elementary results in hand regarding the effect of hydrophobicity/hydrophilicity in governing nanoparticle biodistribution and efficacy in tumour penetration/accumulation, it would be worthwhile studying how this parameter influences other aspects more pertinent to a potential drag carrier system, such as sustained

and controlled drug release. In such future studies, experiments could be devised using a similar MPB scaffold using the same PEGMA/DEGMA copolymer system loaded with a therapeutically active drug cargo in the core. Precedents for such research already exists in the numerous studies employing therapeutic loaded-nanoparticles surface-functionalised with thermosensitive polymers, in order to achieve spatial and temporal control of an active pharmaceutical cargo.[241,242] Apart from enabling fine control over therapeutic cargo release using temperature as a trigger, it has been demonstrated that modifying the hydrophobic/hydrophilic character of the loaded nanoparticle can impact their ability to efficiently encapsulate and discharge small-molecule drugs. For instance, a systematic study carried out by Pietrangelo *et al*. identified the influence of the hydrophobic block's chemical composition in DOX-loaded polymer micelles on their efficacy in drug loading and release. Summarily, by varying the hydrophobicity of the core block using derivatives of acryloyl pyrrolidone with similar molar masses, the assembled micelles experienced improvements in drug loading with more hydrophobic cores, albeit at the cost of impaired drug release even above the micelles' LCST.[243] In a similar investigation, drug-loaded liposomes functionalised with thermosensitive polymers synthesised by Kono *et al.* were used to investigate how drug release was impacted by the polymers' different transition enthalpies (as modulated by the polymer's hydrophobicity). Control over transition enthalpy was accomplished via changing the hydrophobicity of the surface copolymer using different pyrrolidone and acrylamide-based monomers, and the final nanoformulations were synthesised to bear the same LCST (around 40 °C). It was found that the liposomes decorated with the most hydrophobic NIPMAM (N-isopropylmethacrylamide)-containing copolymer bore the largest enthalpy transition and thus formed the most hydrophobic domains upon heating above their LCST, leading to stronger interactions with the underlying liposome. This was found to correlate with

enhanced release of calcein (a model hydrophobic dye) which the authors posited was due to the more drastic changes in the liposome fluidity caused by interactions with the hydrophobic copolymer domains.[244] To date and to our knowledge however, the contributions of nanoparticle hydrophilicity/hydrophobicity on drug encapsulation and release performance in purely polymeric, unimolecular systems such as MPBs has been seldom explored. Previous works have nonetheless ascertained that drug release profiles can vary in nanoparticles affixed with variable PEGMA-co-DEGMA compositions, such as in terms of the temperature range and total percentage of drug load in which release occurs.[245–247] In a more relevant and recent example, the Reineke research group synthesised a series of MPBs with installed end-groups of different hydrophilicity levels. [248] In testing the MPBs propensity to physically encapsulate a moderately hydrophobic anticonvulsant drug (phenytoin), they found the drug's trapping efficiency peaked when entrapped with the most hydrophilic carboxylate-modified MPBs.

The fundamental findings made of the particles' organ and tumour accumulation propelled us to further investigate the potential mechanisms underlying these differences. In the third chapter, we did so by specifically examining how changing the amphiphilicity of the MPBs might effect a change in their interactions with serum components such as proteins. So far however, our work in the third chapter has shown that these MPB amphiphilicity levels had a limited effect on serum protein binding. Nonetheless, significant differences in cellular interactions were observed between MPBs exposed to a protein-rich and a protein-free environment. Specifically, a distinct increase in the MPBs cellular internalisation was noted in the absence of serum proteins that could potentially have formed a corona around the nanoparticles, although high endocytic uptake in D20% and D40% persevered in both serum conditions. As it stands, our limited approach to studying the hydrophobic-

hydrophilic balance of these PEGMA-based MPBs has yielded a fragmented understanding of how they influence PC formation and composition, primarily due to the difficulties in reliably separating potential MPB-PC complexes from surrounding free proteins and MPB particles. The subtle differences in hydrophobicity between the MPBs as modulated by our use of a PEGMA/DEGMA platform, while affording a facile handle for particle hydrophobicity control, showed insignificant differences as a function of hydrophobicity when it came to their binding activity with BSA or their ability to meaningfully induce physical changes to the tBLMs. The likely explanation for this, as noted before, is that the MPBs hydrophobicities only show drastic changes dependent on their LCST/T_{CP}. Hence, while D60%'s lowered T_{CP} meant that its behaviour *in vitro* and *in vivo* predictably differed from the remaining MPBs, the higher T_{CP} values of D0%, D20% and D40% compared to the temperatures used in most of the third chapter's experiments meant that differences in hydrophobicity between these three particles did not manifest strongly enough to be apparent. A more insightful and interesting direction that could be taken in future works is to examine in more detail how parameters such as hydration levels might change between these particles using techniques such as differential scanning calorimetry (DSC). Previously, Tanaka *et al*. have used this technique alongside computational studies to model and experimentally verify differences in the binding states of water molecules with PEG-derivative polymers depending on factors such as the number of EG units present and their spacing along the polymer chain. Furthermore, they correlated the different amounts of water in different solvation states with the platelet adhesion activity of different polymers.[249,250] In that sense, exploring how hydration water molecules behave differently around our PEGMA/DEGMA copolymers may provide an avenue for future differences in protein adsorption onto the different MPBs to be explained.

The extraction of MPB-protein complexes at this point presents a significant challenge that needs to be overcome before more detailed analyses of the protein corona's dependence on the MPBs hydrophobicity can be conducted. In that context, a variety of more specialised methods for PC separation and purification from polymeric nanoparticles have been documented in literature, such as asymmetrical flow field-flow fractionation (AF4).[251,252] This technique achieves species separation by hydrodynamic radii/volume and can be applied to a wide size range of particles (1 nm – 100 µm).[253] In AF4, samples are injected into a channel and subjected to a 'cross-flow' that pushes them towards the permeable membrane lining the channel's opposite edge. As the sample species elutes back towards the centre of the channel *via* Brownian motion, their varying diffusion coefficients (dependent on their hydrodynamic radii) causes smaller particles to diffuse towards the middle of the channel, whilst larger species tend to settle closer to the channel edges.[254] Combined with the parabolic flow profile of the eluent travelling through the channel, the greater speed at the center of the channel causes smaller particles to elute faster than their larger counterparts. Compared to the more ubiquitous techniques of centrifugation and SEC for isolation of nanoparticle-protein complexes, AF4 manages to fulfil the same purpose under much milder conditions, since the analyte is not subjected to harsh shear forces that may prematurely separate or degrade the corona of interest.[255] Reliable isolation of stable MPB-PC complexes from the surrounding medium in this way would drastically facilitate proteomics studies downstream, such as LC-MS or SDS-PAGE-based analyses to determine the corona's composition. The separated MPB-corona complexes could furthermore be tested against our tBLM models used earlier in a more reliable analysis of how the MPBs' hydrophobicity, as bridged by the MPB-protein corona, interacts with mammalian membranes on a molecular level, without the confounding effect of membrane perturbations triggered by sole MPBs or proteins. Koeper *et al*. have already demonstrated

the feasibility of such an approach in their investigation into the membrane-destabilising effects and cytotoxic activity of both bare and protein-coated PS nanoplastics.[256]

Bibliography

(1) Kocarnik, J. M.; Compton, K.; Dean, F. E.; Fu, W.; Gaw, B. L.; Harvey, J. D.; Henrikson, H. J.; Lu, D.; Pennini, A.; Xu, R.; et al. Cancer Incidence, Mortality, Years of Life Lost, Years Lived With Disability, and Disability-Adjusted Life Years for 29 Cancer Groups From 2010 to 2019 A Systematic Analysis for the Global Burden of Disease Study 2019. *JAMA Oncol.* **2022**, *8* (3), 420–444. https://doi.org/10.1001/jamaoncol.2021.6987.

(2) Chen, S.; Cao, Z.; Prettner, K.; Kuhn, M.; Yang, J.; Jiao, L.; Wang, Z.; Li, W.; Geldsetzer, P.; Bärnighausen, T.; Bloom, D. E.; Wang, C. Estimates and Projections of the Global Economic Cost of 29 Cancers in 204 Countries and Territories From 2020 to 2050. *JAMA Oncol.* **2023**, *9* (4), 465–472. https://doi.org/10.1001/JAMAONCOL.2022.7826.

(3) Weinberg, R. A. How Cancer Arises. *Sci. Am.* **1996**, *275* (3), 62–70. https://doi.org/10.1038/scientificamerican0996-61.

(4) Lorscheider, M.; Gaudin, A.; Nakhle, J.; Veiman, K. L.; Richard, J.; Chassaing, C. Challenges and Opportunities in the Delivery of Cancer Therapeutics: Update on Recent Progress. *Ther. Deliv.* **2021**, *12* (1), 55–76. https://doi.org/10.4155/tde-2020-0079.

(5) Manzari, M. T.; Shamay, Y.; Kiguchi, H.; Rosen, N.; Scaltriti, M.; Heller, D. A. Targeted Drug Delivery Strategies for Precision Medicines. *Nat. Rev. Mater.* **2021**, *6* (4), 351–370. https://doi.org/10.1038/s41578-020-00269-6.

(6) Yetisgin, A. A.; Sibel, Cetinel; Merve, Zuvin; Ali, Kosar and Ozlem, K. *Therapeutic Nanoparticles and Their Targeted Delivery Applications*; 2020; Vol. 25.

(7) Cairns, R.; Papandreou, I.; Denko, N. Overcoming Physiologic Barriers to Cancer Treatment by Molecularly Targeting the Tumor Microenvironment. *Mol. Cancer Res.* **2006**, *4* (2), 61–70. https://doi.org/10.1158/1541-7786.MCR-06-0002.

(8) Jang, S. H.; Wientjes, M. G.; Lu, D.; Au, J. L. S. Drug Delivery and Transport to Solid Tumors. *Pharm. Res.* **2003**, *20* (9), 1337–1350. https://doi.org/10.1023/A:1025785505977.

(9) Mansoori, B.; Mohammadi, A.; Davudian, S.; Shirjang, S.; Baradaran, B. The Different

Mechanisms of Cancer Drug Resistance: A Brief Review. *Adv. Pharm. Bull.* **2017**, *7* (3), 339. https://doi.org/10.15171/APB.2017.041.

(10) Shi, J.; Kantoff, P. W.; Wooster, R.; Farokhzad, O. C. Cancer Nanomedicine: Progress, Challenges and Opportunities. *Nat. Rev. Cancer* **2017**, *17* (1), 20–37. https://doi.org/10.1038/nrc.2016.108.

(11) Patra, J. K.; Das, G.; Fraceto, L. F.; Campos, E. V. R.; Rodriguez-Torres, M. D. P.; Acosta-Torres, L. S.; Diaz-Torres, L. A.; Grillo, R.; Swamy, M. K.; Sharma, S.; Habtemariam, S.; Shin, H. S. Nano Based Drug Delivery Systems: Recent Developments and Future Prospects. *J. Nanobiotechnology 2018 161* **2018**, *16* (1), 1–33. https://doi.org/10.1186/S12951-018-0392-8.

(12) Doane, T. L.; Burda, C. The Unique Role of Nanoparticles in Nanomedicine: Imaging, Drug Delivery and Therapy. *Chem. Soc. Rev.* **2012**, *41* (7), 2885. https://doi.org/10.1039/c2cs15260f.

(13) Giri, P. M.; Banerjee, A.; Layek, B. A Recent Review on Cancer Nanomedicine. *Cancers 2023, Vol. 15, Page 2256* **2023**, *15* (8), 2256. https://doi.org/10.3390/CANCERS15082256.

(14) Wang, L.; Xu, H.; Weng, L.; Sun, J.; Jin, Y.; Xiao, C. Activation of Cancer Immunotherapy by Nanomedicine. *Front. Pharmacol.* **2022**, *13*, 5343. https://doi.org/10.3389/FPHAR.2022.1041073/BIBTEX.

(15) Zhao, B.; Chen, S.; Hong, Y.; Jia, L.; Zhou, Y.; He, X.; Wang, Y.; Tian, Z.; Yang, Z.; Gao, D. Research Progress of Conjugated Nanomedicine for Cancer Treatment. *Pharm. 2022, Vol. 14, Page 1522* **2022**, *14* (7), 1522. https://doi.org/10.3390/PHARMACEUTICS14071522.

(16) Shan, X.; Gong, X.; Li, J.; Wen, J.; Li, Y.; Zhang, Z. Current Approaches of Nanomedicines in the Market and Various Stage of Clinical Translation. *Acta Pharm. Sin. B* **2022**, *12* (7), 3028. https://doi.org/10.1016/J.APSB.2022.02.025.

(17) He, H.; Liu, L.; Morin, E. E.; Liu, M.; Schwendeman, A. Survey of Clinical Translation of Cancer Nanomedicines - Lessons Learned from Successes and Failures. *Acc. Chem. Res.* **2019**, *52* (9), 2673–2683. https://doi.org/10.1021/ACS.ACCOUNTS.9B00228/ASSET/IMAGES/LARGE/AR9B

00228_0006.JPEG.

(18) Park, K. Facing the Truth about Nanotechnology in Drug Delivery. *ACS Nano* **2013**, *7* (9), 7442. https://doi.org/10.1021/NN404501G.

(19) Venditto, V. J.; Szoka, F. C. Cancer Nanomedicines: So Many Papers and so Few Drugs! *Adv. Drug Deliv. Rev.* **2013**, *65* (1), 80–88. https://doi.org/10.1016/J.ADDR.2012.09.038.

(20) Cheng, Y. H.; He, C.; Riviere, J. E.; Monteiro-Riviere, N. A.; Lin, Z. Meta-Analysis of Nanoparticle Delivery to Tumors Using a Physiologically Based Pharmacokinetic Modeling and Simulation Approach. *ACS Nano* **2020**, *14* (3), 3075–3095. https://doi.org/10.1021/ACSNANO.9B08142/ASSET/IMAGES/MEDIUM/NN9B08142_M004.GIF.

(21) Milligan, J. J.; Saha, S. A Nanoparticle's Journey to the Tumor: Strategies to Overcome First-Pass Metabolism and Their Limitations. *Cancers (Basel).* **2022**, *14* (7). https://doi.org/10.3390/CANCERS14071741.

(22) Drummond, D. C.; Meyer, O.; Hong, K.; Kirpotin, D. B.; Papahadjopoulos, D. Optimizing Liposomes for Delivery of Chemotherapeutic Agents to Solid Tumors. *Pharmacol. Rev.* **1999**, *51* (4), 691–744.

(23) Drozdov, A. S.; Nikitin, P. I.; Rozenberg, J. M. Systematic Review of Cancer Targeting by Nanoparticles Revealed a Global Association between Accumulation in Tumors and Spleen. *Int. J. Mol. Sci.* **2021**, *22* (23). https://doi.org/10.3390/IJMS222313011/S1.

(24) Bae, Y. H.; Park, K. Targeted Drug Delivery to Tumors: Myths, Reality and Possibility. *Journal of Controlled Release*. Elsevier B.V. August 10, 2011, pp 198–205. https://doi.org/10.1016/j.jconrel.2011.06.001.

(25) Nichols, J. W.; Bae, Y. H. Odyssey of a Cancer Nanoparticle: From Injection Site to Site of Action. *Nano Today* **2012**, *7* (6), 606–618. https://doi.org/10.1016/j.nantod.2012.10.010.Odyssey.

(26) Christian, D. A.; Cai, S.; Garbuzenko, O. B.; Harada, T.; Zajac, A. L.; Minko, T.; Discher, D. E. Flexible Filaments for in Vivo Imaging and Delivery: Persistent Circulation of Filomicelles Opens the Dosage Window for Sustained Tumor Shrinkage.

Mol. Pharm. **2009**, *6* (5), 1343–1352. https://doi.org/10.1021/MP900022M.

(27) Kyriakides, T. R.; Raj, A.; Tseng, T. H.; Xiao, H.; Nguyen, R.; Mohammed, F. S.; Halder, S.; Xu, M.; Wu, M. J.; Bao, S.; Sheu, W. C. Biocompatibility of Nanomaterials and Their Immunological Properties. *Biomed. Mater.* **2021**, *16* (4). https://doi.org/10.1088/1748-605X/abe5fa.

(28) Nel, A. E.; Mädler, L.; Velegol, D.; Xia, T.; Hoek, E. M. V.; Somasundaran, P.; Klaessig, F.; Castranova, V.; Thompson, M. Understanding Biophysicochemical Interactions at the Nano-Bio Interface. *Nat. Mater.* **2009**, *8* (7), 543–557. https://doi.org/10.1038/nmat2442.

(29) Alexis, F.; Pridgen, E.; Molnar, L. K.; Farokhzad, O. C. Factors Affecting the Clearance and Biodistribution of Polymeric Nanoparticles. *Mol. Pharm.* **2008**, *5* (4), 505–515. https://doi.org/10.1021/mp800051m.

(30) Mochalova, E. N.; Egorova, E. A.; Komarova, K. S.; Shipunova, V. O.; Khabibullina, N. F.; Nikitin, P. I.; Nikitin, M. P. Comparative Study of Nanoparticle Blood Circulation after Forced Clearance of Own Erythrocytes (Mononuclear Phagocyte System-Cytoblockade) or Administration of Cytotoxic Doxorubicin- or Clodronate-Loaded Liposomes. *Int. J. Mol. Sci.* **2023**, *24* (13), 10623. https://doi.org/10.3390/ijms241310623.

(31) Gustafson, H. H.; Holt-Casper, D.; Grainger, D. W.; Ghandehari, H. Nanoparticle Uptake: The Phagocyte Problem. *Nano Today* **2015**, *10* (4), 487–510. https://doi.org/10.1016/j.nantod.2015.06.006.

(32) Carboni, E. J.; Bognet, B. H.; Bouchillon, G. M.; Kadilak, A. L.; Shor, L. M.; Ward, M. D.; Ma, A. W. K. Direct Tracking of Particles and Quantification of Margination in Blood Flow. *Biophys. J.* **2016**, *111* (7), 1487–1495. https://doi.org/10.1016/j.bpj.2016.08.026.

(33) Huang, D.; Sun, L.; Huang, L.; Chen, Y. Nanodrug Delivery Systems Modulate Tumor Vessels to Increase the Enhanced Permeability and Retention Effect. *J. Pers. Med.* **2021**, *11* (2), 124. https://doi.org/10.3390/jpm11020124.

(34) Danhier, F.; Feron, O.; Préat, V. To Exploit the Tumor Microenvironment: Passive and Active Tumor Targeting of Nanocarriers for Anti-Cancer Drug Delivery. *J. Control.*

Release **2010**, *148* (2), 135–146. https://doi.org/10.1016/j.jconrel.2010.08.027.

(35) Vander Heiden, M. G.; Cantley, L. C.; Thompson, C. B. Understanding the Warburg Effect: The Metabolic Requirements of Cell Proliferation. *Science (80-.).* **2009**, *324* (5930), 1029–1033. https://doi.org/10.1126/science.1160809.

(36) Biscop; Lin; Boxem; Loenhout; Backer; Deben; Dewilde; Smits; Bogaerts. Influence of Cell Type and Culture Medium on Determining Cancer Selectivity of Cold Atmospheric Plasma Treatment. *Cancers (Basel).* **2019**, *11* (9), 1287. https://doi.org/10.3390/cancers11091287.

(37) Trédan, O.; Galmarini, C. M.; Patel, K.; Tannock, I. F. Drug Resistance and the Solid Tumor Microenvironment. *J. Natl. Cancer Inst.* **2007**, *99* (19), 1441–1454. https://doi.org/10.1093/jnci/djm135.

(38) Kataru, R. P.; Ly, C. L.; Shin, J.; Park, H. J.; Baik, J. E.; Rehal, S.; Ortega, S.; Lyden, D.; Mehrara, B. J. Tumor Lymphatic Function Regulates Tumor Inflammatory and Immunosuppressive Microenvironments. *Cancer Immunol. Res.* **2019**, *7* (8), 1345–1358. https://doi.org/10.1158/2326-6066.CIR-18-0337.

(39) Padera, T. P.; Stoll, B. R.; Tooredman, J. B.; Capen, D.; Di Tomaso, E.; Jain, R. K. Cancer Cells Compress Intratumour Vessels. *Nat. 2004 4276976* **2004**, *427* (6976), 695–695. https://doi.org/10.1038/427695a.

(40) Liu, L. J.; Brown, S. L.; Ewing, J. R.; Ala, B. D.; Schneider, K. M.; Schlesinger, M. Estimation of Tumor Interstitial Fluid Pressure (TIFP) Noninvasively. *PLoS One* **2016**, *11* (7), e0140892. https://doi.org/10.1371/JOURNAL.PONE.0140892.

(41) Heldin, C. H.; Rubin, K.; Pietras, K.; Östman, A. High Interstitial Fluid Pressure — an Obstacle in Cancer Therapy. *Nat. Rev. Cancer 2004 410* **2004**, *4* (10), 806–813. https://doi.org/10.1038/nrc1456.

(42) Omidi, Y.; Barar, J. Targeting Tumor Microenvironment: Crossing Tumor Interstitial Fluid by Multifunctional Nanomedicines. *Bioimpacts* **2014**, *4* (2), 55. https://doi.org/10.5681/BI.2014.021.

(43) Gao, Y.; Shi, Y.; Fu, M.; Feng, Y.; Lin, G.; Kong, D.; Jiang, B. Simulation Study of the Effects of Interstitial Fluid Pressure and Blood Flow Velocity on Transvascular

Transport of Nanoparticles in Tumor Microenvironment. *Comput. Methods Programs Biomed.* **2020**, *193*, 105493. https://doi.org/10.1016/j.cmpb.2020.105493.

(44) Baxter, L. T.; Jain, R. K. Transport of Fluid and Macromolecules in Tumors. I. Role of Interstitial Pressure and Convection. *Microvasc. Res.* **1989**, *37* (1), 77–104. https://doi.org/10.1016/0026-2862(89)90074-5.

(45) Dreher, M. R.; Liu, W.; Michelich, C. R.; Dewhirst, M. W.; Yuan, F.; Chilkoti, A. Tumor Vascular Permeability, Accumulation, and Penetration of Macromolecular Drug Carriers. *JNCI J. Natl. Cancer Inst.* **2006**, *98* (5), 335–344. https://doi.org/10.1093/JNCI/DJJ070.

(46) Torosean, S.; Flynn, B.; Axelsson, J.; Gunn, J.; Samkoe, K. S.; Hasan, T.; Doyley, M. M.; Pogue, B. W. Nanoparticle Uptake in Tumors Is Mediated by the Interplay of Vascular and Collagen Density with Interstitial Pressure. *Nanomedicine* **2013**, *9* (2), 151. https://doi.org/10.1016/J.NANO.2012.07.002.

(47) Heine, M.; Freund, B.; Nielsen, P.; Jung, C.; Reimer, R.; Hohenberg, H.; Zangemeister-Wittke, U.; Wester, H. J.; Lüers, G. H.; Schumacher, U. High Interstitial Fluid Pressure Is Associated with Low Tumour Penetration of Diagnostic Monoclonal Antibodies Applied for Molecular Imaging Purposes. *PLoS One* **2012**, *7* (5), e36258. https://doi.org/10.1371/JOURNAL.PONE.0036258.

(48) Ramanujan, S.; Pluen, A.; McKee, T. D.; Brown, E. B.; Boucher, Y.; Jain, R. K. Diffusion and Convection in Collagen Gels: Implications for Transport in the Tumor Interstitium. *Biophys. J.* **2002**, *83* (3), 1650–1660. https://doi.org/10.1016/S0006-3495(02)73933-7.

(49) Stylianopoulos, T.; Poh, M.-Z.; Insin, N.; Bawendi, M. G.; Fukumura, D.; Munn, L. L.; Jain, R. K. Diffusion of Particles in the Extracellular Matrix: The Effect of Repulsive Electrostatic Interactions. *Biophys. J.* **2010**, *99* (5), 1342–1349.

(50) Blanco, E.; Shen, H.; Ferrari, M. Principles of Nanoparticle Design for Overcoming Biological Barriers to Drug Delivery. *Nat. Biotechnol.* **2015**, *33* (9), 941–951. https://doi.org/10.1038/nbt.3330.

(51) Matsumura, Y.; Maeda, H.; Maeda2, H. A New Concept for Macromolecular Therapeutics in Cancer Chemotherapy: Mechanism of Tumoritropic Accumulation of

Proteins and the Antitumor Agent Smancs1. *Cancer Res.* **1986**, *46* (12_Part_1), 6387–6392.

(52) Lee, H.; Shields, A. F.; Siegel, B. A.; Miller, K. D.; Krop, I.; Ma, C. X.; Lorusso, P. M.; Munster, P. N.; Campbell, K.; Gaddy, D. F.; Leonard, S. C.; Geretti, E.; Blocker, S. J.; Kirpotin, D. B.; Moyo, V.; Wickham, T. J.; Hendriks, B. S. 64Cu-MM-302 Positron Emission Tomography Quantifies Variability of Enhanced Permeability and Retention of Nanoparticles in Relation to Treatment Response in Patients with Metastatic Breast Cancer. *Clin. Cancer Res.* **2017**, *23* (15), 4190–4202. https://doi.org/10.1158/1078-0432.CCR-16-3193.

(53) Biancacci, I.; De Lorenzi, F.; Theek, B.; Bai, X.; May, J. N.; Consolino, L.; Baues, M.; Moeckel, D.; Gremse, F.; von Stillfried, S.; El Shafei, A.; Benderski, K.; Azadkhah Shalmani, A.; Wang, A.; Momoh, J.; Peña, Q.; Buhl, E. M.; Buyel, J.; Hennink, W.; Kiessling, F.; Metselaar, J.; Shi, Y.; Lammers, T. Monitoring EPR Effect Dynamics during Nanotaxane Treatment with Theranostic Polymeric Micelles. *Adv. Sci.* **2022**, *9* (10), 2103745. https://doi.org/10.1002/ADVS.202103745.

(54) Danhier, F. To Exploit the Tumor Microenvironment: Since the EPR Effect Fails in the Clinic, What Is the Future of Nanomedicine? *J. Control. Release* **2016**, *244*, 108–121. https://doi.org/10.1016/J.JCONREL.2016.11.015.

(55) Bolkestein, M.; De Blois, E.; Koelewijn, S. J.; Eggermont, A. M. M.; Grosveld, F.; De Jong, M.; Koning, G. A. Investigation of Factors Determining the Enhanced Permeability and Retention Effect in Subcutaneous Xenografts. *J. Nucl. Med.* **2016**, *57* (4), 601–607. https://doi.org/10.2967/JNUMED.115.166173.

(56) de Lázaro, I.; Mooney, D. J. Obstacles and Opportunities in a Forward Vision for Cancer Nanomedicine. *Nat. Mater.* **2021**, *20* (11), 1469–1479.

(57) Zwicke, G. L.; Mansoori, G. A.; Jeffery, C. J. Utilizing the Folate Receptor for Active Targeting of Cancer Nanotherapeutics. *Nano Rev.* **2012**, *3* (1), 18496. https://doi.org/10.3402/NANO.V3I0.18496.

(58) Scaranti, M.; Cojocaru, E.; Banerjee, S.; Banerji, U. Exploiting the Folate Receptor α in Oncology. *Nat. Rev. Clin. Oncol. 2020 176* **2020**, *17* (6), 349–359. https://doi.org/10.1038/s41571-020-0339-5.

(59) Toffoli, G.; Cernigoi, C.; Russo, A.; Gallo, A.; Bagnoli, M.; Boiocchi, M. Overexpression of Folate Binding Protein in Ovarian Cancers. *Int. J. Cancer* **1997**, *74* (2), 193–198. https://doi.org/10.1002/(SICI)1097-0215(19970422)74:2<193::AID-IJC10>3.0.CO;2-F.

(60) Parker, N.; Turk, M. J.; Westrick, E.; Lewis, J. D.; Low, P. S.; Leamon, C. P. Folate Receptor Expression in Carcinomas and Normal Tissues Determined by a Quantitative Radioligand Binding Assay. *Anal. Biochem.* **2005**, *338* (2), 284–293. https://doi.org/10.1016/j.ab.2004.12.026.

(61) Yoo, H. S.; Park, T. G. Folate Receptor Targeted Biodegradable Polymeric Doxorubicin Micelles. *J. Control. Release* **2004**, *96* (2), 273–283. https://doi.org/10.1016/J.JCONREL.2004.02.003.

(62) Xin, H.; Jiang, X.; Gu, J.; Sha, X.; Chen, L.; Law, K.; Chen, Y.; Wang, X.; Jiang, Y.; Fang, X. Angiopep-Conjugated Poly(Ethylene Glycol)-Co-Poly(ε-Caprolactone) Nanoparticles as Dual-Targeting Drug Delivery System for Brain Glioma. *Biomaterials* **2011**, *32* (18), 4293–4305. https://doi.org/10.1016/J.BIOMATERIALS.2011.02.044.

(63) Hoshyar, N.; Gray, S.; Han, H.; Bao, G. The Effect of Nanoparticle Size on in Vivo Pharmacokinetics and Cellular Interaction. *Nanomedicine* **2016**, *11* (6), 673. https://doi.org/10.2217/NNM.16.5.

(64) Mathaes, R.; Winter, G.; Besheer, A.; Engert, J. Influence of Particle Geometry and PEGylation on Phagocytosis of Particulate Carriers. *Int. J. Pharm.* **2014**, *465* (1–2), 159–164. https://doi.org/10.1016/j.ijpharm.2014.02.037.

(65) Müller, K.; Fedosov, D. A.; Gompper, G. Margination of Micro- and Nano-Particles in Blood Flow and Its Effect on Drug Delivery. *Sci. Rep.* **2014**, *4* (1), 4871. https://doi.org/10.1038/srep04871.

(66) Zein, R.; Sharrouf, W.; Selting, K. Physical Properties of Nanoparticles That Result in Improved Cancer Targeting. *J. Oncol.* **2020**, *2020*, 1–16. https://doi.org/10.1155/2020/5194780.

(67) Foroozandeh, P.; Aziz, A. A. Insight into Cellular Uptake and Intracellular Trafficking of Nanoparticles. *Nanoscale Res. Lett.* **2018**, *13*. https://doi.org/10.1186/s11671-018-2728-6.

(68) Albanese, A.; Tang, P. S.; Chan, W. C. W. The Effect of Nanoparticle Size, Shape, and Surface Chemistry on Biological Systems. *Annu. Rev. Biomed. Eng.* **2012**, *14*, 1–16. https://doi.org/10.1146/annurev-bioeng-071811-150124.

(69) Li, Y.; Lian, Y.; Zhang, L. T.; Aldousari, S. M.; Hedia, H. S.; Asiri, S. A.; Liu, W. K. Cell and Nanoparticle Transport in Tumour Microvasculature: The Role of Size, Shape and Surface Functionality of Nanoparticles. *Interface Focus* **2016**, *6* (1). https://doi.org/10.1098/RSFS.2015.0086.

(70) Jain, R. K. Transport of Molecules across Tumor Vasculature. *Cancer Metastasis Rev.* **1987**, *6* (4), 559–593. https://doi.org/10.1007/BF00047468/METRICS.

(71) Gentile, F.; Chiappini, C.; Fine, D.; Bhavane, R. C.; Peluccio, M. S.; Cheng, M. M. C.; Liu, X.; Ferrari, M.; Decuzzi, P. The Effect of Shape on the Margination Dynamics of Non-Neutrally Buoyant Particles in Two-Dimensional Shear Flows. *J. Biomech.* **2008**, *41* (10), 2312–2318. https://doi.org/10.1016/J.JBIOMECH.2008.03.021.

(72) Ye, H.; Shen, Z.; Yu, L.; Wei, M.; Li, Y. Manipulating Nanoparticle Transport within Blood Flow through External Forces: An Exemplar of Mechanics in Nanomedicine. *Proc. R. Soc. A Math. Phys. Eng. Sci.* **2018**, *474* (2211). https://doi.org/10.1098/RSPA.2017.0845.

(73) Geng, Y.; Dalhaimer, P.; Cai, S.; Tsai, R.; Tewari, M.; Minko, T.; Discher, D. E. Shape Effects of Filaments versus Spherical Particles in Flow and Drug Delivery. *Nat. Nanotechnol. 2007 24* **2007**, *2* (4), 249–255. https://doi.org/10.1038/nnano.2007.70.

(74) Kinnear, C.; Moore, T. L.; Rodriguez-Lorenzo, L.; Rothen-Rutishauser, B.; Petri-Fink, A. Form Follows Function: Nanoparticle Shape and Its Implications for Nanomedicine. *Chem. Rev.* **2017**, *117* (17), 11476–11521. https://doi.org/10.1021/acs.chemrev.7b00194.

(75) Müllner, M.; Yang, K.; Kaur, A.; New, E. J. Aspect-Ratio-Dependent Interaction of Molecular Polymer Brushes and Multicellular Tumour Spheroids. *Polym. Chem.* **2018**, *9* (25), 3461–3465. https://doi.org/10.1039/c8py00703a.

(76) Liu, D.; Auguste, D. T. Cancer Targeted Therapeutics: From Molecules to Drug Delivery Vehicles. *J. Control. Release* **2015**, *219*, 632–643. https://doi.org/10.1016/j.jconrel.2015.08.041.

(77) Levchenko, T. S.; Rammohan, R.; Lukyanov, A. N.; Whiteman, K. R.; Torchilin, V. P. Liposome Clearance in Mice: The Effect of a Separate and Combined Presence of Surface Charge and Polymer Coating. *Int. J. Pharm.* **2002**, *240* (1–2), 95–102. https://doi.org/10.1016/S0378-5173(02)00129-1.

(78) Arvizo, R. R.; Miranda, O. R.; Moyano, D. F.; Walden, C. A.; Giri, K.; Bhattacharya, R.; Robertson, J. D.; Rotello, V. M.; Reid, J. M.; Mukherjee, P. Modulating Pharmacokinetics, Tumor Uptake and Biodistribution by Engineered Nanoparticles. *PLoS One* **2011**, *6* (9), e24374. https://doi.org/10.1371/JOURNAL.PONE.0024374.

(79) Wang, H. X.; Zuo, Z. Q.; Du, J. Z.; Wang, Y. C.; Sun, R.; Cao, Z. T.; Ye, X. D.; Wang, J. L.; Leong, K. W.; Wang, J. Surface Charge Critically Affects Tumor Penetration and Therapeutic Efficacy of Cancer Nanomedicines. *Nano Today* **2016**, *11* (2), 133–144. https://doi.org/10.1016/J.NANTOD.2016.04.008.

(80) Chen, Z.; Wang, F.; Zhu, L. The Effects of Hypoxia on Uptake of Positively Charged Nanoparticles by Tumor Cells. *J. Bionanoscience* **2013**, *7* (5), 601–605. https://doi.org/10.1166/JBNS.2013.1177.

(81) Li, Z.; Gao, Y.; Li, W.; Li, Y.; Lv, H.; Zhang, D.; Peng, J.; Cheng, W.; Mei, L.; Chen, H.; Zeng, X. Charge-Reversal Nanomedicines as a Smart Bullet for Deep Tumor Penetration. *Smart Mater. Med.* **2022**, *3*, 243–253. https://doi.org/10.1016/J.SMAIM.2022.01.008.

(82) Chen, X.; Liu, L.; Jiang, C. Charge-Reversal Nanoparticles: Novel Targeted Drug Delivery Carriers. *Acta Pharm. Sin. B* **2016**, *6* (4), 261–267. https://doi.org/10.1016/j.apsb.2016.05.011.

(83) Zhang, P.; Chen, D.; Li, L.; Sun, K. Charge Reversal Nano-Systems for Tumor Therapy. *J. Nanobiotechnology* **2022**, *20* (1), 31. https://doi.org/10.1186/s12951-021-01221-8.

(84) Cedervall, T.; Lynch, I.; Lindman, S.; Berggård, T.; Thulin, E.; Nilsson, H.; Dawson, K. A.; Linse, S. Understanding the Nanoparticle-Protein Corona Using Methods to Quntify Exchange Rates and Affinities of Proteins for Nanoparticles. *Proc. Natl. Acad. Sci. U. S. A.* **2007**, *104* (7), 2050–2055. https://doi.org/10.1073/pnas.0608582104.

(85) Rahman, M.; Laurent, S.; Tawil, N.; Yahia, L.; Mahmoudi, M. Nanoparticle and Protein Corona. **2013**, 21–44. https://doi.org/10.1007/978-3-642-37555-2_2.

(86) Bobo, D.; Robinson, K. J.; Islam, J.; Thurecht, K. J.; Corrie, S. R. Nanoparticle-Based Medicines: A Review of FDA-Approved Materials and Clinical Trials to Date. *Pharm. Res.* **2016**, *33* (10), 2373–2387. https://doi.org/10.1007/S11095-016-1958-5/TABLES/1.

(87) Rodríguez, F.; Caruana, P.; De la Fuente, N.; Español, P.; Gámez, M.; Balart, J.; Llurba, E.; Rovira, R.; Ruiz, R.; Martín-Lorente, C.; Corchero, J. L.; Céspedes, M. V. Nano-Based Approved Pharmaceuticals for Cancer Treatment: Present and Future Challenges. *Biomolecules* **2022**, *12* (6). https://doi.org/10.3390/BIOM12060784/S1.

(88) Folkman, J.; Long, D. M. The Use of Silicone Rubber as a Carrier for Prolonged Drug Therapy. *J. Surg. Res.* **1964**, *4* (3), 139–142. https://doi.org/10.1016/S0022-4804(64)80040-8.

(89) Oerlemans, C.; Bult, W.; Bos, M.; Storm, G.; Nijsen, J. F. W.; Hennink, W. E. Polymeric Micelles in Anticancer Therapy: Targeting, Imaging and Triggered Release. *Pharm. Res. 2010 2712* **2010**, *27* (12), 2569–2589. https://doi.org/10.1007/S11095-010-0233-4.

(90) Vergote, I.; Brize, A.; Lisyanskaya, A. S.; Lichinitser, M. Randomized Phase III Study Comparing Paclical-Carboplatin with Paclitaxel-Carboplatin in Patients with Recurrent Platinum-Sensitive Epithelial Ovarian Cancer. American Society of Clinical Oncology 2015.

(91) Li, R.-J.; Jin, R.; Liu, C.; Cao, X.; Manning, M. L.; Di, X. M.; Przepiorka, D.; Namuswe, F.; Deisseroth, A.; Goldberg, K. B.; Blumenthal, G. M.; Pazdur, R. FDA Approval Summary: Calaspargase Pegol-Mknl For Treatment of Acute Lymphoblastic Leukemia in Children and Young Adults. *Clin. Cancer Res.* **2020**, *26* (2), 328–331. https://doi.org/10.1158/1078-0432.CCR-19-1255.

(92) Patterson, C. M.; Balachander, S. B.; Grant, I.; Pop-Damkov, P.; Kelly, B.; McCoull, W.; Parker, J.; Giannis, M.; Hill, K. J.; Gibbons, F. D.; Hennessy, E. J.; Kemmitt, P.; Harmer, A. R.; Gales, S.; Purbrick, S.; Redmond, S.; Skinner, M.; Graham, L.; Secrist, J. P.; Schuller, A. G.; Wen, S.; Adam, A.; Reimer, C.; Cidado, J.; Wild, M.; Gangl, E.; Fawell, S. E.; Saeh, J.; Davies, B. R.; Owen, D. J.; Ashford, M. B. Design and Optimisation of Dendrimer-Conjugated Bcl-2/XL Inhibitor, AZD0466, with Improved Therapeutic Index for Cancer Therapy. *Commun. Biol.* **2021**, *4* (1), 112. https://doi.org/10.1038/s42003-020-01631-8.

(93) Liechty, W. B.; Peppas, N. A. Expert Opinion: Responsive Polymer Nanoparticles in Cancer Therapy. *Eur. J. Pharm. Biopharm.* **2012**, *80* (2), 241. https://doi.org/10.1016/J.EJPB.2011.08.004.

(94) Xiao, X.; Teng, F.; Shi, C.; Chen, J.; Wu, S.; Wang, B.; Meng, X.; Essiet Imeh, A.; Li, W. Polymeric Nanoparticles—Promising Carriers for Cancer Therapy. *Front. Bioeng. Biotechnol.* **2022**, *10*, 1852. https://doi.org/10.3389/fbioe.2022.1024143.

(95) Mülhaupt, R. Hermann Staudinger and the Origin of Macromolecular Chemistry. *Angew. Chemie - Int. Ed.* **2004**, *43* (9), 1054–1063. https://doi.org/10.1002/anie.200330070.

(96) Ziegler, K.; Holzkamp, E.; Breil, H.; Martin, H. Polymerisation von Äthylen Und Anderen Olefinen. *Angew. Chemie* **1955**, *67* (16), 426.

(97) Ziegler, K.; Holzkamp, E.; Breil, H.; Martin, H. Das Mülheimer Normaldruck-polyäthylen-verfahren. *Angew. Chemie* **1955**, *67* (19-20), 541–547.

(98) Natta, G.; Pino, P.; Corradini, P.; Danusso, F.; Mantica, E.; Mazzanti, G.; Moraglio, G. Crystalline High Polymers of α-Olefins. *J. Am. Chem. Soc.* **1955**, *77* (6), 1708–1710.

(99) Higashimura, T.; Kishiro, O. Possible Formation of Living Polymers of P-Methoxystyrene by Iodine. *Polym. J.* **1977**, *9* (1), 87–93. https://doi.org/10.1295/polymj.9.87.

(100) Szwarc, M.; Levy, M.; Milkovich, R. Polymerization Initiated by Electron Transfer to Monomer. A New Method of Formation of Block Polymers. *J. Am. Chem. Soc.* **1956**, *78* (11), 2656–2657. https://doi.org/10.1021/JA01592A101/ASSET/JA01592A101.FP.PNG_V03.

(101) Grubbs, R. B.; Grubbs, R. H. 50th Anniversary Perspective: Living Polymerization - Emphasizing the Molecule in Macromolecules. *Macromolecules* **2017**, *50* (18), 6979–6997. https://doi.org/10.1021/acs.macromol.7b01440.

(102) Kato, M.; Kamigaito, M.; Sawamoto, M.; Higashimura, T. Polymerization of Methyl Methacrylate with the Carbon Tetrachloride/Dichlorotris-(Triphenylphosphine)Ruthenium(II)/ Methylaluminum Bis(2,6-Di-Tert-Butylphenoxide) Initiating System: Possibility of Living Radical Polymerization.

Macromolecules **1995**, *28* (5), 1721–1723. https://doi.org/10.1021/MA00109A056/ASSET/MA00109A056.FP.PNG_V03.

(103) Wang, J. S.; Matyjaszewski, K. Controlled/“Living” Radical Polymerization. Atom Transfer Radical Polymerization in the Presence of Transition-Metal Complexes. *J. Am. Chem. Soc.* **1995**, *117* (20), 5614–5615. https://doi.org/10.1021/JA00125A035/ASSET/JA00125A035.FP.PNG_V03.

(104) Matyjaszewski, K. Mechanistic and Synthetic Aspects of Atom Transfer Radical Polymerization. *J. Macromol. Sci. - Pure Appl. Chem.* **1997**, *34* (10), 1785–1801. https://doi.org/10.1080/10601329708010308.

(105) Teodorescu, M.; Gaynor, S. G.; Matyjaszewski, K. Halide Anions as Ligands in Iron-Mediated Atom Transfer Radical Polymerization. **2000**. https://doi.org/10.1021/ma991652e.

(106) Chen, Z. H.; Ma, Y.; Wang, X. Y.; Sun, X. L.; Li, J. F.; Zhu, B. H.; Tang, Y. Winning Strategy for Iron-Based ATRP Using in Situ Generated Iodine as a Regulator. *ACS Catal.* **2020**, *10* (23), 14127–14134. https://doi.org/10.1021/ACSCATAL.0C04312/ASSET/IMAGES/MEDIUM/CS0C04312_M003.GIF.

(107) Wang, B.; Zhuang, Y.; Luo, X.; Xu, S.; Zhou, X. Controlled/"living" Radical Polymerization of MMA Catalyzed by Cobaltocene. *Macromolecules* **2003**, *36* (26), 9684–9686. https://doi.org/10.1021/MA035334Y/SUPPL_FILE/MA035334YSI20031114_013315.PDF.

(108) De Roma, A.; Yang, H. J.; Milione, S.; Capacchione, C.; Roviello, G.; Grassi, A. Atom Transfer Radical Polymerization of Methylmethacrylate Mediated by a Naphtyl–Nickel(II) Phosphane Complex. *Inorg. Chem. Commun.* **2011**, *14* (4), 542–544. https://doi.org/10.1016/J.INOCHE.2011.01.019.

(109) Duquesne, E.; Habimana, J.; Degée, P.; Dubois, P. Nickel-Catalyzed Supported ATRP of Methyl Methacrylate Using Cross-Linked Polystyrene Triphenylphosphine as Ligand. *Macromolecules* **2005**, *38* (24), 9999–10006. https://doi.org/10.1021/MA051413T/ASSET/IMAGES/LARGE/MA051413TF00005.J

PEG.

(110) Afonso, M. B. A.; Cruz, T. R.; Silva, Y. F.; Pereira, J. C. A.; Machado, A. E. H.; Goi, B. E.; Lima-Neto, B. S.; Carvalho-Jr, V. P. Ruthenium(II) Complexes of Schiff Base Derived from Cycloalkylamines as Pre-Catalysts for ROMP of Norbornene and ATRP of Methyl Methacrylate. *J. Organomet. Chem.* **2017**, *851*, 225–234. https://doi.org/10.1016/J.JORGANCHEM.2017.09.043.

(111) Simal, F.; Demonceau, A.; Noels, A. F. Highly Efficient Ruthenium-Based Catalytic Systems for the Controlled Free-Radical Polymerization of Vinyl Monomers**. *Angew. Chem. Int. Ed* **1999**, *38* (4). https://doi.org/10.1002/(SICI)1521-3773(19990215)38:4.

(112) Grishin, I. D.; Zueva, E. I.; Pronina, Y. S.; Grishin, D. F. Novel Copper-Based Catalytic Systems for Atom Transfer Radical Polymerization of Acrylonitrile. *Catal. 2023, Vol. 13, Page 444* **2023**, *13* (2), 444. https://doi.org/10.3390/CATAL13020444.

(113) Tang, H.; Arulsamy, N.; Radosz, M.; Shen, Y.; Tsarevsky, N. V.; Braunecker, W. A.; Tang, W.; Matyjaszewski, K. Highly Active Copper-Based Catalyst for Atom Transfer Radical Polymerization. *J. Am. Chem. Soc.* **2006**, *128* (50), 16277–16285. https://doi.org/10.1021/JA0653369/SUPPL_FILE/JA0653369SI20060809_121938.CIF.

(114) Ding, M.; Jiang, X.; Zhang, L.; Cheng, Z.; Zhu Q Ding, X. M.; Jiang, X. W.; Zhang, L. F.; Cheng, Z. P.; Zhu, X. L. Recent Progress on Transition Metal Catalyst Separation and Recycling in ATRP. *Macromol. Rapid Commun.* **2015**, *36* (19), 1702–1721. https://doi.org/10.1002/MARC.201500085.

(115) Matyjaszewski, K.; Hongchen, D.; Jakubowski, W.; Pietrasik, J.; Kusumo, A. Grafting from Surfaces for "Everyone": ARGET ATRP in the Presence of Air. *Langmuir* **2007**, *23* (8), 4528–4531. https://doi.org/10.1021/LA063402E/ASSET/IMAGES/LARGE/LA063402EF00003.JPEG.

(116) Magenau, A. J. D.; Strandwitz, N. C.; Gennaro, A.; Matyjaszewski, K. Electrochemically Mediated Atom Transfer Radical Polymerization. *Science (80-.).* **2011**, *332* (6025), 81–84. https://doi.org/10.1126/SCIENCE.1202357/SUPPL_FILE/MAGENAU_SOM.PDF.

(117) Matyjaszewski, K.; Jakubowski, W.; Min, K.; Tang, W.; Huang, J.; Braunecker, W. A.; Tsarevsky, N. V. Diminishing Catalyst Concentration in Atom Transfer Radical Polymerization with Reducing Agents. *Proc. Natl. Acad. Sci.* **2006**, *103* (42), 15309–15314. https://doi.org/10.1073/pnas.0602675103.

(118) Chmielarz, P.; Fantin, M.; Park, S.; Isse, A. A.; Gennaro, A.; Magenau, A. J. D.; Sobkowiak, A.; Matyjaszewski, K. Electrochemically Mediated Atom Transfer Radical Polymerization (EATRP). *Prog. Polym. Sci.* **2017**, *69*, 47–78. https://doi.org/10.1016/j.progpolymsci.2017.02.005.

(119) Allison-Logan, S.; Karimi, F.; Sun, Y.; McKenzie, T. G.; Nothling, M. D.; Bryant, G.; Qiao, G. G. Highly Living Stars via Core-First Photo-RAFT Polymerization: Exploitation for Ultra-High Molecular Weight Star Synthesis. *ACS Macro Lett.* **2019**, *8* (10), 1291–1295. https://doi.org/10.1021/acsmacrolett.9b00643.

(120) Shanmugam, S.; Cuthbert, J.; Kowalewski, T.; Boyer, C.; Matyjaszewski, K. Catalyst-Free Selective Photoactivation of RAFT Polymerization: A Facile Route for Preparation of Comblike and Bottlebrush Polymers. *Macromolecules* **2018**, *51* (19), 7776–7784. https://doi.org/10.1021/acs.macromol.8b01708.

(121) Guo, Y.; Zhang, J.; Xie, P.; Gao, X.; Luo, Y. Tailor-Made Compositional Gradient Copolymer by a Many-Shot RAFT Emulsion Polymerization Method. *Polym. Chem.* **2014**, *5* (10), 3363–3371. https://doi.org/10.1039/C4PY00003J.

(122) Guo, X.; Zhang, T.; Wu, Y.; Shi, W.; Choi, B.; Feng, A.; Thang, S. H. Synthesis of CO 2 -Responsive Gradient Copolymers by Switchable RAFT Polymerization and Their Controlled Self-Assembly. *Polym. Chem.* **2020**, *11* (42), 6794–6802. https://doi.org/10.1039/D0PY01109F.

(123) Chiefari, J.; Chong, Y. K.; Ercole, F.; Krstina, J.; Jeffery, J.; Le, T. P. T.; Mayadunne, R. T. A.; Meijs, G. F.; Moad, C. L.; Moad, G.; Rizzardo, E.; Thang, S. H. Living Free-Radical Polymerization by Reversible Addition - Fragmentation Chain Transfer: The RAFT Process. *Macromolecules* **1998**, *31* (16), 5559–5562. https://doi.org/10.1021/MA9804951/ASSET/IMAGES/LARGE/MA9804951F00003.JPEG.

(124) Tsukahara, Y.; Mizuno, K.; Segawa, A.; Yamashita, Y. Study on the Radical

Polymerization Behavior of Macromonomers. *Macromolecules* **1989**, *22* (4), 1546–1552. https://doi.org/10.1021/MA00194A007/ASSET/MA00194A007.FP.PNG_V03.

(125) Djalali, R.; Li, S. Y.; Schmidt, M. Amphipolar Core-Shell Cylindrical Brushes as Templates for the Formation of Gold Clusters and Nanowires. *Macromolecules* **2002**, *35* (11), 4282–4288. https://doi.org/10.1021/MA0113733/ASSET/IMAGES/LARGE/MA0113733F00009.JPEG.

(126) Durmaz, H.; Dag, A.; Cerit, N.; Sirkecioglu, O.; Hizal, G.; Tunca, U. Graft Copolymers via ROMP and Diels–Alder Click Reaction Strategy. *J. Polym. Sci. Part A Polym. Chem.* **2010**, *48* (24), 5982–5991.

(127) Xiao, L.; Chen, Y.; Zhang, K. Efficient Metal-Free "Grafting onto" Method for Bottlebrush Polymers by Combining RAFT and Triazolinedione-Diene Click Reaction. *Macromolecules* **2016**, *49* (12), 4452–4461. https://doi.org/10.1021/ACS.MACROMOL.6B00782/ASSET/IMAGES/LARGE/MA-2016-00782G_0003.JPEG.

(128) Sprafke, J. K.; Spruell, J. M.; Mattson, K. M.; Montarnal, D.; McGrath, A. J.; Pötzsch, R.; Miyajima, D.; Hu, J.; Latimer, A. A.; Voit, B. I.; Aida, T.; Hawker, C. J. Revisiting Thiol-Yne Chemistry: Selective and Efficient Monoaddition for Block and Graft Copolymer Formation. *J. Polym. Sci. Part A Polym. Chem.* **2015**, *53* (2), 319–326. https://doi.org/10.1002/POLA.27345.

(129) Ma, H.; Ha, S.; Jeong, J.; Wang, V.; Kim, K. T. Synthesis of Discrete Bottlebrush Polymers via the Iterative Convergent Growth Technique and Post-Functionalization. *Polym. Chem.* **2022**, *13* (24), 3689–3695. https://doi.org/10.1039/D2PY00573E.

(130) Cesana, S.; Kurek, A.; Baur, M. A.; Auernheimer, J.; Nuyken, O. Polymer-Bound Thiol Groups on Poly(2-Oxazoline)S. *Macromol. Rapid Commun.* **2007**, *28* (5), 608–615. https://doi.org/10.1002/MARC.200600737.

(131) Müllner, M. Molecular Polymer Bottlebrushes in Nanomedicine: Therapeutic and Diagnostic Applications. *Chem. Commun.* **2022**, *58* (38), 5683–5716. https://doi.org/10.1039/D2CC01601J.

(132) Bai, S.; Jia, D.; Ma, X.; Liang, M.; Xue, P.; Kang, Y.; Xu, Z. Cylindrical Polymer

Brushes-Anisotropic Unimolecular Micelle Drug Delivery System for Enhancing the Effectiveness of Chemotherapy. *Bioact. Mater.* **2021**, *6* (9), 2894–2904. https://doi.org/10.1016/j.bioactmat.2021.02.011.

(133) Guo, J.; Hong, H.; Chen, G.; Shi, S.; Nayak, T. R.; Theuer, C. P.; Barnhart, T. E.; Cai, W.; Gong, S. Theranostic Unimolecular Micelles Based on Brush-Shaped Amphiphilic Block Copolymers for Tumor-Targeted Drug Delivery and Positron Emission Tomography Imaging. *ACS Appl. Mater. Interfaces* **2014**, *6* (24), 21769–21779. https://doi.org/10.1021/AM5002585/ASSET/IMAGES/LARGE/AM-2014-002585_0008.JPEG.

(134) Niederberger, A.; Pelras, T.; Manni, L. S.; FitzGerald, P. A.; Warr, G. G.; Müllner, M. Stiffness-Dependent Intracellular Location of Cylindrical Polymer Brushes. *Macromol. Rapid Commun.* **2021**, *42* (13), 2100138. https://doi.org/https://doi.org/10.1002/marc.202100138.

(135) Li, H.; Liu, H.; Nie, T.; Chen, Y.; Wang, Z.; Huang, H.; Liu, L.; Chen, Y. Molecular Bottlebrush as a Unimolecular Vehicle with Tunable Shape for Photothermal Cancer Therapy. *Biomaterials* **2018**, *178*, 620–629. https://doi.org/10.1016/j.biomaterials.2018.03.032.

(136) Grundler, J.; Shin, K.; Suh, H.-W.; Zhong, M.; Saltzman, W. M. Surface Topography of Polyethylene Glycol Shell Nanoparticles Formed from Bottlebrush Block Copolymers Controls Interactions with Proteins and Cells. *ACS Nano* **2021**, *15* (10), 16118–16129. https://doi.org/10.1021/acsnano.1c04835.

(137) LaBarbera, D. V.; Reid, B. G.; Yoo, B. H. The Multicellular Tumor Spheroid Model for High-Throughput Cancer Drug Discovery. *Expert Opin. Drug Discov.* **2012**, *7* (9), 819–830. https://doi.org/10.1517/17460441.2012.708334.

(138) Dini, S.; Binder, B. J.; Fischer, S. C.; Mattheyer, C.; Schmitz, A.; Stelzer, E. H. K.; Bean, N. G.; Green, J. E. F. Identifying the Necrotic Zone Boundary in Tumour Spheroids with Pair-Correlation Functions. *J. R. Soc. Interface* **2016**, *13* (123). https://doi.org/10.1098/rsif.2016.0649.

(139) Xu, C.; Zhao, X.; Wang, L.; YunjingLuo; Zhang, X.; Wang, Y.; Lan, J. Protein Conjugation with Gold Nanoparticles: Spectroscopic and Thermodynamic Analysis on

the Conformational and Activity of Serum Albumin. *J. Nanosci. Nanotechnol.* **2018**, *18* (11), 7818–7823. https://doi.org/10.1166/jnn.2018.15215.

(140) Kumar Das, N.; Chakraborty, S.; Mukherjee, M.; Mukherjee, S. Enhanced Luminescent Properties of Photo-Stable Copper Nanoclusters through Formation of "Protein-Corona"-Like Assemblies. *ChemPhysChem* **2018**, *19* (17), 2218–2223. https://doi.org/10.1002/cphc.201800332.

(141) Negoda, A.; Liu, Y.; Hou, W. C.; Corredor, C.; Moghadam, B. Y.; Musolff, C.; Li, N.; Walker, W.; Westerhoff, P.; Mason, A. J.; Duxbury, P.; Posner, J. D.; Worden, R. M. Engineered Nanomaterial Interactions with Bilayer Lipid Membranes: Screening Platforms to Assess Nanoparticle Toxicity. *Int. J. Biomed. Nanosci. Nanotechnol.* **2013**, *3* (1/2), 52. https://doi.org/10.1504/IJBNN.2013.054512.

(142) Jackman, J.; Knoll, W.; Cho, N.-J. Biotechnology Applications of Tethered Lipid Bilayer Membranes. *Materials (Basel).* **2012**, *5* (12), 2637–2657. https://doi.org/10.3390/ma5122637.

(143) Liu, Y.; Mark Worden, R. Size Dependent Disruption of Tethered Lipid Bilayers by Functionalized Polystyrene Nanoparticles. *Biochim. Biophys. Acta - Biomembr.* **2015**, *1848* (1), 67–75. https://doi.org/10.1016/J.BBAMEM.2014.09.014.

(144) Goreham, R. V; Thompson, V. C.; Samura, Y.; Gibson, C. T.; Shapter, J. G.; Köper, I. Interaction of Silver Nanoparticles with Tethered Bilayer Lipid Membranes. *Langmuir* **2015**, *31* (21), 5868–5874. https://doi.org/10.1021/acs.langmuir.5b00586.

(145) Liu, Y.; Zhang, Z.; Zhang, Q.; Baker, G. L.; Worden, R. M. Biomembrane Disruption by Silica-Core Nanoparticles: Effect of Surface Functional Group Measured Using a Tethered Bilayer Lipid Membrane. *Biochim. Biophys. Acta - Biomembr.* **2014**, *1838* (1, Part B), 429–437. https://doi.org/https://doi.org/10.1016/j.bbamem.2013.09.007.

(146) Römer, W.; Steinem, C. Impedance Analysis and Single-Channel Recordings on Nano-Black Lipid Membranes Based on Porous Alumina. *Biophys. J.* **2004**, *86* (2), 955–965. https://doi.org/10.1016/S0006-3495(04)74171-5.

(147) Jeong, D.-W.; Jang, H.; Choi, S. Q.; Choi, M. C. Enhanced Stability of Freestanding Lipid Bilayer and Its Stability Criteria. *Sci. Rep.* **2016**, *6* (1), 38158. https://doi.org/10.1038/srep38158.

(148) Khan, M.; Dosoky, N.; Williams, J. Engineering Lipid Bilayer Membranes for Protein Studies. *Int. J. Mol. Sci.* **2013**, *14* (11), 21561–21597. https://doi.org/10.3390/ijms141121561.

(149) Anderson, N. A.; Richter, L. J.; Stephenson, J. C.; Briggman, K. A. Characterization and Control of Lipid Layer Fluidity in Hybrid Bilayer Membranes. *J. Am. Chem. Soc.* **2007**, *129* (7), 2094–2100. https://doi.org/10.1021/ja066588c.

(150) Giri, P. M.; Banerjee, A.; Layek, B. A Recent Review on Cancer Nanomedicine. *Cancers (Basel).* **2023**, *15* (8), 2256. https://doi.org/10.3390/cancers15082256.

(151) Jain, R. K.; Stylianopoulos, T. Delivering Nanomedicine to Solid Tumors. *Nat. Rev. Clin. Oncol.* **2010**, *7* (11), 653–664. https://doi.org/10.1038/nrclinonc.2010.139.

(152) Hauert, S.; Bhatia, S. N. Mechanisms of Cooperation in Cancer Nanomedicine: Towards Systems Nanotechnology. *Trends Biotechnol.* **2014**, *32* (9), 448–455. https://doi.org/10.1016/j.tibtech.2014.06.010.

(153) De, R.; Mahata, M. K.; Kim, K. Structure-Based Varieties of Polymeric Nanocarriers and Influences of Their Physicochemical Properties on Drug Delivery Profiles. *Adv. Sci.* **2022**, *9* (10). https://doi.org/10.1002/advs.202105373.

(154) Liu, J.; Zhang, R.; Xu, Z. P. Nanoparticle-Based Nanomedicines to Promote Cancer Immunotherapy: Recent Advances and Future Directions. *Small* **2019**, *15* (32). https://doi.org/10.1002/smll.201900262.

(155) Anderson, C. R.; Gnopo, Y. D. M. M.; Gambinossi, F.; Mylon, S. E.; Ferri, J. K. Modulation of Cell Responses to Ag-(MeO2MA-Co-OEGMA): Effects of Nanoparticle Surface Hydrophobicity and Serum Proteins on Cellular Uptake and Toxicity. *J. Biomed. Mater. Res. Part A* **2018**, *106* (4), 1061–1071. https://doi.org/10.1002/JBM.A.36302.

(156) Moyano, D. F.; Saha, K.; Prakash, G.; Yan, B.; Kong, H.; Yazdani, M.; Rotello, V. M. Fabrication of Corona-Free Nanoparticles with Tunable Hydrophobicity. *ACS Nano* **2014**, *8* (7), 6748–6755. https://doi.org/10.1021/nn5006478.

(157) Humphries, J.; Pizzi, D.; Sonderegger, S. E.; Fletcher, N. L.; Houston, Z. H.; Bell, C. A.; Kempe, K.; Thurecht, K. J. Hyperbranched Poly(2-Oxazoline)s and Poly(Ethylene

Glycol): A Structure-Activity Comparison of Biodistribution. *Biomacromolecules* **2020**, *21* (8), 3318–3331. https://doi.org/10.1021/ACS.BIOMAC.0C00765/ASSET/IMAGES/LARGE/BM0C00765_0005.JPEG.

(158) Sheiko, S. S.; Sumerlin, B. S.; Matyjaszewski, K. Cylindrical Molecular Brushes: Synthesis, Characterization, and Properties. *Prog. Polym. Sci.* **2008**, *33* (7), 759–785. https://doi.org/10.1016/j.progpolymsci.2008.05.001.

(159) Foster, J. C.; Varlas, S.; Couturaud, B.; Coe, Z.; O'Reilly, R. K.; O'Reilly, R. K.; O'Reilly, R. K. Getting into Shape: Reflections on a New Generation of Cylindrical Nanostructures' Self-Assembly Using Polymer Building Blocks. *J. Am. Chem. Soc.* **2019**, *141* (7), 2742–2753. https://doi.org/10.1021/jacs.8b08648.

(160) Roberts, M. G.; Facca, V. J.; Keunen, R.; Yu, Q.; Reilly, R. M.; Winnik, M. A. Changing Surface Polyethylene Glycol Architecture Affects Elongated Nanoparticle Penetration into Multicellular Tumor Spheroids. *Biomacromolecules* **2022**, *23* (8), 3296–3307. https://doi.org/10.1021/ACS.BIOMAC.2C00386/ASSET/IMAGES/LARGE/BM2C00386_0004.JPEG.

(161) Teo, J.; McCarroll, J. A.; Boyer, C.; Youkhana, J.; Sagnella, S. M.; Duong, H. T. T.; Liu, J.; Sharbeen, G.; Goldstein, D.; Davis, T. P.; Kavallaris, M.; Phillips, P. A. A Rationally Optimized Nanoparticle System for the Delivery of RNA Interference Therapeutics into Pancreatic Tumors in Vivo. *Biomacromolecules* **2016**, *17* (7), 2337–2351. https://doi.org/10.1021/acs.biomac.6b00185.

(162) Dai, Y.; Cai, H.; Duan, Z.; Ma, X.; Gong, Q.; Luo, K.; Gu, Z. Effect of Polymer Side Chains on Drug Delivery Properties for Cancer Therapy. *J. Biomed. Nanotechnol.* **2017**, *13* (11), 1369–1385. https://doi.org/10.1166/jbn.2017.2466.

(163) Jamal Al Dine, E.; Ferjaoui, Z.; Ghanbaja, J.; Roques-Carmes, T.; Meftah, A.; Hamieh, T.; Toufaily, J.; Schneider, R.; Marchal, S.; Gaffet, E.; Alem, H. Thermo-Responsive Magnetic Fe 3 O 4 @P(MEO 2 MA X -OEGMA 100-X) NPs and Their Applications as Drug Delivery Systems. *Int. J. Pharm.* **2017**, *532* (2), 738–747. https://doi.org/10.1016/j.ijpharm.2017.09.019.

(164) Gao, W.; Liu, W.; Christensen, T.; Zalutsky, M. R.; Chilkoti, A. In Situ Growth of a

PEG-like Polymer from the C Terminus of an Intein Fusion Protein Improves Pharmacokinetics and Tumor Accumulation. *Proc. Natl. Acad. Sci.* **2010**, *107* (38), 16432–16437. https://doi.org/10.1073/pnas.1006044107.

(165) Ozer, I.; Pitoc, G. A.; Layzer, J. M.; Moreno, A.; Olson, L. B.; Layzer, K. D.; Hucknall, A. M.; Sullenger, B. A.; Chilkoti, A.; Ozer, I.; Hucknall, A. M.; Chilkoti, A.; Pitoc, G. A.; Layzer, J. M.; Moreno, A.; Olson, L. B.; Layzer, K. D.; Sullenger, B. A. PEG-Like Brush Polymer Conjugate of RNA Aptamer That Shows Reversible Anticoagulant Activity and Minimal Immune Response. *Adv. Mater.* **2022**, *34* (10), 2107852. https://doi.org/10.1002/ADMA.202107852.

(166) Ozer, I.; Kelly, G.; Gu, R.; Li, X.; Zakharov, N.; Sirohi, P.; Nair, S. K.; Collier, J. H.; Hershfield, M. S.; Hucknall, A. M.; Chilkoti, A. Polyethylene Glycol-Like Brush Polymer Conjugate of a Protein Drug Does Not Induce an Antipolymer Immune Response and Has Enhanced Pharmacokinetics than Its Polyethylene Glycol Counterpart. *Adv. Sci.* **2022**, *9* (11), 2103672. https://doi.org/10.1002/ADVS.202103672.

(167) Joh, D. Y.; Zimmers, Z.; Avlani, M.; Heggestad, J. T.; Aydin, H. B.; Ganson, N.; Kumar, S.; Fontes, C. M.; Achar, R. K.; Hershfield, M. S.; Hucknall, A. M.; Chilkoti, A. Architectural Modification of Conformal PEG-Bottlebrush Coatings Minimizes Anti-PEG Antigenicity While Preserving Stealth Properties. *Adv. Healthc. Mater.* **2019**, *8* (8). https://doi.org/10.1002/adhm.201801177.

(168) Qi, Y.; Simakova, A.; Ganson, N. J.; Li, X.; Luginbuhl, K. M.; Ozer, I.; Liu, W.; Hershfield, M. S.; Matyjaszewski, K.; Chilkoti, A. A Brush-Polymer/Exendin-4 Conjugate Reduces Blood Glucose Levels for up to Five Days and Eliminates Poly(Ethylene Glycol) Antigenicity. *Nat. Biomed. Eng.* **2016**, *1* (1), 0002. https://doi.org/10.1038/s41551-016-0002.

(169) Lutz, J. F. Polymerization of Oligo(Ethylene Glycol) (Meth)Acrylates: Toward New Generations of Smart Biocompatible Materials. *J. Polym. Sci. Part A Polym. Chem.* **2008**, *46* (11), 3459–3470. https://doi.org/10.1002/pola.22706.

(170) Chen, G.; Wright, P. M.; Geng, J.; Mantovani, G.; Haddleton, D. M. Tunable Thermoresponsive Water-Dispersed Multiwalled Carbon Nanotubes. *Chem. Commun.* **2008**, No. 9, 1097–1099. https://doi.org/10.1039/b718112d.

(171) Yamamoto, S.; Pietrasik, J.; Matyjaszewski, K. ATRP Synthesis of Thermally Responsive Molecular Brushes from Oligo(Ethylene Oxide) Methacrylates. *Macromolecules* **2007**, *40* (26), 9348–9353. https://doi.org/10.1021/ma701970t.

(172) Ramamurthi, P.; Zhao, Z.; Burke, E.; Steinmetz, N. F.; Müllner, M. Tuning the Hydrophilic–Hydrophobic Balance of Molecular Polymer Bottlebrushes Enhances Their Tumor Homing Properties. *Adv. Healthc. Mater.* **2022**, *11* (12), 2200163. https://doi.org/10.1002/ADHM.202200163.

(173) Nastyshyn, S.; Stetsyshyn, Y.; Raczkowska, J.; Nastishin, Y.; Melnyk, Y.; Panchenko, Y.; Budkowski, A. Temperature-Responsive Polymer Brush Coatings for Advanced Biomedical Applications. *Polym. 2022, Vol. 14, Page 4245* **2022**, *14* (19), 4245. https://doi.org/10.3390/POLYM14194245.

(174) Lutz, J. F. Thermo-Switchable Materials Prepared Using the OEGMA-Platform. *Adv. Mater.* **2011**, *23* (19), 2237–2243. https://doi.org/10.1002/adma.201100597.

(175) Xie, Y.; Li, N. K.; Singh, A.; Deshmukh, S. A.; Yingling, Y. G. A Comparison between the Lower Critical Solution Temperature Behavior of Polymers and Biomacromolecules. *Physchem* **2022**, *2* (1), 52–71. https://doi.org/10.3390/physchem2010005.

(176) Lutz, J.-F.; Hoth, A. Preparation of Ideal PEG Analogues with a Tunable Thermosensitivity by Controlled Radical Copolymerization of 2-(2-Methoxyethoxy)Ethyl Methacrylate and Oligo(Ethylene Glycol) Methacrylate. *Macromolecules* **2006**, *39* (2), 893–896. https://doi.org/10.1021/ma0517042.

(177) Ramírez-Jiménez; Montoya-Villegas; Licea-Claverie; Gónzalez-Ayón. Tunable Thermo-Responsive Copolymers from DEGMA and OEGMA Synthesized by RAFT Polymerization and the Effect of the Concentration and Saline Phosphate Buffer on Its Phase Transition. *Polymers (Basel).* **2019**, *11* (10), 1657. https://doi.org/10.3390/polym11101657.

(178) Liwinska, W.; Waleka-Bagiel, E.; Stojek, Z.; Karbarz, M.; Zabost, E. Enzyme-Triggered- and Tumor-Targeted Delivery with Tunable, Methacrylated Poly(Ethylene Glycols) and Hyaluronic Acid Hybrid Nanogels. *Drug Deliv.* **2022**, *29* (1), 2561–2578. https://doi.org/10.1080/10717544.2022.2105443.

(179) Salmaso, S.; Caliceti, P.; Amendola, V.; Meneghetti, M.; Magnusson, J. P.; Pasparakis, G.; Alexander, C. Cell Up-Take Control of Gold Nanoparticles Functionalized with a Thermoresponsive Polymer. *J. Mater. Chem.* **2009**, *19* (11), 1608–1615. https://doi.org/10.1039/B816603J.

(180) Kurzhals, S.; Gal, N.; Zirbs, R.; Reimhult, E. Controlled Aggregation and Cell Uptake of Thermoresponsive Polyoxazoline-Grafted Superparamagnetic Iron Oxide Nanoparticles. *Nanoscale* **2017**, *9* (8), 2793–2805. https://doi.org/10.1039/C6NR08654C.

(181) Cataldi, M.; Vigliotti, C.; Mosca, T.; Cammarota, M. R.; Capone, D. Emerging Role of the Spleen in the Pharmacokinetics of Monoclonal Antibodies, Nanoparticles and Exosomes. *Int. J. Mol. Sci.* **2017**, *18* (6). https://doi.org/10.3390/ijms18061249.

(182) Moghimi, S. M.; Hunter, A. C.; Andresen, T. L. Factors Controlling Nanoparticle Pharmacokinetics: An Integrated Analysis and Perspective. *Annu. Rev. Pharmacol. Toxicol.* **2012**, *52* (1), 481–503. https://doi.org/10.1146/annurev-pharmtox-010611-134623.

(183) Moghimi, S. M.; Hedeman, H.; Muir, I. S.; Illum, L.; Davis, S. S. An Investigation of the Filtration Capacity and the Fate of Large Filtered Sterically-Stabilized Microspheres in Rat Spleen. *Biochim. Biophys. Acta - Gen. Subj.* **1993**, *1157* (2), 233–240. https://doi.org/10.1016/0304-4165(93)90105-H.

(184) Ernsting, M. J.; Murakami, M.; Roy, A.; Li, S. D. Factors Controlling the Pharmacokinetics, Biodistribution and Intratumoral Penetration of Nanoparticles. *J. Control. Release* **2013**, *172* (3), 782–794. https://doi.org/10.1016/j.jconrel.2013.09.013.

(185) Demoy, M.; Andreux, J. P.; Weingarten, C.; Gouritin, B.; Guilloux, V.; Couvreur, P. In Vitro Evaluation of Nanoparticles Spleen Capture. *Life Sci.* **1999**, *64* (15), 1329–1337. https://doi.org/10.1016/S0024-3205(99)00068-5.

(186) Ke, P. C.; Lin, S.; Parak, W. J.; Davis, T. P.; Caruso, F. A Decade of the Protein Corona. *ACS Nano* **2017**, *11* (12), 11773–11776. https://doi.org/10.1021/acsnano.7b08008.

(187) Tekie, F. S. M.; Hajiramezanali, M.; Geramifar, P.; Raoufi, M.; Dinarvand, R.; Soleimani, M.; Atyabi, F. Controlling Evolution of Protein Corona: A Prosperous Approach to Improve Chitosan-Based Nanoparticle Biodistribution and Half-Life. *Sci.*

Rep. **2020**, *10* (1), 9664. https://doi.org/10.1038/s41598-020-66572-y.

(188) Schöttler, S.; Landfester, K.; Mailänder, V. Controlling the Stealth Effect of Nanocarriers through Understanding the Protein Corona. *Angew. Chemie Int. Ed.* **2016**, *55* (31), 8806–8815. https://doi.org/10.1002/anie.201602233.

(189) Mosquera, J.; Garciá, I.; Henriksen-Lacey, M.; Martínez-Calvo, M.; Dhanjani, M.; Mascarenãs, J. L.; Liz-Marzán, L. M. Reversible Control of Protein Corona Formation on Gold Nanoparticles Using Host-Guest Interactions. *ACS Nano* **2020**, *14* (5), 5382–5391. https://doi.org/10.1021/acsnano.9b08752.

(190) Ahmed, S. T.; Leckband, D. E. Protein Adsorption on Grafted Zwitterionic Polymers Depends on Chain Density and Molecular Weight. *Adv. Funct. Mater.* **2020**, *30* (30). https://doi.org/10.1002/adfm.202000757.

(191) Hamad, I.; Al-Hanbali, O.; Hunter, A. C.; Rutt, K. J.; Andresen, T. L.; Moghimi, S. M. Distinct Polymer Architecture Mediates Switching of Complement Activation Pathways at the Nanosphere−Serum Interface: Implications for Stealth Nanoparticle Engineering. *ACS Nano* **2010**, *4* (11), 6629–6638. https://doi.org/10.1021/nn101990a.

(192) Palchetti, S.; Pozzi, D.; Capriotti, A. L.; Barbera, G. La; Chiozzi, R. Z.; Digiacomo, L.; Peruzzi, G.; Caracciolo, G.; Laganà, A. Influence of Dynamic Flow Environment on Nanoparticle-Protein Corona: From Protein Patterns to Uptake in Cancer Cells. *Colloids Surfaces B Biointerfaces* **2017**, *153*, 263–271. https://doi.org/10.1016/j.colsurfb.2017.02.037.

(193) Huang, K.; Boerhan, R.; Liu, C.; Jiang, G. Nanoparticles Penetrate into the Multicellular Spheroid-on-Chip: Effect of Surface Charge, Protein Corona, and Exterior Flow. *Mol. Pharm.* **2017**, *14* (12), 4618–4627. https://doi.org/10.1021/acs.molpharmaceut.7b00726.

(194) Calatayud, M. P.; Sanz, B.; Raffa, V.; Riggio, C.; Ibarra, M. R.; Goya, G. F. The Effect of Surface Charge of Functionalized Fe3O4 Nanoparticles on Protein Adsorption and Cell Uptake. *Biomaterials* **2014**, *35* (24), 6389–6399. https://doi.org/10.1016/j.biomaterials.2014.04.009.

(195) Wang, W.; Huang, Z.; Li, Y.; Wang, W.; Shi, J.; Fu, F.; Huang, Y.; Pan, X.; Wu, C. Impact of Particle Size and PH on Protein Corona Formation of Solid Lipid

Nanoparticles: A Proof-of-Concept Study. *Acta Pharm. Sin. B* **2021**, *11* (4), 1030–1046. https://doi.org/10.1016/j.apsb.2020.10.023.

(196) Zhao, Z.; Li, G.; Liu, Q. S.; Liu, W.; Qu, G.; Hu, L.; Long, Y.; Cai, Z.; Zhao, X.; Jiang, G. Identification and Interaction Mechanism of Protein Corona on Silver Nanoparticles with Different Sizes and the Cellular Responses. *J. Hazard. Mater.* **2021**, *414*, 125582. https://doi.org/10.1016/j.jhazmat.2021.125582.

(197) Xu, F.; Reiser, M.; Yu, X.; Gummuluru, S.; Wetzler, L.; Reinhard, B. M. Lipid-Mediated Targeting with Membrane-Wrapped Nanoparticles in the Presence of Corona Formation. *ACS Nano* **2016**, *10* (1), 1189–1200. https://doi.org/10.1021/acsnano.5b06501.

(198) Alberg, I.; Kramer, S.; Schinnerer, M.; Hu, Q.; Seidl, C.; Leps, C.; Drude, N.; Möckel, D.; Rijcken, C.; Lammers, T.; Diken, M.; Maskos, M.; Morsbach, S.; Landfester, K.; Tenzer, S.; Barz, M.; Zentel, R. Polymeric Nanoparticles with Neglectable Protein Corona. *Small* **2020**, *16* (18). https://doi.org/10.1002/smll.201907574.

(199) Lindman, S.; Lynch, I.; Thulin, E.; Nilsson, H.; Dawson, K. A.; Linse, S. Systematic Investigation of the Thermodynamics of HSA Adsorption to N-Iso-Propylacrylamide/N-Tert-Butylacrylamide Copolymer Nanoparticles. Effects of Particle Size and Hydrophobicity. *Nano Lett.* **2007**, *7* (4), 914–920. https://doi.org/10.1021/nl062743+.

(200) Aggarwal, P.; Hall, J. B.; McLeland, C. B.; Dobrovolskaia, M. A.; McNeil, S. E. Nanoparticle Interaction with Plasma Proteins as It Relates to Particle Biodistribution, Biocompatibility and Therapeutic Efficacy. *Adv. Drug Deliv. Rev.* **2009**, *61* (6), 428–437. https://doi.org/10.1016/j.addr.2009.03.009.

(201) Pustulka, S. M.; Ling, K.; Pish, S. L.; Champion, J. A. Protein Nanoparticle Charge and Hydrophobicity Govern Protein Corona and Macrophage Uptake. *ACS Appl. Mater. Interfaces* **2020**, *12* (43), 48284–48295. https://doi.org/10.1021/acsami.0c12341.

(202) Yu, Q.; Zhao, L.; Guo, C.; Yan, B.; Su, G. Regulating Protein Corona Formation and Dynamic Protein Exchange by Controlling Nanoparticle Hydrophobicity. *Front. Bioeng. Biotechnol.* **2020**, *8*, 522931. https://doi.org/10.3389/fbioe.2020.00210.

(203) Hellstrand, E.; Lynch, I.; Andersson, A.; Drakenberg, T.; Dahlbäck, B.; Dawson, K. A.; Linse, S.; Cedervall, T. Complete High-Density Lipoproteins in Nanoparticle Corona.

FEBS J. **2009**, *276* (12), 3372–3381. https://doi.org/10.1111/j.1742-4658.2009.07062.x.

(204) Sun, H.; Jiang, C.; Wu, L.; Bai, X.; Zhai, S. Cytotoxicity-Related Bioeffects Induced by Nanoparticles: The Role of Surface Chemistry. *Front. Bioeng. Biotechnol.* **2019**, *7*. https://doi.org/10.3389/fbioe.2019.00414.

(205) Chen, J.; Hessler, J. A.; Putchakayala, K.; Panama, B. K.; Khan, D. P.; Hong, S.; Mullen, D. G.; DiMaggio, S. C.; Som, A.; Tew, G. N.; Lopatin, A. N.; Baker, J. R.; Holl, M. M. B.; Orr, B. G. Cationic Nanoparticles Induce Nanoscale Disruption in Living Cell Plasma Membranes. *J. Phys. Chem. B* **2009**, *113* (32), 11179–11185. https://doi.org/10.1021/JP9033936/SUPPL_FILE/JP9033936_SI_001.PDF.

(206) Zhang, Y.; Dahal, U.; Feng, Z. V.; Rosenzweig, Z.; Cui, Q.; Hamers, R. J. Influence of Surface Ligand Molecular Structure on Phospholipid Membrane Disruption by Cationic Nanoparticles. *Langmuir* **2021**, *37* (24), 7600–7610. https://doi.org/10.1021/acs.langmuir.1c01146.

(207) Zhang, Y.; Hudson-Smith, N. V.; Frand, S. D.; Cahill, M. S.; Davis, L. S.; Feng, Z. V.; Haynes, C. L.; Hamers, R. J. Influence of the Spatial Distribution of Cationic Functional Groups at Nanoparticle Surfaces on Bacterial Viability and Membrane Interactions. *J. Am. Chem. Soc.* **2020**, *142* (24), 10814–10823. https://doi.org/10.1021/jacs.0c02737.

(208) van de Wetering, P.; Moret, E. E.; Schuurmans-Nieuwenbroek, N. M. E.; van Steenbergen, M. J.; Hennink, W. E. Structure−Activity Relationships of Water-Soluble Cationic Methacrylate/Methacrylamide Polymers for Nonviral Gene Delivery. *Bioconjug. Chem.* **1999**, *10* (4), 589–597. https://doi.org/10.1021/bc980148w.

(209) Castells, V.; Van Tassel, P. R. Conformational Transition Free Energy Profiles of an Adsorbed, Lattice Model Protein by Multicanonical Monte Carlo Simulation. *J. Chem. Phys.* **2005**, *122* (8). https://doi.org/10.1063/1.1849772.

(210) Poncin-Epaillard, F.; Vrlinic, T.; Debarnot, D.; Mozetic, M.; Coudreuse, A.; Legeay, G.; El Moualij, B.; Zorzi, W. Surface Treatment of Polymeric Materials Controlling the Adhesion of Biomolecules. *J. Funct. Biomater.* **2012**, *3* (3), 528–543. https://doi.org/10.3390/jfb3030528.

(211) Zhang, Y.; Cai, J.; Li, C.; Wei, J.; Liu, Z.; Xue, W. Effects of Thermosensitive Poly(N-Isopropylacrylamide) on Blood Coagulation. *J. Mater. Chem. B* **2016**, *4* (21), 3733–

3749. https://doi.org/10.1039/C6TB00823B.

(212) O'Brien, J.; Shea, K. J. Tuning the Protein Corona of Hydrogel Nanoparticles: The Synthesis of Abiotic Protein and Peptide Affinity Reagents. *Acc. Chem. Res.* **2016**, *49* (6), 1200–1210. https://doi.org/10.1021/acs.accounts.6b00125.

(213) Koshkina, O.; Lang, T.; Thiermann, R.; Docter, D.; Stauber, R. H.; Secker, C.; Schlaad, H.; Weidner, S.; Mohr, B.; Maskos, M.; Bertin, A. Temperature-Triggered Protein Adsorption on Polymer-Coated Nanoparticles in Serum. *Langmuir* **2015**, *31* (32), 8873–8881. https://doi.org/10.1021/ACS.LANGMUIR.5B00537/ASSET/IMAGES/LARGE/LA-2015-00537S_0007.JPEG.

(214) Koshkina, O.; Westmeier, D.; Lang, T.; Bantz, C.; Hahlbrock, A.; Würth, C.; Resch-Genger, U.; Braun, U.; Thiermann, R.; Weise, C.; Eravci, M.; Mohr, B.; Schlaad, H.; Stauber, R. H.; Docter, D.; Bertin, A.; Maskos, M. Tuning the Surface of Nanoparticles: Impact of Poly(2-Ethyl-2-Oxazoline) on Protein Adsorption in Serum and Cellular Uptake. *Macromol. Biosci.* **2016**, *16* (9), 1287–1300. https://doi.org/10.1002/MABI.201600074.

(215) Lesniak, A.; Campbell, A.; Monopoli, M. P.; Lynch, I.; Salvati, A.; Dawson, K. A. Serum Heat Inactivation Affects Protein Corona Composition and Nanoparticle Uptake. *Biomaterials* **2010**, *31* (36), 9511–9518. https://doi.org/10.1016/j.biomaterials.2010.09.049.

(216) Høl, P.; Ekeland Allouni, Z.; Gjerdet, N. R.; Cimpan, M. R. The Effect of Blood Protein Adsorption on Cellular Uptake of Anatase TiO2 Nanoparticles. *Int. J. Nanomedicine* **2015**, 687. https://doi.org/10.2147/IJN.S72726.

(217) Lesniak, A.; Fenaroli, F.; Monopoli, M. P.; Åberg, C.; Dawson, K. A.; Salvati, A. Effects of the Presence or Absence of a Protein Corona on Silica Nanoparticle Uptake and Impact on Cells. *ACS Nano* **2012**, *6* (7), 5845–5857. https://doi.org/10.1021/NN300223W/SUPPL_FILE/NN300223W_SI_001.PDF.

(218) El-Baz, N.; Nunn, B. M.; Bates, P. J.; O'Toole, M. G. The Impact of PEGylation on Cellular Uptake and In Vivo Biodistribution of Gold Nanoparticle MRI Contrast Agents. *Bioengineering* **2022**, *9* (12), 766. https://doi.org/10.3390/bioengineering9120766.

(219) Pelaz, B.; del Pino, P.; Maffre, P.; Hartmann, R.; Gallego, M.; Rivera-Fernández, S.; de la Fuente, J. M.; Nienhaus, G. U.; Parak, W. J. Surface Functionalization of Nanoparticles with Polyethylene Glycol: Effects on Protein Adsorption and Cellular Uptake. *ACS Nano* **2015**, *9* (7), 6996–7008. https://doi.org/10.1021/acsnano.5b01326.

(220) Mishra, S.; Webster, P.; Davis, M. E. PEGylation Significantly Affects Cellular Uptake and Intracellular Trafficking of Non-Viral Gene Delivery Particles. *Eur. J. Cell Biol.* **2004**, *83* (3), 97–111. https://doi.org/10.1078/0171-9335-00363.

(221) Merlot, A. M.; Kalinowski, D. S.; Richardson, D. R. Unraveling the Mysteries of Serum Albumin - More than Just a Serum Protein. *Front. Physiol.* **2014**, *5*. https://doi.org/10.3389/fphys.2014.00299.

(222) Nguyen, V. H.; Meghani, N. M.; Amin, H. H.; Tran, T. T. D.; Tran, P. H. L.; Park, C.; Lee, B.-J. Modulation of Serum Albumin Protein Corona for Exploring Cellular Behaviors of Fattigation-Platform Nanoparticles. *Colloids Surfaces B Biointerfaces* **2018**, *170*, 179–186. https://doi.org/10.1016/j.colsurfb.2018.05.060.

(223) Schroffenegger, M.; Leitner, N. S.; Morgese, G.; Ramakrishna, S. N.; Willinger, M.; Benetti, E. M.; Reimhult, E. Polymer Topology Determines the Formation of Protein Corona on Core–Shell Nanoparticles. *ACS Nano* **2020**, *14* (10), 12708–12718. https://doi.org/10.1021/acsnano.0c02358.

(224) Lee, M. F. X.; Chan, E. S.; Tam, K. C.; Tey, B. T. Thermo-Responsive Adsorbent for Size-Selective Protein Adsorption. *J. Chromatogr. A* **2015**, *1394*, 71–80. https://doi.org/10.1016/j.chroma.2015.03.034.

(225) Xue, C.; Yonet-Tanyeri, N.; Brouette, N.; Sferrazza, M.; Braun, P. V.; Leckband, D. E. Protein Adsorption on Poly(N -Isopropylacrylamide) Brushes: Dependence on Grafting Density and Chain Collapse. *Langmuir* **2011**, *27* (14), 8810–8818. https://doi.org/10.1021/la2001909.

(226) Murakami, D.; Kitahara, Y.; Kobayashi, S.; Tanaka, M. Thermosensitive Polymer Biocompatibility Based on Interfacial Structure at Biointerface. *ACS Biomater. Sci. Eng.* **2018**, acsbiomaterials.8b00081. https://doi.org/10.1021/acsbiomaterials.8b00081.

(227) Raghuwanshi, V. S.; Yu, B.; Browne, C.; Garnier, G. Reversible PH Responsive Bovine Serum Albumin Hydrogel Sponge Nanolayer. *Front. Bioeng. Biotechnol.* **2020**, *8*.

https://doi.org/10.3389/fbioe.2020.00573.

(228) Shivabalan, A. P.; Ambrulevicius, F.; Talaikis, M.; Pudzaitis, V.; Niaura, G.; Valincius, G. Effect of PH on Electrochemical Impedance Response of Tethered Bilayer Lipid Membranes: Implications for Quantitative Biosensing. *Chemosensors* **2023**, *11* (8), 450. https://doi.org/10.3390/chemosensors11080450.

(229) Wang, S.; Guo, H.; Li, Y.; Li, X. Penetration of Nanoparticles across a Lipid Bilayer: Effects of Particle Stiffness and Surface Hydrophobicity. *Nanoscale* **2019**, *11* (9), 4025–4034. https://doi.org/10.1039/C8NR09381D.

(230) Li, Y.; Chen, X.; Gu, N. Computational Investigation of Interaction between Nanoparticles and Membranes: Hydrophobic/Hydrophilic Effect. *J. Phys. Chem. B* **2008**, *112* (51), 16647–16653. https://doi.org/10.1021/jp8051906.

(231) Xia, Z.; Woods, A.; Quirk, A.; Burgess, I. J.; Lau, B. L. T. Interactions between Polystyrene Nanoparticles and Supported Lipid Bilayers: Impact of Charge and Hydrophobicity Modification by Specific Anions. *Environ. Sci. Nano* **2019**, *6* (6), 1829–1837. https://doi.org/10.1039/C9EN00055K.

(232) Jing, B.; Abot, R. C. T.; Zhu, Y. Semihydrophobic Nanoparticle-Induced Disruption of Supported Lipid Bilayers: Specific Ion Effect. *J. Phys. Chem. B* **2014**, *118* (46), 13175–13182. https://doi.org/10.1021/jp5074945.

(233) Kabanov, A. V.; Batrakova, E. V.; Miller, D. W. Pluronic® Block Copolymers as Modulators of Drug Efflux Transporter Activity in the Blood–Brain Barrier. *Adv. Drug Deliv. Rev.* **2003**, *55* (1), 151–164. https://doi.org/10.1016/S0169-409X(02)00176-X.

(234) Gopinath, P. M.; Saranya, V.; Vijayakumar, S.; Mythili Meera, M.; Ruprekha, S.; Kunal, R.; Pranay, A.; Thomas, J.; Mukherjee, A.; Chandrasekaran, N. Assessment on Interactive Prospectives of Nanoplastics with Plasma Proteins and the Toxicological Impacts of Virgin, Coronated and Environmentally Released-Nanoplastics. *Sci. Reports 2019 91* **2019**, *9* (1), 1–15. https://doi.org/10.1038/s41598-019-45139-6.

(235) Lesniak, A.; Salvati, A.; Santos-Martinez, M. J.; Radomski, M. W.; Dawson, K. A.; Åberg, C. Nanoparticle Adhesion to the Cell Membrane and Its Effect on Nanoparticle Uptake Efficiency. *J. Am. Chem. Soc.* **2013**, *135* (4), 1438–1444. https://doi.org/10.1021/JA309812Z/SUPPL_FILE/JA309812Z_SI_001.PDF.

(236) Silvio, D. Di; Maccarini, M.; Parker, R.; Mackie, A.; Fragneto, G.; Bombelli, F. B. The Effect of the Protein Corona on the Interaction between Nanoparticles and Lipid Bilayers. *J. Colloid Interface Sci.* **2017**, *504*, 741–750. https://doi.org/10.1016/j.jcis.2017.05.086.

(237) Lu, X.; Xu, P.; Ding, H.-M.; Yu, Y.-S.; Huo, D.; Ma, Y.-Q. Tailoring the Component of Protein Corona via Simple Chemistry. *Nat. Commun.* **2019**, *10* (1), 4520.

(238) Schöttler, S.; Becker, G.; Winzen, S.; Steinbach, T.; Mohr, K.; Landfester, K.; Mailänder, V.; Wurm, F. R. Protein Adsorption Is Required for Stealth Effect of Poly(Ethylene Glycol)- and Poly(Phosphoester)-Coated Nanocarriers. *Nat. Nanotechnol.* **2016**, *11* (4), 372–377. https://doi.org/10.1038/nnano.2015.330.

(239) Roach, P.; Farrar, D.; Perry, C. C. Interpretation of Protein Adsorption: Surface-Induced Conformational Changes. *J. Am. Chem. Soc.* **2005**, *127* (22), 8168–8173. https://doi.org/10.1021/ja042898o.

(240) Roach, P.; Farrar, D.; Perry, C. C. Surface Tailoring for Controlled Protein Adsorption: Effect of Topography at the Nanometer Scale and Chemistry. *J. Am. Chem. Soc.* **2006**, *128* (12), 3939–3945.

(241) Abuwatfa, W. H.; Awad, N. S.; Pitt, W. G.; Husseini, G. A. Thermosensitive Polymers and Thermo-Responsive Liposomal Drug Delivery Systems. *Polymers (Basel).* **2022**, *14* (5), 925. https://doi.org/10.3390/polym14050925.

(242) Bordat, A.; Boissenot, T.; Nicolas, J.; Tsapis, N. Thermoresponsive Polymer Nanocarriers for Biomedical Applications. *Adv. Drug Deliv. Rev.* **2019**, *138*, 167–192. https://doi.org/https://doi.org/10.1016/j.addr.2018.10.005.

(243) Sun, X.-L.; Tsai, P.-C.; Bhat, R.; Bonder, E. M.; Michniak-Kohn, B.; Pietrangelo, A. Thermoresponsive Block Copolymer Micelles with Tunable Pyrrolidone-Based Polymer Cores: Structure/Property Correlations and Application as Drug Carriers. *J. Mater. Chem. B* **2015**, *3* (5), 814–823. https://doi.org/10.1039/C4TB01494D.

(244) Yoshino, K.; Kadowaki, A.; Takagishi, T.; Kono, K. Temperature Sensitization of Liposomes by Use of N -Isopropylacrylamide Copolymers with Varying Transition Endotherms. *Bioconjug. Chem.* **2004**, *15* (5), 1102–1109. https://doi.org/10.1021/bc034205j.

(245) Ferjaoui, Z.; Schneider, R.; Meftah, A.; Gaffet, E.; Alem, H. Functional Responsive Superparamagnetic Core/Shell Nanoparticles and Their Drug Release Properties. *RSC Adv.* **2017**, *7* (42), 26243–26249. https://doi.org/10.1039/C7RA02437A.

(246) Deng, L.; Ren, J.; Li, J.; Leng, J.; Qu, Y.; Lin, C.; Shi, D. Magnetothermally Responsive Star-Block Copolymeric Micelles for Controlled Drug Delivery and Enhanced Thermo-Chemotherapy. *Nanoscale* **2015**, *7* (21), 9655–9663. https://doi.org/10.1039/C5NR00642B.

(247) Hu, Y.; Darcos, V.; Monge, S.; Li, S. Thermo-Responsive Drug Release from Self-Assembled Micelles of Brush-like PLA/PEG Analogues Block Copolymers. *Int. J. Pharm.* **2015**, *491* (1–2), 152–161. https://doi.org/10.1016/j.ijpharm.2015.06.020.

(248) Ohnsorg, M. L.; Prendergast, P. C.; Robinson, L. L.; Bockman, M. R.; Bates, F. S.; Reineke, T. M. Bottlebrush Polymer Excipients Enhance Drug Solubility: Influence of End-Group Hydrophilicity and Thermoresponsiveness. *ACS Macro Lett.* **2021**, 375–381. https://doi.org/10.1021/acsmacrolett.0c00890.

(249) Tanaka, M.; Mochizuki, A. Effect of Water Structure on Blood Compatibility—Thermal Analysis of Water in Poly(Meth)Acrylate. *J. Biomed. Mater. Res. Part A* **2004**, *68A* (4), 684–695. https://doi.org/https://doi.org/10.1002/jbm.a.20088.

(250) Kuo, A. T.; Urata, S.; Koguchi, R.; Sonoda, T.; Kobayashi, S.; Tanaka, M. Effects of Side-Chain Spacing and Length on Hydration States of Poly(2-Methoxyethyl Acrylate) Analogues: A Molecular Dynamics Study. *ACS Biomater. Sci. Eng.* **2021**, *7* (6), 2383–2391. https://doi.org/10.1021/acsbiomaterials.1c00388.

(251) Weber, C.; Simon, J.; Mailänder, V.; Morsbach, S.; Landfester, K. Preservation of the Soft Protein Corona in Distinct Flow Allows Identification of Weakly Bound Proteins. *Acta Biomater.* **2018**, *76*, 217–224. https://doi.org/10.1016/j.actbio.2018.05.057.

(252) Yohannes, G.; Jussila, M.; Hartonen, K.; Riekkola, M.-L. Asymmetrical Flow Field-Flow Fractionation Technique for Separation and Characterization of Biopolymers and Bioparticles. *J. Chromatogr. A* **2011**, *1218* (27), 4104–4116. https://doi.org/10.1016/j.chroma.2010.12.110.

(253) Richtering, W.; Alberg, I.; Zentel, R. Nanoparticles in the Biological Context: Surface Morphology and Protein Corona Formation. *Small* **2020**, *16* (39), 1–8.

https://doi.org/10.1002/smll.202002162.

(254) Bian, J.; Gobalasingham, N.; Purchel, A.; Lin, J. The Power of Field-Flow Fractionation in Characterization of Nanoparticles in Drug Delivery. *Molecules* **2023**, *28* (10), 4169. https://doi.org/10.3390/molecules28104169.

(255) Hansen, U.; Thünemann, A. F. Characterization of Silver Nanoparticles in Cell Culture Medium Containing Fetal Bovine Serum. *Langmuir* **2015**, *31* (24), 6842–6852. https://doi.org/10.1021/ACS.LANGMUIR.5B00687/SUPPL_FILE/LA5B00687_SI_001.PDF.

(256) Kihara, S.; Ashenden, A.; Kaur, M.; Glasson, J.; Ghosh, S.; van der Heijden, N.; Brooks, A. E. S.; Mata, J. P.; Holt, S.; Domigan, L. J.; Köper, I.; McGillivray, D. J. Cellular Interactions with Polystyrene Nanoplastics—The Role of Particle Size and Protein Corona. *Biointerphases* **2021**, *16* (4), 041001. https://doi.org/10.1116/6.0001124.